

Copyright
by
Claudia Knez
2006

The Dissertation Committee for Claudia Knez
certifies that this is the approved version of the following dissertation:

**Chemical Evolution of Ice and Gas from Molecular
Clouds to Protostars**

Committee:

Neal J. Evans II, Supervisor

John H. Lacy, Supervisor

Paul M. Harvey

Daniel T. Jaffe

John Scalo

Ewine F. van Dishoeck

**Chemical Evolution of Ice and Gas from Molecular
Clouds to Protostars**

by

Claudia Knez, B.A.

DISSERTATION

Presented to the Faculty of the Graduate School of
The University of Texas at Austin
in Partial Fulfillment
of the Requirements
for the Degree of

DOCTOR OF PHILOSOPHY

THE UNIVERSITY OF TEXAS AT AUSTIN

August 2006

To Celina

Acknowledgments

First I would like to thank my advisors, Neal Evans and John Lacy, for their wonderful patience and support for the past years. I have thoroughly enjoyed working with them and learning from them. They have always been very welcoming and very understanding. Some people say it is difficult having two advisors. I found it very enjoyable as it provided me the opportunity to learn and think in different ways. On a personal level, I would like to thank Neal, Leslie, John, and Marianne for their friendship.

I would like to thank my committee, Dan Jaffe, Paul Harvey, John Scalo, and Ewine van Dishoeck, for providing the guidance and the push I needed to get things done. To Ewine, I express a special thanks for all her help in all aspects of my research. Her insight with the chemistry has been invaluable. Also, I would like to thank her for giving me the opportunity to visit Leiden to work with her and with Annemieke Boonman-Gludemans.

I express my sincerest gratitude for all their support to the c2d team, especially the IRS team. To Adwin Boogert and Helen Fraser, I would like to thank for all their help and support with the work on ices. It meant a lot to me to have their support since I knew nothing about ices before embarking on this venture. Thanks also go to Fred Lahuis for all the discussion we had on the gas-phase absorption especially for CH_3 . I would like to give a special

thanks to Jackie Kessler-Silacci for her friendship and for all the times we went to lunch together as well as for the useful scientific discussions.

When I visited Leiden for the first time, Annemieke Boonman-Gludemans served as my tour guide and hostess. I am grateful for her hospitality. Also, I am grateful for all of the discussion we had on AFGL 2591.

I would also like to thank Marc van Hemert for providing the band strength of HNCO. Information on this molecule was hard to acquire and I am grateful for his contribution.

I would like to thank all of my fellow grad students, I could not have done it with out them. Many of them have graduated already and some of them are yet to finish. I am grateful for their friendship and camaraderie.

I am extremely thankful for my *comadre*, Eva, with whom I shared an apartment/house for 4 years of grad school. Her friendship has been wonderful and it will be difficult to part our separate ways.

A big thanks goes to flat pieces of plastic known as frisbees. Playing ultimate frisbee has helped keep me sane throughout the years. My teammates and friends have provided an important distraction from working all the time.

I would like to thank Mrs. Diane Luttrell for all her extra efforts to help teach me. Her help was invaluable in preparing for college and building the confidence I needed to continue pursuing my dreams.

A big thanks goes to my grandmother Yolanda, who set an example for me. She studied chemistry in Mexico at a time where very few women

attended universities, much less study science. She wanted to be a medical doctor, but she was a woman. So she studied the subject that interested her, chemistry. Her determination has been inspiring.

To my parents, I express the deepest gratitude for all their support and encouragement throughout my life. I would like to especially thank my mother for everything, and I mean EVERYTHING, she has done for me. Without her, I would not be here. I admire her strength and determination. I love her very much and I could not have done it without her support. Thank you to my brothers, who are curious about science and invite me to speak to their classmates.

Lastly, I would like to thank my husband Jared. Since we were at UVA, we have supported each other in our endeavors. There were many rough times throughout grad school. Some had to do with science, others were personal. He was always by my side (though sometimes not literally). I could not have made it through without his support and encouragement. Thank you so much!!

Chemical Evolution of Ice and Gas from Molecular Clouds to Protostars

Publication No. _____

Claudia Knez, Ph.D.

The University of Texas at Austin, 2006

Supervisors: Neal J. Evans II
John H. Lacy

We present observations toward stars behind molecular clouds (background stars) and toward massive protostars in order to study the chemical evolution in molecular clouds before and during star formation. Infrared absorption spectroscopy with the *Spitzer Space Telescope* toward background stars shows that complex ices exist toward lines of sight not associated with star formation. In addition to solid H₂O, CO, and CO₂, we find evidence for HCOOH and a tentative identification of NH₄⁺. We also find that the 6.0 μm H₂O band changes when mixed with CO₂ in high concentrations. These results give the initial composition of solid material prior to star formation.

Once the star formation process ensues, the icy grain mantles sublime due to heating from the protostar. We present gas-phase, infrared absorption spectroscopy using TEXES, a high-resolution spectrograph, toward the massive protostars NGC 7538 IRS 1 and AFGL 2591. While we only detect two

molecules (C_2H_2 and HCN) toward AFGL 2591, NGC 7538 IRS 1 shows a very rich mid-infrared spectrum with absorption from seven molecules (C_2H_2 , HCN , CH_3 , HNCO , NH_3 , CH_4 , and CS). We present the first infrared detection of interstellar HNCO as well as the first detection of CH_3 in dense gas. Sublimation of icy mantles can explain the observed enhancement of molecules formed on grains such as CH_4 , NH_3 , and HNCO . Other species such as C_2H_2 are also enhanced though its formation is less certain. It is possible that C_2H_2 also forms on grains though no evidence of solid C_2H_2 has been found to date. Daughter molecules such as CH_3 are also found in high abundance toward NGC 7538 IRS 1. The gas observations presented in this work could be tracing material in a disk or material that, at some point in time, was part of a circumstellar disk. By combining observations of gas and ice compositions, we can begin to understand the chemical evolution from quiescent molecular clouds to protostars.

Table of Contents

Acknowledgments	v
Abstract	viii
List of Tables	xii
List of Figures	xiv
Chapter 1. Introduction	1
1.1 Current State of the Field	3
1.1.1 Studies of Cold Molecular Clouds	3
1.1.2 Massive Star Formation	6
1.2 Description of Chapters	8
Chapter 2. Spitzer Mid-Infrared Spectroscopy of Ices toward Extincted Background Stars	10
2.1 Introduction	10
2.2 Observations and Reduction	11
2.3 Results	14
2.3.1 CO ₂ and H ₂ O Ices	14
2.3.2 The 6.85 μm Band	17
2.3.3 Other Ices and Hydrogen Column Densities	20
2.4 Conclusions	22
Chapter 3. Probing the Emerging Hot Core in AFGL 2591 Through Absorption of C₂H₂ and HCN	25
3.1 Introduction	25
3.2 Observations	29
3.3 Spectrum Fitting	31

3.3.1	Properties of the Absorbing Gas	37
3.4	Models	42
3.4.1	Physical Models	42
3.4.2	Chemical Models	44
3.5	Conclusions	46
Chapter 4. High Resolution Mid-Infrared Spectroscopy of NGC 7538 IRS 1: A UV-Illuminated Protostellar Disk?		49
4.1	Introduction	49
4.2	Observations	55
4.2.1	Observations and Data Reduction	55
4.2.2	New Infrared Detections	56
4.3	Spectrum Fitting	82
4.3.1	Method	82
4.3.2	Results	90
4.3.3	C ₂ H ₂ and HCN	91
4.3.4	NH ₃	97
4.3.5	HNCO	98
4.3.6	CH ₃	100
4.3.7	CH ₄ and CS	100
4.4	Models	102
4.4.1	Physical Models	102
4.4.2	Chemical Models	105
4.5	Conclusions	111
Chapter 5. Summary		113
Appendix		119
Appendix 1. Spectroscopy of CH₃ and HNCO		120
Bibliography		122
Vita		131

List of Tables

2.1	Column Densities and Abundances	16
3.1	Observed Lines	33
3.2	Results from the model	38
3.3	Abundances with respect to CO and H ₂	42
3.4	$N(X)/N(H_2)$ From Chemical Models	46
4.1	Summary of Observed Lines	63
4.2	Observed Lines	64
4.2	Observed Lines	65
4.2	Observed Lines	66
4.2	Observed Lines	67
4.2	Observed Lines	68
4.2	Observed Lines	69
4.2	Observed Lines	70
4.2	Observed Lines	71
4.2	Observed Lines	72
4.2	Observed Lines	73
4.2	Observed Lines	74
4.2	Observed Lines	75
4.2	Observed Lines	76
4.2	Observed Lines	77
4.2	Observed Lines	78
4.2	Observed Lines	79
4.2	Observed Lines	80
4.2	Observed Lines	81
4.2	Observed Lines	82
4.3	Results from the model fit to the spectra	89

4.4	Abundances with respect to CO and H ₂	96
4.5	$N(X)/N(\text{CO})$ from chemical models	108

List of Figures

1.1	The chemical evolution in low mass protostars	4
2.1	1–20 μm spectra of CK 2, Elias 16, and Elias 13	13
2.2	CO ₂ feature toward CK 2, Elias 16 and Elias 13	17
2.3	5–20 μm optical depth spectra of CK 2, Elias 16, Elias 13 . . .	18
2.4	Spectra of background stars after removing contribution from silicates	19
2.5	The 6.85 μm feature toward CK 2 and Elias 16	21
3.1	C ₂ H ₂ and HCN lines toward AFGL 2591 with the best-fit model	32
3.2	Cartoon of the two components used in model	35
3.3	Fit to AFGL 2591 observations using parameters from Carr et al. (1995)	40
4.1	Selected orders between 729 and 870 cm^{-1}	59
4.2	Selected orders between 1245 and 1285 cm^{-1}	60
4.3	Forrest of HNC and NH ₃ lines toward NGC 7538 IRS 1 . . .	61
4.4	Blow-up of HNC and NH ₃ lines	62
4.5	Illustration of two component model	84
4.6	Our fit compared to <i>ISO</i> spectrum	93
4.7	Cartoon representation of the NGC 7538 IRS 1 region	103

Chapter 1

Introduction

Were the chemical conditions for the formation of life on Earth unique or are they common throughout the galaxy? What was the origin of pre-biotic material on the early Earth? Many lines of evidence suggest the possibility that the precursor molecules for life had an extraterrestrial origin. During the early stages of our Solar System, the Earth was frequently bombarded by interplanetary bodies rich in volatiles, such as water and organic material (Irvine 1998). Complex organic compounds of biological interest, including amino acids, are found in some meteorites (Botta & Bada 2002), and comets are known to contain numerous organic molecules (Crovisier 2004). A large number of molecules of pre-biotic importance, such as simple sugars, have also been observed in the interstellar medium. Hence, the chemical seeds necessary for the emergence of life are common in the Solar System and beyond.

Tracing the origin and chemical evolution of organic and pre-biotic molecules is a fundamental goal of astrobiology. The journey likely begins in interstellar molecular clouds, where many simple molecules can be formed via gas-phase reactions. Within dense, cold clouds, many molecules freeze-out onto the surfaces of dust grains, and subsequent reactions on the grain

surfaces lead to the formation of more complex molecules. When molecular clouds collapse to form protostars, icy grain mantles are subjected to heating and irradiation, which trigger further reactions and changes in composition (Gerakines et al. 1996; Ehrenfreund & Charnley 2000; Schutte & Khanna 2003). Molecules formed on grains that sublime into the gas phase can then drive a rich gas-phase chemistry that can produce larger organic molecules. As protostars develop from the infalling cloud core, they form circumstellar disks, which are the reservoirs of material from which planetary systems form. Material incorporated into a disk is subjected to further processing, including irradiation by X-rays and UV light from the newly formed star.

Understanding the chemical evolution of organic molecules requires a detailed accounting of the processing which material undergoes as it evolves from cold molecular clouds, to star-forming cores, to planet-forming disks. van Dishoeck & Blake (1998) present a cartoon of the chemical evolution during star formation (see Figure 1.1). In this dissertation, I describe the work aimed at understanding some important stages in the chemical evolution related to the formation of massive stars: 1) the chemical composition of ices in cold molecular clouds (which later collapse to form high and low mass stars), 2) the chemical enhancement of organic material in hot cores around massive protostars, and 3) the organic composition of material in a circumstellar disk around a high mass star. The composition of molecular clouds prior to star formation (quiescent clouds) provides the initial conditions that affect the subsequent chemistry occurring during the star and planet formation process

and is the baseline for comparison of ice compositions towards star-forming cores and in comets. Once collapse ensues and the protostar begins to heat its environment, small regions ($d \leq 0.1$ pc) of dense ($n \geq 10^7$ cm $^{-3}$) and hot ($T \geq 100$ K) gas become enriched by the recently sublimated icy grain mantles (Kurtz et al. 2000). These regions lie close to the protostars and are known as hot cores. Once material is somewhat cleared out by the emerging protostar, it may be possible to observe the material in a circumstellar disk around a massive protostar. Because massive protostars are intrinsically brighter than solar-type stars, infrared observations of high mass stars are easier to obtain than for low mass stars.

1.1 Current State of the Field

1.1.1 Studies of Cold Molecular Clouds

The chemical composition of molecular clouds can be studied with spectroscopy at millimeter and sub-millimeter (henceforth radio) and infrared wavelengths. The gas composition has been studied mostly through line emission at radio wavelengths, since the low energy rotational transitions, which can be excited at low temperatures, occur at these wavelengths. Radio observations can be used to determine gas parameters such as temperature, density, and abundances for different regions of molecular clouds.

In the coldest and densest regions of molecular clouds, however, molecules can be efficiently depleted from the gas-phase onto grain surfaces. This means that radio measurements provide an incomplete picture of the total molecular

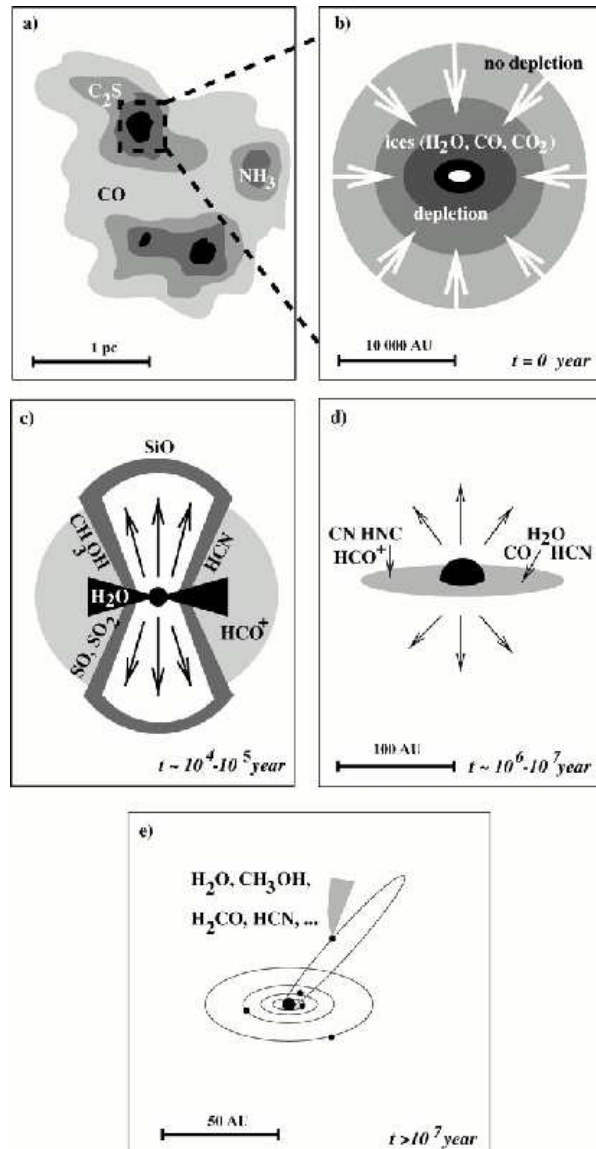


Figure 1.1 This figure taken from van Dishoeck & Blake (1998) shows a cartoon representation of the chemical evolution from molecular cores to protoplanetary disks. This depiction illustrates depletion of molecules onto dust grains at low temperatures and early stages of evolution. Subsequently, the sublimation of molecules occurs as protostars heat up the surroundings. Reprinted, with permission, from the Annual Review of Astronomy and Astrophysics, Volume 36 (c) 1998 by Annual Reviews www.annualreviews.org.

composition. Furthermore, grain surfaces become chemical catalysts that may produce many complex organic molecules. For these reasons, studying the ice (solid-state) composition in molecular clouds is a critical part of following the chemical evolution of organics.

Because molecules in the solid state cannot rotate, the ice content in molecular clouds must be studied using vibrational transitions, which occur in the infrared. This is accomplished using absorption spectroscopy, which measures the column density along a line of sight to an infrared continuum source. Due to sensitivity limitations, observations of ices toward molecular clouds had been limited to lines of sight to infrared-bright protostars embedded in cloud cores. Furthermore, ground-based observations were mostly limited to ice bands below $5\ \mu\text{m}$ due to absorption by the Earth's atmosphere. However, observations of ices in molecular clouds became more feasible with the *Infrared Space Observatory* (*ISO*; Kessler et al. 1996), and abilities increased further with the launch of the *Spitzer Space Telescope* (Werner et al. 2004). The space-based observatories are not hindered by the Earth's atmosphere and are cooled to very low temperatures to reduce noise from the telescope itself.

Probing the “pristine” cloud material (before stars form) requires observations of normal stars behind molecular clouds (background stars), which are difficult because the flux of a star decreases sharply with increasing wavelength in the region of the ice bands. Even with *ISO*, ice composition studies were restricted mostly toward high-mass young stellar objects because they are bright infrared sources. The increased sensitivity of the Infrared Spectrograph

(IRS; Houck et al. 2004) aboard *Spitzer* allows for the study of solid-state features toward faint objects and provides important new opportunities. One is the ability to observe weak ice features toward low-mass protostars (Boogert et al. 2004b), which means we can study environments similar to the ones that formed our Solar System. The other is the opportunity to investigate the ice composition in quiescent molecular clouds. This can be done by observing many lines of sight toward stars behind molecular clouds (Ch. 2, Knez et al. 2005; Bergin et al. 2005).

1.1.2 Massive Star Formation

A general sequence has been developed to explain the formation of a low mass stars based on the spectral energy distribution (SED) (see Lada et al. 1984; Lada 1987). However, there has been very little progress in the case of high mass star formation. Similar classification schemes have been attempted for high mass star formation, but no clear correlation between the SED and the evolutionary stage has been determined (van der Tak et al. 2000). Massive stars reach the main sequence before they stop accreting material, meaning that the material around the star has not been cleared away, thus obscuring the forming star (Stahler et al. 2000). In addition, massive stars form only in clusters, making it difficult to isolate each star's SED. So the measured SEDs are not an accurate indicator of the evolutionary stage of the core. Lada (1987) describes the uncertain evolution of massive stars in giant molecular clouds.

Regions of high mass star formation provide laboratories in which to

study chemistry on dust grains at cold temperatures. As protostars heat the surrounding gas, the ice mantles on dust grains evaporate. By studying molecules which evaporate from grains, we can learn about the low-temperature, chemical processes that occur on the surface of grains (van Dishoeck & van der Tak 2000). In the cold-prestellar and collapse phases, molecules are frozen onto dust grains, forming icy mantles. Grain surface reactions and ultraviolet photolysis can then alter the mantle composition. Then, as the protostar begins to warm the surrounding gas, the ices sublime and return to the gas phase. A rich chemistry is driven by these newly sublimated molecules in compact, optically thick hot cores. Hot cores typically have densities $\geq 10^7$ cm^{-3} , diameters ≤ 0.1 pc, and temperatures ≥ 100 K (Kurtz et al. 2000). High abundances of fully hydrogenated molecules such as NH_3 , H_2S , and H_2O and saturated complex organic molecules such as CH_3OH , CH_3CN , CH_3OCH_3 are characteristic of hot cores.

Mid-infrared absorption spectroscopy, along with radio spectroscopy, is a powerful probe of the physical conditions and chemical abundances in molecular clouds. Most radio spectroscopy involves emission spectra, where the angular resolution is set by the size of the beam, which varies with frequency and with telescope. However, in infrared absorption spectroscopy, the spatial resolution is set by the size of the background source. For this case, embedded protostars serve as the background source, and small scales in star forming regions are probed for all excitation levels. In addition, mid-infrared spectroscopy can be used to study symmetric molecules like acetylene, C_2H_2 ,

methane, CH₄ (Lacy et al. 1989b; Evans et al. 1991; Carr et al. 1995), and methyl, CH₃, which do not have a permanent dipole moment and, therefore, no pure rotational transitions. The study of ro-vibrational transitions allows for the sampling of populations for many rotational levels with a single instrument, often simultaneously, therefore reducing the calibration problems encountered in radio observations. Previous infrared spectroscopy has been limited by low to medium spectral resolution (i.e. $R \sim 2000$ for the Short Wavelength Spectrometer (SWS) on board the *Infrared Space Observatory* (ISO; Kessler et al. 1996) and $R \sim 10^4$ for Irshell, a previous ground-based moderate resolution instrument (Lacy et al. 1989a)). We now have a new instrument, the Texas Echelon Cross Echelle Spectrograph (TEXES) (Lacy et al. 2002), that achieves $R \approx 75,000$ at 13 μm , or $\delta v \sim 4 \text{ km s}^{-1}$, allowing the resolution of long-standing questions such as velocity structure of gas close to the forming star.

1.2 Description of Chapters

The subsequent chapters describe research aimed at addressing some of the questions regarding the chemical evolution of organic material. In Chapter 2, I describe studies of icy material toward background stars. I, then, describe the effects of sublimation of icy mantles in the hot core phase of the high-mass protostar AFGL 2591 in Chapter 3. Chapter 4 describes the chemistry of a UV-illuminating disk around high-mass protostar NGC 7538 IRS 1. The last Chapter (Ch. 5) gives concluding remarks on the results from the previous

chapters. The goal of this research is to lay the foundation for chemical studies of environments around lower mass protostars where planets are likely to form. Because protoplanetary disks are the sites of planet formation, understanding the chemistry and composition of disks at the time planets form provides insight into the availability of pre-biotic material in the early Solar System.

Chapter 2

Spitzer Mid-Infrared Spectroscopy of Ices toward Extincted Background Stars

2.1 Introduction

Infrared absorption studies of protostars embedded in dense clouds have shown that dust grains along these lines of sight have icy mantles (e.g., Willner et al. 1982; Tielens et al. 1984; Allamandola et al. 1992; Whittet et al. 1996; Boogert et al. 2004b). Heating by the protostar and energetic photons can affect the ice composition by sublimation and by triggering chemical reactions (e.g., Gerakines et al. 1996; Ehrenfreund & Charnley 2000; Schutte & Khanna 2003). Knowledge of the ice composition in quiescent dense clouds is required in determining the amount of processing ices undergo during star formation. This ‘baseline’ can be obtained by observations of field stars lying behind molecular clouds. These observations also help constrain models of chemical evolution during the star forming process (e.g., Lee et al. 2004).

The $3\ \mu\text{m}$ absorption band of H_2O ice was observed toward stars behind the Serpens (Eiroa & Hodapp 1989) and Taurus dark clouds (Whittet et al. 1988; Smith et al. 1993; Murakawa et al. 2000). These studies indicate that H_2O ice is formed deep in the clouds, at visual extinctions $A_V > 3$ magnitudes

(the ice formation threshold). Solid CO was observed toward background stars as well (e.g., Whittet et al. 1985; Chiar et al. 1994, 1995). Its formation threshold is significantly larger ($A_V=6-15$ mag) due to the lower sublimation temperature of solid CO.

Studies of ices toward background stars have been limited to bands below $5 \mu\text{m}$ because of telluric absorption and the fact that stellar fluxes drop rapidly with increasing wavelength. Observations of background stars have become increasingly feasible with the *Infrared Space Observatory (ISO)* mission and, in particular, with the launch of the *Spitzer Space Telescope* (Werner et al. 2004). With *ISO*, solid CO_2 at $4.25 \mu\text{m}$ was observed toward two Taurus background stars (Whittet et al. 1998; Nummelin et al. 2001), indicating that radiation from nearby protostars is not required to form this species. Recent observations with *Spitzer* detected the CO_2 bending mode at $15 \mu\text{m}$ toward background stars (Bergin et al. 2005). Here we present observations of ices toward three background stars over the full $5-20 \mu\text{m}$ range taken with the Infrared Spectrograph (IRS; Houck et al. 2004) aboard *Spitzer*. We assess the complete ice inventory in quiescent clouds and compare it to observations toward protostars.

2.2 Observations and Reduction

The background stars discussed here include a source behind the Serpens dark cloud, CK 2, and two sources behind the Taurus dark cloud, Elias 13 and Elias 16. The observations are part of the “c2d” legacy program (Evans

et al. 2003). All sources were observed with the short wavelength, low resolution module (SL; $\lambda = 5\text{-}14 \mu\text{m}$; $R \equiv \lambda/\Delta\lambda = 64\text{-}128$), with on-source integration times of 28 sec per spectral order. CK 2 and Elias 13 were also observed with the short wavelength, high resolution module (SH; $\lambda = 10\text{-}20 \mu\text{m}$; $R = 600$), with integration times of 240 sec and 60 sec per spectral order, respectively. Spectra of Elias 13, Elias 16 and CK 2 were part of AOR# 0005636864, 0005637632, and 0011828224. The SH spectrum of Elias 16 has been published by Bergin et al. (2005) and was part of AOR# 0003868160. The data were reduced using the *Spitzer* Science Center (SSC) pipeline version S11.0.2 (S12 for SH in Elias 16) to produce the 2-dimensional Basic Calibrated Data. Subsequently, customized source extractions were performed, including the subtraction of extended background emission. The spectra were then de-fringed with sine-wave fitting routines (Lahuis & Boogert 2003).

Figure 2.1 shows the *Spitzer* spectra of the observed background stars, complemented by near-infrared (NIR) broad band photometry (2MASS¹). In addition, for CK 2, *Spitzer* IRAC (S. T. Megeath, priv. comm.) and ground-based L' band photometry (Churchwell & Koornneef 1986) are included and for Elias 16 the 2-5 μm *ISO* spectrum is shown (Whittet et al. 1998).

In order to put the data on an optical depth scale and analyze the ice and dust features, each spectrum is normalized to the spectrum of an

¹This publication makes use of data from the Two Micron All Sky Survey, which is a joint project of the University of Massachusetts and IPAC/Caltech, funded by NASA and NSF.

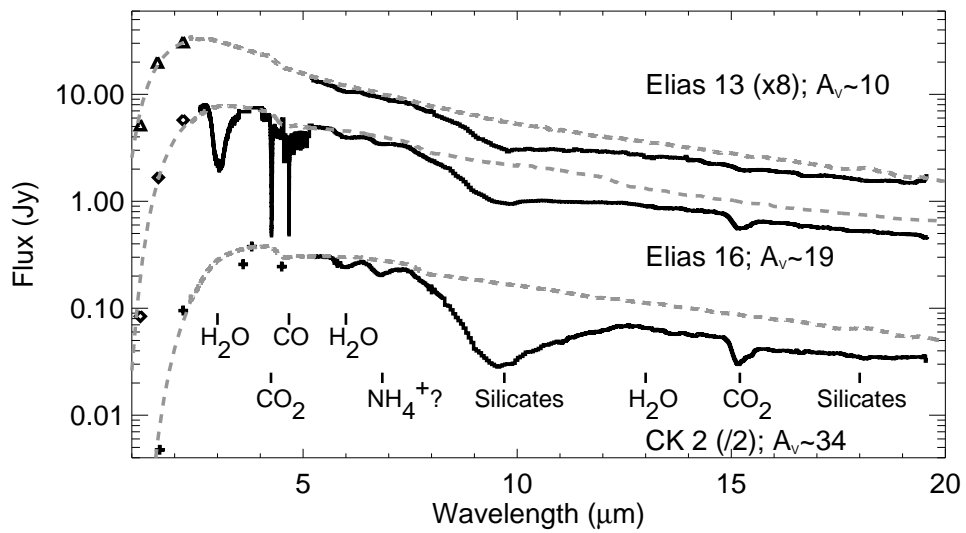


Figure 2.1 The spectra of Elias 13, Elias 16 and CK 2 with the extinguished photospheres (dashed lines) used for normalization. Near-infrared complementary data are shown in triangles, diamonds and plus signs, respectively. The spectra are scaled along the flux axis by the numbers given in brackets.

extincted late-type giant taken from the *ISO* database (Sloan et al. 2003). A blackbody is used at wavelengths below $2.5 \mu\text{m}$ to fit the NIR photometry. The extinction law used for Serpens is of the form $A_\lambda \sim \lambda^{-1.9}$ (Kaas et al. 2004), whereas that for Taurus has a shallower power law, $A_\lambda \sim \lambda^{-1.7}$ (Whittet et al. 1988). Indebetouw et al. (2005) find a shallower slope on the extinction curve beyond $6 \mu\text{m}$. This flattening is partly due to the silicate and ice features which we account for separately and the powerlaw is a good approximation to the extinction at longer wavelengths. A_V is taken to be $9.1 \times A_K$ (Rieke & Lebofsky 1985). Spectral types K4 III, G9 III, and K3 III were adopted for CK 2, Elias 13 and Elias 16, respectively. These values are within the range of types given in Chiar et al. (1994) for CK 2 and close to the K2 III type assigned by Smith et al. (1993) for Elias 13 and 16. While the selected spectral types give the best fit (in removing the photospheric CO and SiO bands at 5 and $8 \mu\text{m}$), they are uncertain by a few subclasses resulting in an abundance error of 20% on the strong features, especially since the available *ISO* database has limited coverage.

2.3 Results

2.3.1 CO₂ and H₂O Ices

The CO₂ $15 \mu\text{m}$ feature is very strong toward CK 2 and Elias 16, and weakly detected toward Elias 13 (Table 2.1). The abundance of CO₂ relative to H₂O is 33% toward CK 2, higher than the $\sim 20\%$ abundance seen toward the Taurus sources. The derived CO₂ column densities toward Elias 13 and 16

agree within errors with those obtained from the 4.25 μm feature (Nummelin et al. 2001). The bottom of the 15 μm CO_2 feature appears single peaked toward all sources (Fig. 2.2) and does not show double dips due to crystallization as some protostars do (Gerakines et al. 1999; Boogert et al. 2004b). The profile of this band toward Elias 16 is fitted in Bergin et al. (2005) with the sum of polar ($\text{H}_2\text{O}:\text{CO}_2=7:1$) and apolar ($\text{CO}:\text{CO}_2=4:1$) mixtures. The polar, H_2O -rich mixture accounts for 85% of the CO_2 column density. However, the H_2O column density assumed in this fit overestimates the observed value by 30%. We require that both the observed H_2O and CO_2 column densities, as well as the CO_2 band profile are matched. We use a combination of two polar mixtures $\text{H}_2\text{O}:\text{CO}_2=1:1$ and $\text{H}_2\text{O}:\text{CO}_2=10:1$ (with the ratios of the two mixtures: 2:1 for CK 2, 1.3:1 for Elias 16 and 1:0 for Elias 13) and the apolar mixture $\text{CO}:\text{N}_2:\text{CO}_2=100:50:20$, all at low temperature (Ehrenfreund et al. 1997). Satisfactory fits are obtained for polar fractions of 78% in CK 2, 84% in Elias 16, and 87% in Elias 13, comparable to the fractions found by Bergin et al. (2005) despite the different mixtures used.

Using the H_2O ice column densities from the 3 μm band (Table 2.1) and laboratory spectra of pure H_2O ice (Hudgins et al. 1993), the H_2O bending mode contributes 77% and 69% of the observed 6.0 μm absorption feature for Elias 16 and CK 2 (Fig. 2.3). However, the peak position, width, and strength of this band change significantly when H_2O is diluted. For example, compared to pure H_2O , the mixture $\text{H}_2\text{O}:\text{CO}_2=1:1$ shifts the peak to longer wavelengths by $\sim 0.1 \mu\text{m}$, and increases the peak by a factor of 2.4, but the extensive long

Table 2.1. Column Densities and Abundances

Species	Unit	CK 2	EL 13	EL 16	HH46 ¹	B5 ¹
CO	%H ₂ O	36 ² , 57 ³	9 ⁴	26 ⁴	20	43
CO ₂	%H ₂ O	33	≤15, 22 ⁵	18 ⁵ ,22 ⁶ , 19 ⁷ ,24	32	37
HCOOH	%H ₂ O	1.9	<8.7	9.3
CH ₃ OH	%H ₂ O	<2.1	<0.8	<2.3	7.0	< 2.3
NH ₃	%H ₂ O	≤8	<6	≤8	17	<9.1
NH ₄ ⁺	%H ₂ O	10.8	...	5.5	9.6	<12.7
CH ₄	%H ₂ O	<3	...	<3	4	...
OCN ⁻	%H ₂ O	<2.3 ⁸	≤0.7	<0.5
H ₂ O	10 ¹⁸ cm ⁻²	3.5 ⁹	1.0 ¹⁰	2.5 ¹⁰	8.4	2.6
H	10 ²² cm ⁻²	6.4	1.9	3.6	5.0	3.2

References. — 1. HH46 IRS and B5 IRS1 from Boogert et al. 2004b, and in preparation; 2. Chiar et al. 1994; 3. Pontoppidan et al. 2003; 4. Chiar et al. 1995; 5. Whittet et al. 1998; 6. Nummelin et al. 2001; 7. Bergin et al. 2005; 8. Whittet et al. 2001; 9. Eiroa & Hodapp 1989; 10. Whittet et al. 1988; Smith et al. 1993

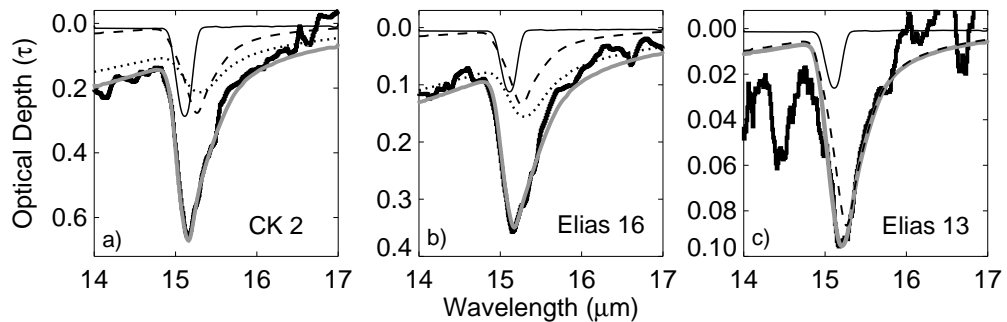


Figure 2.2 CO₂ feature for a) CK 2, b) Elias 16 and c) Elias 13 compared to laboratory spectra composed of H₂O:CO₂=10:1 (dot) and 1:1 (dash) at 10 K and CO:N₂:CO₂=100:50:20 (thin solid) at 30 K. The grey line shows the best composite fit. Note that the vertical offset is due to the H₂O libration mode.

wavelength wing remains unchanged. Using mixtures that fit the 15 μm CO₂ band (Fig. 2.2), $\sim 85\text{-}100\%$ of the 6.0 μm feature can be explained by H₂O (Fig. 2.4). The strong libration mode of H₂O explains much of the excess absorption in the 12-13 μm region, but due to severe blending with the silicate absorption feature, residuals in that spectral region are hard to interpret (Ch. 2.3.3). A model of astronomical silicates (Weingartner & Draine 2001) is used to fit the 10 and 20 μm features for all sources (Fig. 2.3), but this silicate model may not be unique.

2.3.2 The 6.85 μm Band

A strong feature at 6.85 μm is detected toward CK 2 and Elias 16 but not toward Elias 13. This is the first detection of this band toward background stars. It is commonly observed toward protostars (Keane et al. 2001) and often

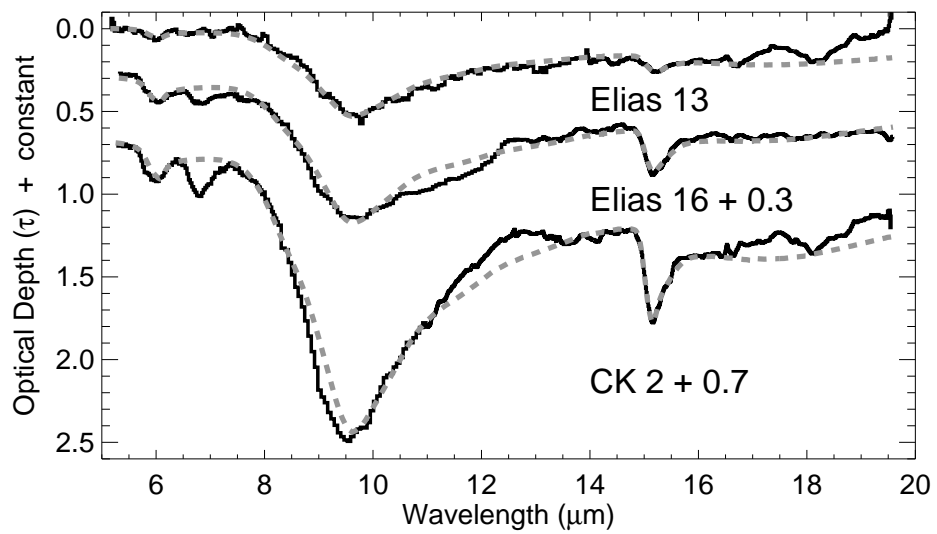


Figure 2.3 Background star spectra on optical depth scale (black). A fit (dashed grey) of small spherical silicate grains is shown to which are added laboratory spectra of H_2O and CO_2 (at $15 \mu\text{m}$) at opacities corresponding to the column densities mentioned in Table 2.1.

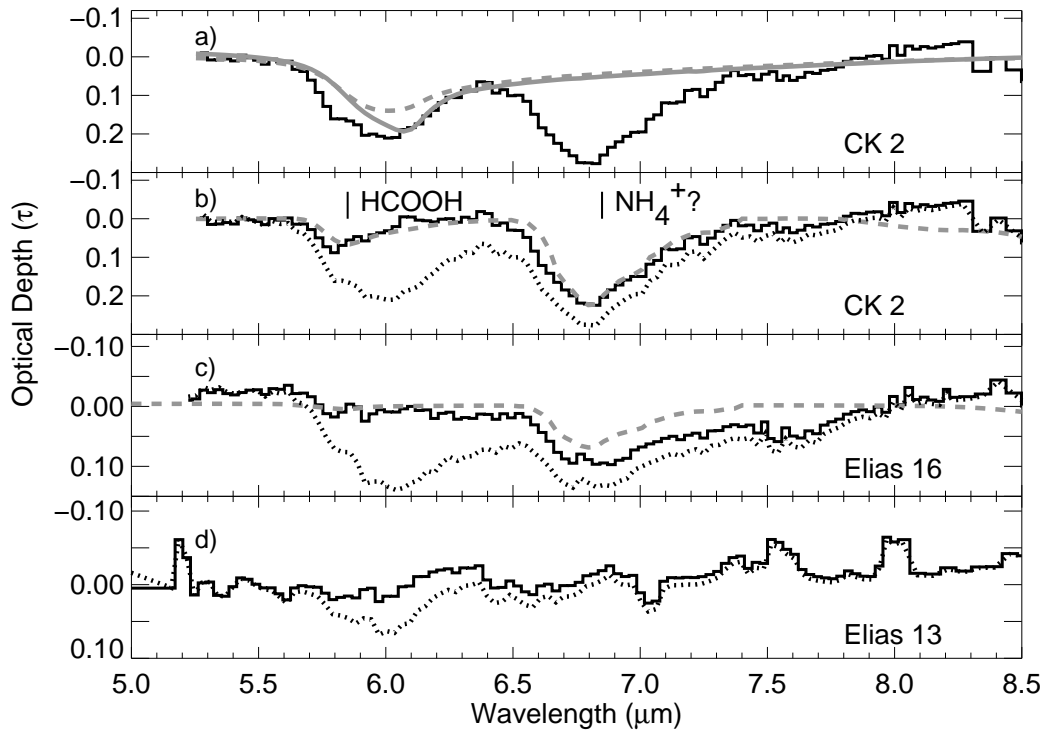


Figure 2.4 a) The spectrum of CK 2 after removing silicate absorption is shown in black. The dashed grey line is the pure H₂O-ice contribution to the 6.0 μm feature while the solid grey is the H₂O:CO₂ mixture. b-d) The dotted lines show the spectra after removing the silicate contribution. The solid lines show the spectra after removing silicate and H₂O contributions. b) For CK 2, the dashed grey line shows a fit to HCOOH (5.85 and 8.2 μm), NH₄⁺ (6.85 μm) and NH₃ (6 μm). c) For Elias 16, the dashed grey line shows a fit to NH₄⁺ and NH₃. d) For Elias 13, no remaining features are found.

attributed to the NH_4^+ ion (see Schutte & Khanna 2003, Ch. 2.4). Regardless of the identification, the profile may be a powerful tracer of the thermal history of the ices. Figure 2.5 shows the decomposition of the $6.85 \mu\text{m}$ feature into the short and long wavelength components used by Keane et al. (2001) to characterize this band. The phenomenological separation is meant to represent NH_4^+ bands at different temperatures. The ratio of the peak optical depths of the two components (short/long) is 2 for Elias 16 and 1.2 for CK 2. If instead the equivalent widths are compared, the ratios are 1.6 and 0.9, respectively. In either case, the profiles resemble those of the protostars with the coldest sight-lines (e.g., NGC 7538 IRS9). Its equivalent width is used to calculate the column density for NH_4^+ (Table 2.1) using the band strength from Schutte & Khanna (2003).

2.3.3 Other Ices and Hydrogen Column Densities

H_2O ice accounts for up to 85% of the $6.0 \mu\text{m}$ absorption band for CK 2 (Fig. 2.4; Ch. 2.3.1). Some excess absorption remains, in particular on the short wavelength side. This is observed towards protostars as well, and attributed in part to absorption by HCOOH (Schutte et al. 1999; Keane et al. 2001). The $5.85 \mu\text{m}$ band is the strongest HCOOH band in our observed wavelength range; that at $8.2 \mu\text{m}$ is slightly weaker. For CK 2, the laboratory spectrum of pure solid HCOOH fits the $5.85 \mu\text{m}$ feature with a discrepancy at $8.2 \mu\text{m}$, which may indicate over-correction of the photospheric SiO band (Ch. 2.2). Table 2.1 shows upper limits and tentative detections of weak features

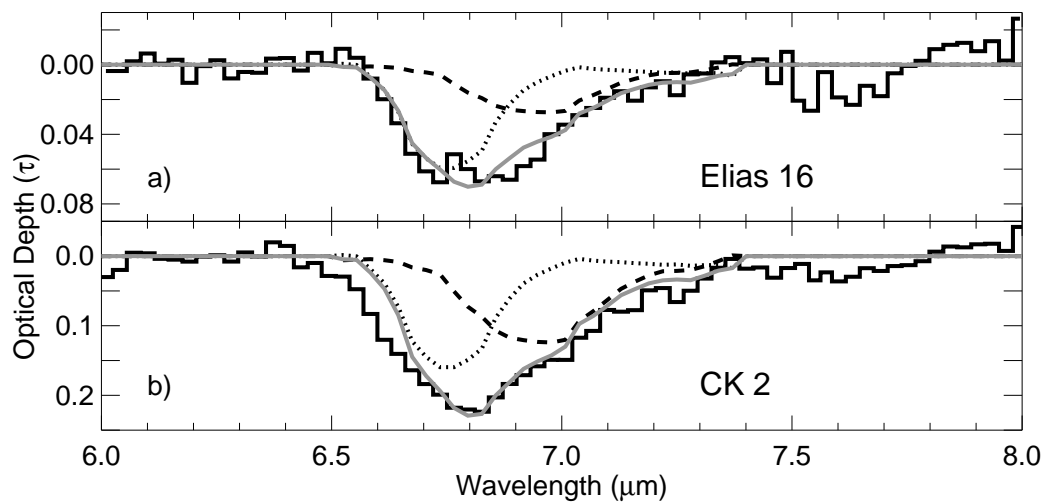


Figure 2.5 The decomposition of the 6.85 μm feature into short (dot) and long wavelength (dash) components (Keane et al. 2001) for a) Elias 16 and b) CK 2. The solid grey line indicates the sum of the short and long wavelength components. The solid black line represents the spectrum after subtraction of silicate and H₂O contributions.

in the 7–13 μm spectral region.

The uncertainty in the shape of the silicate feature is large in some places (e.g., 20% at 10–13 μm) and hard to quantify in others. For ice abundance determinations, the hydrogen column density is usually calculated from the relation $N_{\text{H}} \approx 1.87 \times 10^{21} \times A_{\text{V}} \text{ cm}^{-2}$ for $R_{\text{V}} = 3.1$ (Draine 2003). As outlined in Ch. 2.2, by fitting *ISO* template spectra, extinctions A_{V} of 34^m , 19^m , and 10^m are derived for CK 2, Elias 16, and Elias 13 respectively. The observed peak optical depth of the silicate band and the relation $A_{\text{V}}/\tau_{9.7} = 18.5 \pm 2$ (Draine 2003) give similar values for A_{V} . The N_{H} values listed in Table 2.1 are calculated using the A_{V} values derived from the photospheric fits.

2.4 Conclusions

Our *Spitzer* spectra of background stars show clear detections of absorption features at 6.0 and 6.85 μm that had previously been seen only toward YSOs, imposing new constraints on the origin of the 6.85 μm band. The strength of the 6.85 μm band, scaled to H_2O , is similar to that seen toward YSOs, as is the factor of 2 variation between sight-lines (Table 2.1; Schutte & Khanna 2003). In one scenario, the 6.85 μm band is explained by NH_4^+ produced by acid-base reactions in ice mixtures containing NH_3 and HNCO . In laboratory experiments such reactions occur at temperatures as low as 10 K with conversion factors between 15% and 100% depending on ice mixtures and temperature (van Broekhuizen et al. 2004). The strength of the 6.85 μm band is a factor of 2 larger toward CK 2 compared to Taurus. This sight line probes

a very cold region, as evidenced by the very high abundance of the volatile apolar CO ice ($T_{\text{subl}} \sim 20$ K) as well as the smooth profile of the $15 \mu\text{m}$ CO₂ band. In contrast, the line of sight of the YSO HH46 IRS shows evidence for the ices to have undergone thermal processing (Boogert et al. 2004b), but the $6.85 \mu\text{m}$ band is not unusually deep (Table 2.1). Thus, if the $6.85 \mu\text{m}$ band is due to NH₄⁺, variables other than temperature, such as the initial HNCO and NH₃ abundances, must play roles in determining its strength. We stress that the identification of the $6.85 \mu\text{m}$ band with NH₄⁺ is tentative and more evidence, including correlation with the bands of counter ions such as OCN⁻ (van Broekhuizen et al. 2005) or HCOO⁻ is required.

Most ($\sim 75\%$) of the $6.0 \mu\text{m}$ band toward background stars is explained by pure H₂O ice, comparable to the percentage toward most massive YSOs (Keane et al. 2001). While H₂O mixed with CO₂ can explain the remaining absorption in the Taurus sources, the residual toward CK 2 has a peak absorption wavelength consistent with HCOOH (Fig. 2.4). Its abundance would be a few % of H₂O, comparable to that seen in several high-mass YSOs (Keane et al. 2001) but not as high as seen in some low-mass YSOs (Boogert et al., in preparation).

Dust grains have accumulated rather complex icy mantles in opaque regions of molecular clouds before star formation begins, a point which must be included in models of star formation. Also, the effect of freeze-out on the thermal balance has been studied by Goldsmith (2001). For the two stars with extinctions above 15 mag, the abundances relative to H₂O ice are within

the range seen toward embedded objects. From the abundances in Table 2.1, the percentages of nitrogen, oxygen and carbon locked in ices for Elias 16 and CK 2 are 35-37% N, 28-30% O and \sim 12% C. Further work on larger samples of background stars will elucidate the dependence of the ice composition on cloud conditions and history. Such surveys are now possible with *Spitzer*/IRS for sources as weak as 10 mJy (9.5 mag) at 8 μ m and A_V of up to 50 mag.

Chapter 3

Probing the Emerging Hot Core in AFGL 2591 Through Absorption of C₂H₂ and HCN

3.1 Introduction

Determining the evolutionary stages of massive protostars is difficult because they tend to form in clusters. One possible exception is AFGL 2591 (van der Tak et al. 1999), which has been the target of extensive studies. From the depth of the silicate feature studied by Willner et al. (1982), the visual extinction toward this source is ~ 70 magnitudes. At a distance of 1 kpc (Mozurkewich et al. 1986), the luminosity of this object is $\sim 3 \times 10^4 L_{\odot}$ (Merrill & Soifer 1974). However, the distance to this object is very uncertain (see van der Tak et al. 1999, and references therein).

A molecular outflow was observed in the region (Torrelles et al. 1983) which originates from the infrared source (Lada et al. 1984). Campbell (1984a) looked for radio continuum emission in the region and found 4 sources, none of which are coincident with the infrared source. Additionally, a shell-like structure is seen in near-infrared continuum emission (Forrest & Shure 1986) and in NH₃ (J, K) = (1,1) emission (Torrelles et al. 1989). Marengo et al. (2000) find that a second infrared source coincided with one of the radio sources

observed by Campbell as well as with the shell traced out by the near-infrared and NH_3 emission. Speckle interferometry showed that the loops traced by the near-infrared continuum and NH_3 line emission were made up of clumpy material (Preibisch et al. 2003).

Based on molecular radio emission, AFGL 2591 is not considered to have hot core chemistry (van Dishoeck & van der Tak 2000) since large abundances of complex molecules are not seen. However, hot material has been seen by Mitchell et al. (1989) with mid-infrared absorption. Hot cores are characterized by their small size ($r \leq 0.1$ pc), and dense ($n \geq 10^7$ cm^{-3}) and hot ($T \geq 100$ K) gas (Kurtz et al. 2000). The hot temperatures allow for a rich gas-phase chemistry to ensue after sublimation of icy grain mantles. It is possible that the hot core region is too small to be detected by single radio dishes (van Dishoeck & van der Tak 2000). We summarize below many of the gas phase observations of AFGL 2591 tracing hot, dense gas.

Mitchell et al. (1989) found cold ($T = 38$ K), warm ($T = 200$ K), and hot ($T = 1010$ K) CO components at -11 , -28 , and -8 km s^{-1} , as traced by ^{13}CO lines. They interpret the cold component as being the envelope surrounding AFGL 2591. The hot component is near the infrared source and warmed by radiation. There is a velocity difference between the absorption components and the CO emission ($V_{\text{LSR}} = -5$ km s^{-1}). Vibrationally excited ^{12}CO was also detected with a mean centroid velocity, $V_{\text{LSR}} = -9$ km s^{-1} , which agrees with the hot component seen in the ^{13}CO lines. Carr et al. (1995) presented mid-infrared observations of C_2H_2 , HCN, NH_3 , CS, SO, and

SiO. They fitted their C₂H₂ data with the two temperature components found by Mitchell et al. and found $N = 4.2 \times 10^{15} \text{ cm}^{-2}$ at 200 K and $N = 1.1 \times 10^{16} \text{ cm}^{-2}$ at 1010 K.

From radio observations of HCN and CS, the density power law ($n(r) = n_1 r_{pc}^{-\alpha}$) with $\alpha = 1.5$ is consistent with observations of both molecules. This density law fits the HCN data with a constant abundance $X(\text{HCN}) \sim 7 \times 10^{-10}$ with respect to H₂. Combining the radio and infrared observations of HCN, Carr et al. (1995) estimate the size of the infrared source to be 3'' for the $T = 200$ K and 2'' for the $T = 1010$ K.

Hot H₂O has been detected with the *Infrared Space Observatory (ISO)* toward AFGL 2591 (Helmich et al. 1996) $T_{\text{H}_2\text{O}} = 300$ K, $b = 7.5 \text{ km s}^{-1}$, $N(\text{H}_2\text{O}) = 2 \times 10^{18} \text{ cm}^{-2}$. Also, using *ISO* data, Lahuis & van Dishoeck (2000) observed absorption of C₂H₂ and HCN toward AFGL 2591. They fitted their data with a single excitation temperature for acetylene, $T_{ex}(\text{C}_2\text{H}_2) = 900$ K, with corresponding column density of $2 \times 10^{16} \text{ cm}^{-2}$. HCN was found to have a slightly lower temperature of 600 K with a column density of $4 \times 10^{16} \text{ cm}^{-2}$. These values were obtained by assuming a line width b of 5 km s^{-1} . Hot bands are observed in the *ISO* spectra which confirm the high temperatures (Lahuis & van Dishoeck 2000). A hint of a cold component is apparent especially in the C₂H₂ lines.

van der Tak et al. (1999) studied infrared absorption of CO as well as single dish and interferometric observations of line and continuum emission at radio wavelengths. In the infrared, they observed ¹³CO at $V_{\text{LSR}} = -5.7 \text{ km s}^{-1}$,

which does not match the velocities, $V_{\text{LSR}} = -8$ and -11 km s^{-1} found by Mitchell et al. (1989). Because the velocity measured by van der Tak et al. agrees with the millimeter emission lines, they assume the millimeter and infrared lines trace the same gas. Line shapes seen in the radio observations are not reproduced by the spherically symmetric envelope models. Models with a cavity (carved by an outflow) reproduce the data better by creating holes through which we can see deeper into the core and avoid self-absorption. From the radio interferometric observations of HCN, van der Tak et al. find that the HCN abundance remains constant at 10^{-8} with respect to H_2 down to a radius of $\sim 1500 \text{ AU}$, compared to the 10^{-9} abundance found for the envelope by Carr et al. (1995). Enhancement of HCN ($X(\text{HCN}) \sim 10^{-7}$) seen by Lahuis & van Dishoeck (2000) occurs within 175 AU from the star where $T > 300 \text{ K}$, based on models by van der Tak et al. (1999, 2000).

Boonman et al. (2001) find enhanced HCN abundances (10^{-6}) inside 350 AU from the central object based on the detection of vibrationally-excited HCN emission. At this radius the temperature is 230 K . The ground state $J = 9 \rightarrow 8$ rotational line has a line width of 5.8 km s^{-1} and a center velocity of -5.1 km s^{-1} . The line from the first vibrationally excited state has a line width of 4.4 km s^{-1} and a center velocity of -6.1 km s^{-1} .

Doty et al. (2002) and Stauber et al. (2004, 2005) used the physical model for the envelope of AFGL 2591 from van der Tak et al. (1999, 2000) to study the chemical evolution of the source. In the models presented by Doty et al., the predicted abundance was lower than observed by Carr et al. (1995),

Lahuis & van Dishoeck (2000), and Boonman et al. (2001). More recently, Stauber et al. (2004, 2005) studied the effects of UV and X-ray, respectively, on the HCN abundance, especially at small radii.

Despite the wealth of species and enhanced abundances observed, AFGL 2591 is not considered to have hot core chemistry because it lacks high abundance of complex organics such as CH_3OCH_3 and CH_3OCHO (see van Dishoeck & van der Tak 2000). In this paper, we postulate that AFGL 2591 has a hot core but the small size means that lines from complex organics observed with large beams are diluted and therefore an underestimate of the actual abundance, as previously suggested by Boonman et al. (2001). In Chapter 3.2, we discuss how the observations were obtained and reduced. Then, we describe the spectral fitting routine and the derived parameters (such as velocity, column density, and temperature) in Chapter 3.3. Chapter 3.4 describes physical and chemical models used to explain the observations. Finally, in Chapter 3.5, we summarize our results.

3.2 Observations

Observations were made with TEXES, the Texas Echelon Cross Echelle Spectrograph, on the NASA Infrared Telescope Facility (IRTF) in 2001 June and 2002 September. Much of the data was taken in less than ideal weather, but the observing conditions did not seriously affect the spectra except for increased noise, especially on atmospheric lines.

TEXES is a high-resolution cross-dispersed spectrograph operating at

mid-infrared wavelengths between 5 and 25 μm (Lacy et al. 2002). It achieves a spectral resolution of $R = 75,000$ ($\Delta v = 4 \text{ km s}^{-1}$) shortward of 14 μm with a slit width of $\sim 1.5''$. At each spectral setting 5-8 orders of the high resolution echelon grating are observed, giving a spectral coverage of $\sim 0.5\%$. At wavelengths longward of 11 μm the width of each order exceeds that of the array, leaving gaps in the observed spectra. The spatial resolution along the slit is $\sim 1''$, slightly larger than the diffraction limit of the IRTF. The spectral and spatial sampling by the 256×256 pixel Si:As detector array are 1.0 km s^{-1} and $0.35''$, respectively.

Observations of AFGL 2591 were interspersed with observations of the bright asteroid, Ceres, which served as a comparison source for removal of telluric absorption features. The telescope was nodded by $3\text{-}5''$, moving the source along the spectrograph entrance slit to allow subtraction of telluric emission. At the beginning of each set of nodded observations an ambient temperature blackbody was observed for flat-fielding.

Data reduction followed the standard TEXES procedure (Lacy et al. 2002) of first subtracting the two nod position spectra, flat-fielding with the blackbody-sky difference spectrum, and interpolating over spikes and bad pixels. Optimally-weighted point-source spectra were then extracted from the echelograms. The spectra were linearized in $\ln(\nu)$ based on the known optical distortions, and absolute wavenumber calibration was obtained from telluric emission features. The resulting wavenumber scale is correct to within 1 km s^{-1} . The same procedure was used for the asteroid spectra, and then the

AFGL 2591 spectra were divided by the asteroid spectra with correction for differences in airmass. With this procedure, telluric absorption lines as deep as 90% can be removed, although of course the noise increases on atmospheric lines. However, broad response variations often remained, which were removed by fitting the continuum in each echelon order to a quartic polynomial and dividing. This procedure also set the continuum in each order to one. This last step makes weak, broad lines (especially closely spaced lines) difficult to detect. Toward NGC 7538 IRS 1, another massive protostar, weak lines of HNC, CH₃, and NH₃ were detected in settings similar to the ones presented here (see Chapter 4). However, the lines toward IRS 1 are narrower than the lines observed toward AFGL 2591 so we could miss weak lines.

Four spectral settings were observed in the 740–785 cm⁻¹ (13.5–12.7 μm) region. A total of 29 echelon orders were observed. Many C₂H₂ hot band lines were detected in our spectra including lines from the $\nu_4 + \nu_5 - \nu_5$ and the $2\nu_5$ bands. A selection of spectra including all observed molecules is shown in Figure 3.1, along with fits described in Chapter 3.3. Table 3.1 shows all the lines identified.

3.3 Spectrum Fitting

To derive physical parameters of the absorbing gas, model spectra were fitted to the observations. All data were fitted simultaneously. The Marquardt fitting procedure (Bevington & Robinson 2003) was used, which minimizes χ^2 , the summed squared deviation normalized by the squared noise, between the

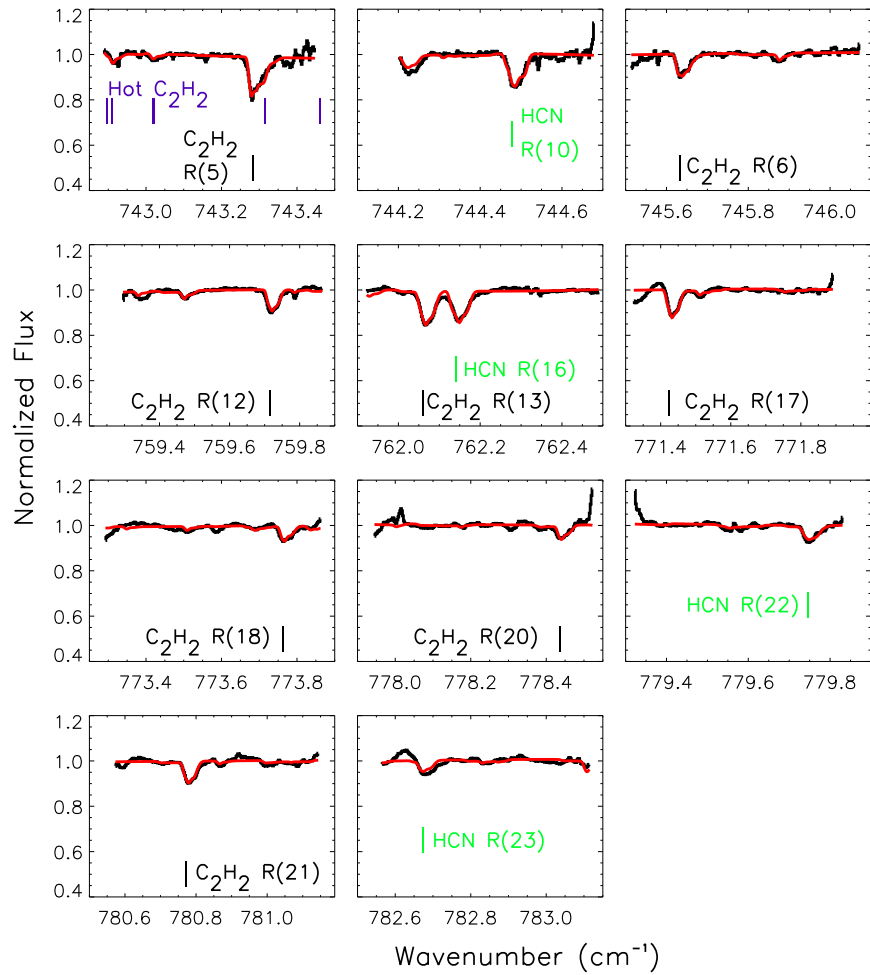


Figure 3.1 This figure shows the observed spectra in black with the best fit overlaid in red. The lines from the fundamental bands of C_2H_2 and HCN lines are labeled in black and green, respectively. The first panel shows hot band lines of C_2H_2 .

Table 3.1. Observed Lines

Molecule	Line	Wavenumber cm ⁻¹	E_J (K)	Band
C ₂ H ₂	R(5)	743.264	35.30	ν_5
C ₂ H ₂	R(6)	745.613	49.42	ν_5
C ₂ H ₂	R(12)	759.695	183.52	ν_5
C ₂ H ₂	R(13)	762.039	214.10	ν_5
C ₂ H ₂	R(17)	771.405	359.90	ν_5
C ₂ H ₂	R(18)	773.744	402.22	ν_5
C ₂ H ₂	R(20)	778.417	493.90	ν_5
C ₂ H ₂	R(21)	780.752	543.26	ν_5
HCN	R(10)	744.458	162.57	ν_2
HCN	R(16)	762.121	401.86	ν_2
HCN	R(22)	779.725	747.24	ν_2
HCN	R(23)	782.652	815.09	ν_2

Note. — Only lines that were individually detected at the 3- σ level are included in this list.

data and the model.

The model assumed that each molecule is found in one or more absorbing ‘components’. Each component is described by its Doppler shift, V_{LSR} , its Gaussian line width ($1/e$ half width), b , the molecule’s column density, N , the rotational temperature of the gas, T , and the covering factor, C , (the fraction of the background continuum source covered by the component). The fitted column density is the average over the partially covered source, so the column density in the covered portion would be N/C . A covering factor of, e.g., 10% means that lines saturate at 90% of the continuum flux. This could result from a partially covered source, from veiling (continuum emission from foreground or surrounding material), or from re-emission in the lines by the absorbing molecules. Components were assumed to only overlap by the product of the covering factors (see Fig. 3.2). This approach was chosen because it gave a better fit to the data than adding the optical depths first and assuming the same covering factor. It assumes that different components absorb along different lines of sight to a partially covered continuum source. The following equation was used to calculate the observed transmission:

$$I_{obs} = I_0(1 - C_1(1 - e^{-\tau_1(\nu)}))(1 - C_2(1 - e^{-\tau_2(\nu)})). \quad (3.1)$$

where C_1 and C_2 are the covering factors for the two components. This model is the same as the one used to model NGC 7538 IRS 1 (see Chapter 4).

A constant frequency resolution (as opposed to a constant Doppler res-

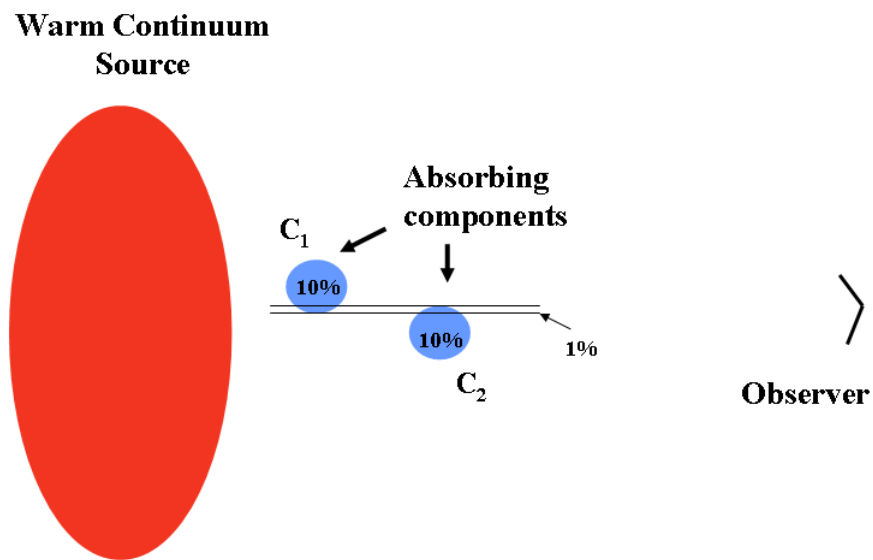


Figure 3.2 This figure shows two absorbing components between the continuum source and the observer. Each component covers 10% of the continuum source. The overlap of the two absorbing regions is given by the product of their covering factor. In this case, only 1% of the continuum source is covered by both components.

olution) was used in each of the two fitted regions. That approximates the improving resolving power toward shorter wavelengths in the 10.7-13.7 μm region. In addition to these parameters, the continuum, slope, and curvature of each echelon order were varied, to allow correction of the baseline fitting done during data reduction. The continuum fitting required 87 free, but rather easily determined, parameters. There were fewer parameters needed to determine the physical parameters such as temperature, column density, line width and covering factor: 28 parameters.

For C_2H_2 , lines of several bands were observed. In addition to lines of the R branch of the ν_5 fundamental, lines of several $\nu_4 + \nu_5 - \nu_5$ and $2\nu_5 - \nu_5$ bands (involving absorption from the excited ν_4 and ν_5 vibration states) were observed. The vibrational temperatures of the ν_4 and ν_5 states were included as free parameters in the fit. R-branch lines of the ν_5 band of $^{13}\text{CCH}_2$ were also observed. The HCN lines observed were from the ν_2 bending mode. We included H^{13}CN lines in the fit, with an assumed $^{12}\text{C}/^{13}\text{C}$ ratio of 60. Although no H^{13}CN lines were obvious in the spectra, their inclusion constrained the best-fitting N_{HCN} noticeably (although not outside of its very large uncertainty).

Although it might not be apparent from the spectra, given the shallowness of the lines, many of the detected lines are at least moderately saturated, and some are very saturated. The lines only appear weak because of the small covering factors (or emission filling in the absorption lines) and to a lesser extent the small line widths. This conclusion is very robust; the relative depths

of lines of different opacity requires substantial saturation. This is most apparent in the near equality of the depths of the ortho and para lines in C_2H_2 instead of the expected 3:1 ortho:para ratio (see Figure 3.1). By including isotopomers and intrinsically weak lines, a wide enough range of line optical depths was observed to allow meaningful constraints to be placed on the molecular abundances in spite of the saturation.

The derived component parameters are given in Table 3.2. Uncertainties for the parameters, given in parentheses, are three times the square roots of the diagonal elements of the error matrix, which are uncertainties allowing all other parameters to vary. The noise in the fitted spectra is assumed to be purely photon statistical noise. With this noise estimate, the reduced $\chi^2 \approx 1.2$, indicating that non-statistical noise sources contribute moderately, or perhaps that a different model for the line profiles is justified. Including non-statistical noise, the uncertainties given might reasonably be taken to be 95% confidence intervals. The larger fractional errors are asymmetric, and would be more symmetric in the log of the parameters. Both molecules are detected with very high confidence.

3.3.1 Properties of the Absorbing Gas

With the high spectral resolution of TEXES, we can resolve two components. We find asymmetric, double-peaked profiles especially evident in less optically thick lines (see C_2H_2 R(6) line in Figure 3.1). For both molecules, we found two components with Doppler shifts of $V_{\text{LSR}} \sim -7.5 \text{ km s}^{-1}$ and

Table 3.2. Results from the model

Molecule	V_{LSR} km s ⁻¹	b (km s ⁻¹)	T_{ex} (K)	$N(X)$ 10 ¹⁶ (cm ⁻²)	C %
C ₂ H ₂	-7.9(0.4)	2.4(0.4)	303(51)	1.9(1.0)	5(1.8)
C ₂ H ₂	-14.2(0.6)	5.7(0.6)	311(27)	1.4(0.3)	13(1.9)
HCN	-7.2(0.6)	3.5(0.3)	269(45)	12(8)	5(1.5)
HCN	-14.9(0.6)	5.4(0.7)	249(30)	13(6)	10(1.2)

Note. — The column densities listed are averages over the lines of sight to the continuum emitting material, or column densities in the absorbing gas multiplied by the covering factor, $\langle NC \rangle$.

-14.5 km s⁻¹, with widths of $b \sim 2.4 - 5.7$ km s⁻¹(see Table 3.2).

Most of the component temperatures are in the range 250-310 K and covering factors are typically 5–13%. Carr et al. (1995) adopted the temperatures derived from CO observations (Mitchell et al. 1989). From CO observations, two temperatures were derived for absorption centered around -8 and -11 km s⁻¹: $T \sim 1000$ K and 38 K. These temperatures were derived with the assumption that the absorbing material covers the continuum source completely (i.e., the covering factor is 100%). When we try the same temperatures from Mitchell et al. (1989), we do not get as good a fit as with the lower temperatures and low covering factors. Figure 3.3 shows the synthetic spectrum resulting from the temperatures and column densities used by Carr et al. (1995). The synthetic lines are flat-bottomed especially for the

lower J transitions. Also, the $^{13}\text{CCH}_2$ line at 744.3 cm^{-1} is not present in the observations.

Lahuis & van Dishoeck (2000) found lower temperatures for both C_2H_2 and HCN than what Carr et al. used. Lahuis & van Dishoeck find that they are not sensitive to the cold component seen by Mitchell et al. ($T \sim 38\text{ K}$). While our temperatures are lower than those found by Mitchell et al. and Lahuis & van Dishoeck, they are similar to the temperature derived from the H_2O observations (Helmich et al. 1996). We do not see the cold component at $T = 38\text{ K}$. This point will be discussed further in Chapter 3.4.2.

The derived column densities for C_2H_2 and HCN are higher than the column densities derived by Carr et al. and Lahuis & van Dishoeck. Since we find that the lines are very saturated but shallow, we use a covering factor to explain the observed depths of the lines. In order for the lines to be saturated the column density has to be higher than what is derived in the previous studies. Note that our quoted column densities are averages over the lines of sight to the continuum emitting material, or column densities in the absorbing gas multiplied by the covering factors. Since our fitted covering factors may instead be a way of representing the effect of emission in the lines filling in the absorption, the actual column densities of our molecules could be as much as an order of magnitude larger than our quoted numbers.

We calculate the abundances of C_2H_2 and HCN relative to both CO and H_2 (see Table 3.3). Because H_2 is hard to measure, a comparison with CO is a more direct way of comparing observations to chemical models (see

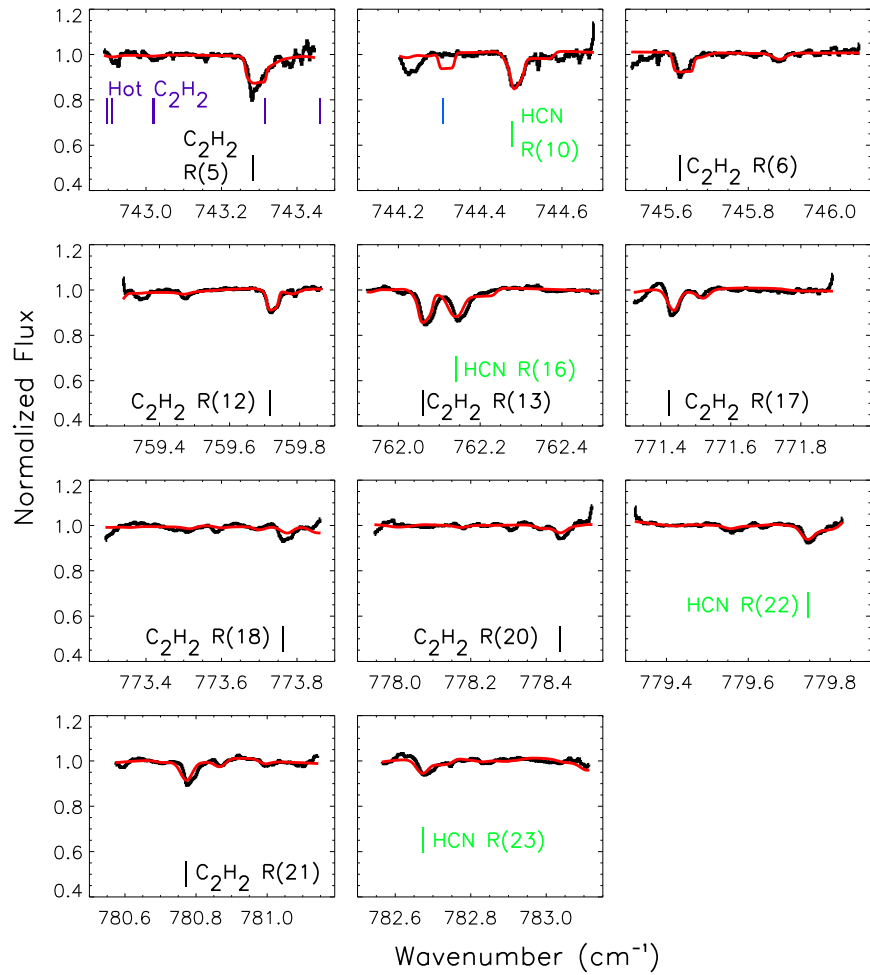


Figure 3.3 Same as Figure 3.1 except the fit in red here represents the model using the temperatures and column densities found by Carr et al. (1995). In the second panel a line of $^{13}\text{CCH}_2$ is predicted by the model but is not observed.

Chapter 3.4.2). However, CO has a large covering factor and possibly samples different lines of sight.

Despite differences in the derived temperatures for the components centered around -11 km s^{-1} , we take the combined column density of CO found in both cold and hot components to compare with the total columns we observe. Using $^{12}\text{C}/^{13}\text{C} = 60$ derived from the C_2H_2 isotopomers, the ^{12}CO column density is $1.3 \times 10^{19} \text{ cm}^{-2}$. This gives abundance ratios of 2.5×10^{-3} and 1.9×10^{-2} for $\text{C}_2\text{H}_2/\text{CO}$ and HCN/CO , respectively. If we instead look at the abundance compared to H_2 , we calculate the following abundances: $X(\text{C}_2\text{H}_2) = 2.4 \times 10^{-7}$ and $X(\text{HCN}) = 1.8 \times 10^{-6}$. The H_2 column is derived from the optical depth of the silicate feature observed by Willner et al. (1982), $\tau_{9.7} = 4.14$. First we use the extinction to silicate relation, $A_V/\tau_{9.7} = 18.5$ (Draine 2003). Then we relate the extinction to the column density of hydrogen using $N_{\text{H}} \approx 1.87 \times 10^{21} A_V \text{ cm}^{-2}$ for $R_V = 3.1$ (Draine 2003). The abundance of CO with respect to H_2 is then $\sim 10^{-4}$. The abundance of HCN is enhanced when compared to the submillimeter observations of the material in the envelope (van der Tak et al. 1999). From observations of vibrationally excited HCN ($\nu_2 = 1$), Boonman et al. (2001) also find that the abundance of HCN is $\sim 10^{-6}$ in the inner warm gas.

AFGL 2591 is just one example of a ‘warm’ core, a source which has warm gas but does not have enhanced abundances of complex molecules like hot cores (van Dishoeck & van der Tak 2000). NGC 7538 IRS 1, which is another massive protostar and is studied in Chapter 4, does not have high

Table 3.3. Abundances with respect to CO and H₂

Molecule	$N(X)/N(\text{CO})^*$ 10^{-3}	$N(X)/N(\text{H}_2)^*$ 10^{-7}
C ₂ H ₂	2.5	2.4
HCN	19	18

Note. — *N(CO) = 1.3×10^{19} cm⁻² and
N(H₂) = 1.4×10^{23} cm⁻².

abundances of complex molecules from radio observations. NGC 7538 IRS 1 also has enhanced abundances of C₂H₂ and HCN (see Lahuis & van Dishoeck 2000, and Chapter 4). In addition, IRS 1 has enhanced abundances of CH₄, CH₃, and NH₃. As mentioned in Chapter 3.2, HNCO is also detected toward IRS 1. While AFGL 2591 has abundant C₂H₂ and HCN, NGC 7538 IRS 1 appears to have a richer mid-infrared spectrum. It is possible that the broader line widths observed toward AFGL 2591 make the detection of weak lines, such as those of HNCO, CH₃, and NH₃, very difficult. However, it is more likely that the molecules are less abundant in AFGL 2591 than in NGC 7538 IRS 1.

3.4 Models

3.4.1 Physical Models

Torrelles et al. (1989) concluded that there is a cavity as traced by NH₃

(1,1) emission and by near-infrared continuum (Forrest & Shure 1986). The continuum and molecular line emission show material being pushed out by the outflow. The cavity is aligned with the blue-shifted lobe of the outflow seen in CO. Preibisch et al. (2003) showed that loops of material enclosing the cavity are very clumpy. The extent of the loops ranges between $5 - 15''$.

We observe two distinct velocity components at -7.5 km s^{-1} and -14.5 km s^{-1} . The -7.5 km s^{-1} component is slightly blue-shifted from the ambient cloud velocity while the other component is more blue-shifted from the ambient velocity. Since there is evidence of clumpy material having been pushed out, it is likely that clumpy material near the protostar is also being pushed out. Preibisch et al. (2003) suggest that the loops may be due to episodic ejection of material similar to a highly variable FU Orionis star. Then, the two velocity components seen here could trace clumps which have been accelerated outward at different times. Since these clumps are still close to the protostar, they can be heated such that grain mantles evaporate. Thus, we observe enhanced abundances of C_2H_2 and HCN. However, these clumps do not cover the entire continuum source, which arises from the hot dust close to the star and from the dusty envelope material.

This source has been modeled extensively. Physical models of the envelope are discussed by van der Tak et al. (1999). They ascribe the high near- and mid-infrared continuum as due to deviation from spherical symmetry, lowering the optical depth to the hot inner 10-20 AU where the continuum originates. This lower optical depth can result from clearing due to the CO outflow. From

the dust continuum, they find a power-law density structure, $n = n_0 r^{-\alpha}$ with a best-fit of $\alpha = 1.5$. For such a density structure, they also derive the dust temperature structure given various dust opacity constants. If we assume that the temperature of the dust also describes the temperature of the gas, then we find that the region probed by the infrared absorption of C_2H_2 and HCN is a region between 200–500 AU away from the central object.

3.4.2 Chemical Models

Observed enhancements of molecules such as C_2H_2 and HCN are thought to result from warm gas-phase chemistry following the sublimation of grain mantles once temperatures are ≥ 100 K. If this is true, then at low temperatures, the expected abundances should not be enhanced. Since absorption from CO gas traces a cold component at $T = 38$ K which is not seen in the C_2H_2 and HCN absorption, this suggests that sublimation of icy mantles does play a role in the enhancement of these molecules in the cold gas. Since CO desorbs at very low temperatures ($T \sim 20$ K), it is a good molecule to trace the cold gas. As far as C_2H_2 and HCN are concerned, they are either still trapped on the grain surfaces or else they will form from the newly sublimated species through gas-phase reactions.

Despite the lower abundance of complex molecules (van Dishoeck & van der Tak 2000), the abundances for molecules such as C_2H_2 and HCN are definitely enhanced compared to the envelope abundances by at least a factor of 100 (Carr et al. 1995; van der Tak et al. 1999; Lahuis & van Dishoeck 2000).

The covering factor used in our models can be interpreted as small clumps of absorbing gas not covering the continuum source as illustrated in Figure 3.2. If this is true, then single-dish radio observations would be too beam diluted to detect large abundances from the small hot region (Boonman et al. 2001).

We compare our observations of AFGL 2591 to various hot core models (see Table 3.4). Rodgers & Charnley (2001) present models for two different temperatures, 100 and 300 K. At each temperature, they explore the effect of the sublimation of NH_3 from grain mantles. Since the temperature derived from our observations is around 300 K, we will only consider models at 300 K. At this temperature, the effect of NH_3 sublimation does not affect C_2H_2 and HCN very much. The predicted abundance (with respect to H_2) for C_2H_2 peaks at $\sim 10^{-7}$ at $\sim 10^5$ yrs. At a similar age, the HCN abundance reaches 10^{-6} . The models come closest to fitting our observations at $\sim 10^5$ yrs.

Doty et al. (2002) present a chemical model for AFGL 2591. This model attempts to fit the abundances found by Carr et al. (1995), Lahuis & van Dishoeck (2000), and Boonman et al. (2001) assuming the corresponding temperatures. The C_2H_2 observations can be reproduced by the models at times $> 10^4$ yrs; however, the HCN abundance predicted was lower than observed. While Doty et al. (2002) mention that an age of 10^5 yrs is consistent with the observations, using the time constraints of both infrared and radio molecular observations, they found that there is an age preference of 3×10^4 yrs. Subsequently, Stauber et al. (2004, 2005) used the physical model by Doty et al. and explored the effects of UV and X-ray irradiation in the inner

Table 3.4. $N(X)/N(H_2)$ From Chemical Models

Molecule	Observed (10^{-7})	Model 1 ^a (10^{-7})	Model 2 ^b (10^{-7})	Model 3 ^c (10^{-7})
C ₂ H ₂	2.4	~1	~1	~1
HCN	18	~10	~0.1	~10

References. — ^a Rodgers & Charnley 2001 with $T = 300\text{K}$

^b Doty et al. 2002

^c Stäuber et al. 2004, 2005

regions. In both cases, the HCN abundance is $\sim 10^{-6}$ at radii between 100-300 AU from the central object. As mentioned in Chapter 3.4.1, at these radii the temperature is ~ 300 K, which agrees with our derived temperatures.

3.5 Conclusions

Our results are summarized below:

1. Two velocity components separated by ~ -7 km s⁻¹ are resolved in the profiles of C₂H₂ and HCN lines observed at high spectral resolution ($R \sim 75000$ or $\delta v \sim 4$ km s⁻¹). The central velocities for the two components are at -7.5 and -14.5 km s⁻¹, with line widths of ~ 3 and 5.5 km s⁻¹, respectively.

2. From the high spectral resolution observations, lower kinetic temperatures ($T = 250 - 300$ K) are derived for C₂H₂ and HCN for one of the

components than had been previously observed ($T \sim 1000$ K) (Mitchell et al. 1989; Boonman et al. 2001). This means that the chemically enhanced material does not need to be as close to the central object as previously thought. In fact, from both chemical and physical arguments, absorbing gas seems to trace a region within 100-500 AU from the central source.

3. The two observed velocity components appear to be tracing clumps of material being pushed out from the central source. The interaction with the outflow may cause the broader lines observed toward AFGL 2591 compared to the narrow lines observed in NGC 7538 IRS 1. Also, the small covering factor found for the two velocity components can be explained by clumpy material that does not fully cover the continuum source.

4. From chemical model predictions of C_2H_2 and HCN abundances, the age of the source is consistent with being $\sim 10^5$ yrs. However, from evidence of other species, Doty et al. (2002) find that there is a preference for an age closer to 3×10^4 yrs. They do not rule out an age of 10^5 yrs.

AFGL 2591 provides a luminous yet chemically simple laboratory in which to begin to study chemistry toward protostars. The AFGL 2591 region has a lot of structure with other faint mid-infrared sources nearby (see Marengo et al. 2000). Within $5''$ to the southwest of the central protostar, there is a 15 Jy source. A spatially-resolved, spectral map of the region may give us a better idea of the physical and chemical evolution of the region. High sensitivity is needed in order to detect the 15 Jy (at $12 \mu\text{m}$) mid-infrared source. With TEXES on Gemini, we can achieve the sensitivity and resolution need to do

spectral mapping of the AFGL 2591 region in C_2H_2 and HCN lines.

Chapter 4

High Resolution Mid-Infrared Spectroscopy of NGC 7538 IRS 1: A UV-Illuminated Protostellar Disk?

4.1 Introduction

The NGC 7538 (S158) molecular cloud, located in the Perseus arm at a distance of 2.8 kpc (Ungerechts et al. 2000), contains many protostellar objects, making it a good candidate to study different stages of star formation. Furthermore, there seems to be a progression in evolution from northwest (the visible H II region, NGC 7538, and IRS 2, an only moderately obscured compact HII region) to southeast (IRS 9, a deeply embedded core) (Elmegreen & Lada 1977; Campbell & Thompson 1984). The near- and mid-infrared sources IRS 1, 2, and 3 all lie near the northwest end of the star-forming region. Of these, IRS 1 is the brightest mid-infrared and radio continuum source (Martin 1973; Wynn-Williams et al. 1974; Willner 1976). Its exciting star has a luminosity of $L > 8 \times 10^4 L_{\odot}$, a spectral type earlier than O7.5, and an ionizing photon flux of $\phi > 10^{48} \text{s}^{-1}$ (Werner et al. 1979; Lugo et al. 2004).

IRS 1 is embedded in a dense molecular cloud. Millimeter continuum emission is seen from the surrounding dust (Scoville et al. 1986), and thermal and maser emission is seen from numerous molecules. Pratap et al. (1989)

mapped the HCO^+ and HCN emission from within $\sim 1'$ of IRS 1 with $3''$ resolution. They found evidence for a shell-like structure on scales of $10\text{--}20''$ around IRS 1. Wilson et al. (1983) observed NH_3 absorption toward IRS 1, and Henkel, Wilson, & Johnston (1984) mapped the absorption with the VLA. The absorption traces warm gas with a high column density of NH_3 and is centered near -60 km s^{-1} . The emission, on the other hand, is centered near -56.5 km s^{-1} . More recently, Zheng et al. (2001) mapped NH_3 emission from a more extended region in NGC 7538. This material probably probes the outer envelope as indicated by the colder temperature and the smaller column density.

Using both single-dish and interferometer observations of various molecular tracers, van der Tak et al. (2000) studied the density and temperature structure of both the cold outer envelope and the warm inner material ($240\text{--}72000 \text{ AU}$). The inner warm region is characterized by temperatures of a few hundred K.

Outflows are often present toward protostars, and NGC 7538 IRS 1 is no exception. Campbell (1984b) observed IRS 1 with the VLA at 5 and 15 GHz. She found a pair of very compact lobes of continuum radiation, separated in declination by $0.2''$, with emission extending out to $\pm 2''$. Her preferred model involves a bipolar ionized outflow from a late O star, collimated by a core of dense gas extending from $<65 \text{ AU}$ to $>25,000 \text{ AU}$. Further evidence of outflows was found when Gaume et al. (1995) observed IRS 1 with the VLA in the $\text{H66}\alpha$ line and the 22 GHz continuum. Their continuum image is similar to that of

Campbell, but shows additional structure. They found broad recombination line emission, full width at half-maximum (FWHM) $\sim 180 \text{ km s}^{-1}$, in the two lobes, with a minimum line-to-continuum ratio, which they attribute to high electron density, between the lobes. They propose a model involving a high velocity stellar wind interacting with photo-evaporating clumps of neutral gas. More recently, Lugo et al. (2004) have modeled the radio continuum observations of IRS 1 as due to a wind produced by photo-evaporation of a circumstellar disk with a radius of 500 AU exposed to UV radiation from the central O star.

Maser line emission is seen from H_2O (Kameya et al. 1990), OH (Dickel et al. 1982), H_2CO (Hoffman et al. 2003), CH_3OH (Menten et al. 1986), and NH_3 (Madden et al. 1986). Minier, Booth, & Conway (1998) used VLBI observations of the methanol masers to infer the presence of a nearly edge-on rotating disk around IRS 1. The central velocity of the masers along the line of sight to IRS 1 is -56.2 km s^{-1} . The disk masers lie along a line centered near the gap between the lobes of the free-free continuum radiation, although they are aligned along a position angle $\sim 30^\circ$ from the symmetry plane. Pestalozzi et al. (2004) made a detailed model of maser emission from a disk around IRS 1, supporting the suggestion of Minier et al. They concluded that the maser emission comes from disk radii of $\sim 290 - 750 \text{ AU}$. However, more recently, De Buizer & Minier (2005) show that the CH_3OH masers may trace clumps in the outflow instead. Also, De Buizer & Minier identify a disk-like structure perpendicular to the outflow direction in mid-infrared continuum.

The extent of the infrared emission is ~ 450 AU.

Infrared absorption by dust grains and their icy mantles has also been observed toward IRS 1. Willner (1976) and Willner et al. (1982) observed $9.7 \mu\text{m}$ silicate absorption and absorption by various ices, including H_2O . They considered two models for the mid-infrared continuum spectrum: emission by optically thin silicate grains, in which case they required $\tau_{9.7} = 0.15$ and $T_{dust} = 370$ K for the emitting grains, and $\tau_{9.7} = 6.4$ for the overlying extinction, or emission by an optically thick blackbody source, with $T = 330$ K, and extinction with $\tau_{9.7} = 4.2$. The two extinction values correspond to $A_V \approx 90$ and 60 , and $N_{\text{H}_2} \approx 9 \times 10^{22}$ and $6 \times 10^{22} \text{ cm}^{-2}$, respectively. The first model, with optically thin emission, gave a better fit to the silicate spectrum, and the larger extinction is most often referenced. The ice bands toward IRS 1 are relatively weak, especially in comparison with NGC 7538 IRS 9, which must lie in a colder region of the NGC 7538 cloud. Gibb et al. (2004) observed the complete $2.5\text{-}20 \mu\text{m}$ region with the Short-Wavelength Spectrometer (SWS) on the *Infrared Space Observatory, ISO*. H_2O , CO , and CO_2 ices are clearly present, as well as other less securely identified features. Toward NGC 7538 IRS 9, $\sim 1'$ southeast of IRS 1, a much richer ice spectrum is seen, with CH_3OH , XCN (probably OCN^-), and CH_4 also confidently identified, and OCS , H_2CO , HCOOH , and NH_3 likely present. Gas-phase CH_4 is also detected toward IRS 9 (Lacy et al. 1991; Boogert et al. 2004a) but not IRS 1.

Gas-phase absorption in the infrared has been observed toward IRS 1

by several groups. Mitchell et al. (1990) observed absorption by ^{12}CO and ^{13}CO in their $5\ \mu\text{m}\ v = 1 - 0$ bands. They did not spectrally resolve the lines, and they used a curve of growth analysis assuming pure absorption by Gaussian lines with FWHM of $8\ \text{km s}^{-1}$ to derive the gas temperature and column density from the less-saturated ^{13}CO lines. They found two absorbing components: cold gas at 25 K, and warm gas at 176 K. A gas density of $n_H > 10^6\ \text{cm}^{-3}$ was required to maintain the population of the high- J levels in the warm gas. Using the *ISO-SWS*, Lahuis & van Dishoeck (2000) detected warmer gas than the CO observed by Mitchell et al.. They observed the ν_5 band of C_2H_2 at $13.7\ \mu\text{m}$ and the ν_2 band of HCN at $14.0\ \mu\text{m}$. With the SWS resolution of ~ 1800 , they were not able to resolve individual lines, and were most sensitive to the blended lines of the Q branches, but they were able to derive temperatures and column densities from the shapes of the Q branches and the depths of the $v = 1 - 0$ fundamental and $v = 2 - 1$ hot band Q branches. They derived $T = 800\ \text{K}$ and $N = 0.8 \times 10^{16}\ \text{cm}^{-2}$ for C_2H_2 , and $T = 600\ \text{K}$ and $N = 1.0 \times 10^{16}\ \text{cm}^{-2}$ for HCN. Boonman et al. (2003) derived $T = 500\ \text{K}$ for C_2H_2 from an updated reduction of the spectra. Boonman et al. (2003) and Boonman & van Dishoeck (2003) studied gas absorption from CO_2 and H_2O using *ISO* data. They found enhanced abundances toward the inner warm material compared to the cold envelope.

Models of hot core chemistry (e.g., Doty et al. 2002; Nomura & Millar 2004) attempt to reproduce the warm gas-phase chemistry following the evaporation of icy grain mantles. Enhanced abundances of molecules such

as C_2H_2 and CH_4 are predicted by these models. Stäuber et al. (2004) and Stäuber et al. (2005) explore the effects of UV and X-rays on the chemistry around massive protostars. Models of UV illuminated disks also predict high abundances of such molecules (Nguyen et al. 2002).

The wealth of observational data available suggest the following physical scenario for NGC 7538 IRS 1. The massive young star is surrounded by a massive cold envelope on scales ~ 72000 AU (van der Tak et al. 2000). At scales below 1000 AU, the temperature increases to ≥ 100 K. Inside this radius, there is evidence for a disk (De Buizer & Minier 2005) and small scale clumpy outflows (Gaume et al. 1995), both of which can be affected by the UV and X-ray radiation from the protostar.

In this chapter, we present high resolution mid-infrared observations of NGC 7538 IRS 1 showing a rich absorption spectrum containing lines from *seven* molecules: C_2H_2 , HCN, CH_4 , CH_3 , NH_3 , HNC, and CS. Mid-infrared absorption is much more sensitive to the inner warm gas than radio observations. Previous infrared studies suffered from limited spectral resolution. Chapter 4.2 describes the observations. We then present the model used to derive the column densities and temperatures for the various species in Chapter 4.3 and describe the results for each of the molecules in subsections. Subsequently, in Chapter 4.4, we discuss the possible scenario in which we are probing chemistry in a circumstellar disk. In Chapter 4.5, we provide some concluding remarks.

4.2 Observations

4.2.1 Observations and Data Reduction

The observations were made with TEXES, the Texas Echelon Cross Echelle Spectrograph, on the NASA Infrared Telescope Facility (IRTF) in 2001 June and November, 2002 September and December, and 2005 December. Much of the data were taken in less than ideal weather, but the observing conditions did not seriously affect the spectra except for increased noise, especially on atmospheric lines.

TEXES is a high-resolution cross-dispersed spectrograph operating at mid-infrared wavelengths between 5 and 25 μm (Lacy et al. 2002). It achieves a spectral resolution of $R = 75,000\text{-}100,000$ ($\Delta v = 3 - 4 \text{ km s}^{-1}$) shortward of 14 μm with a slit width of $\sim 1.5''$. (Of the observations presented here, only the spectra near 11 μm , which used a $1''$ slit, achieved the higher resolution.) At each spectral setting, 5-10 orders of the high resolution echelon grating are recorded, giving a spectral coverage of $\sim 0.5\%$. At wavelengths shortward of 11 μm full orders are observed, giving continuous spectral coverage, but longward of 11 μm the order width exceeds the array width, leaving gaps in the observed spectra. The spatial resolution along the slit is $\sim 1''$, slightly larger than the diffraction limit of the IRTF. The spectral and spatial sampling by the 256×256 pixel Si:As detector array are 1.0 km s^{-1} and $0.35''$, respectively.

Observations of NGC 7538 IRS 1 were interspersed with observations of a bright asteroid (usually Ceres but also used Hygeia), which served as a comparison source for removal of telluric absorption features. The telescope

was nodded by 3-5", moving the source along the spectrograph entrance slit to allow subtraction of background emission. At the beginning of each set of nodded observations an ambient temperature blackbody was observed for flat-fielding.

Data reduction followed the standard TEXES procedure (Lacy et al. 2002) of first subtracting the two nod position spectra, flat-fielding with the blackbody-sky difference spectrum, and interpolating over spikes and bad pixels. Optimally-weighted point-source spectra were then extracted from the echelograms. The spectra were linearized in $\ln(\nu)$ based on the known optical distortions, and absolute wavenumber calibration was obtained from telluric emission features. The resulting wavenumber scale is correct to within 1 km s^{-1} . The same procedure was used for the asteroid spectra, and then the IRS 1 spectra were divided by the asteroid spectra with correction for differences in airmass. With this procedure, telluric absorption lines as deep as 90% can be removed, although of course the noise increases on lines. However, broad response variations often remained, which were removed by fitting the continuum in each echelon order to a quartic polynomial and dividing. This procedure also sets the continuum in each order to one.

4.2.2 New Infrared Detections

Ten spectral settings were observed in the $728\text{--}820 \text{ cm}^{-1}$ ($13.7\text{--}12.2 \mu\text{m}$) region, two in the $860\text{--}930 \text{ cm}^{-1}$ ($11.5\text{--}10.7 \mu\text{m}$) region (see Figure 4.1), and three in the $1240\text{--}1312 \text{ cm}^{-1}$ ($8.0\text{--}7.6 \mu\text{m}$) region (see Figure 4.2). A total of

110 echelon orders, or $\sim 70 \text{ cm}^{-1}$, were observed. The original observations were meant to study the line profiles of C_2H_2 and HCN , which had previously been detected. Many C_2H_2 hot band lines were detected in our spectra including lines from the $\nu_4 + \nu_5 - \nu_4$ and the $2\nu_5$ bands. After the hot bands were identified, unidentified lines still remained, some of which were double dipped. The double lines turned out to be CH_3 lines which are split due to spin-rotation interactions (see Appendix 1). This is the first detection of CH_3 toward dense gas. In efforts to detect ethane, C_2H_6 , between $810\text{--}820 \text{ cm}^{-1}$, many lines were detected, though none corresponded to C_2H_6 . Some were quickly attributed to NH_3 , but many lines remained unidentified for some time (see Figures 4.3 and 4.4). Based on their separation we were able to narrow the possible carriers and finally identified the lines as HNCO . Interstellar HNCO is a well known hot core molecule at radio wavelengths (Zinchenko et al. 2000), but it had never been seen at infrared wavelengths. Its identification was possible only after its spectroscopy was understood (see Appendix 1). In total, five molecules were observed in the $728\text{--}820 \text{ cm}^{-1}$ region: C_2H_2 (including $^{13}\text{CCH}_2$), HCN , HNCO , CH_3 , and NH_3 . At higher frequencies, CH_4 , C_2H_2 and CS were observed in the $1240\text{--}1320 \text{ cm}^{-1}$ region. CH_4 observations from the ground are possible for this source because of the large Doppler shift with respect to the telluric lines.

Table 4.1 gives a summary of the detected lines. At least 5 lines were observed for each molecule, with some molecules like C_2H_2 (including isotopic lines and hot bands), and NH_3 having more than 40 lines detected. However,

the number of HNC₂ lines dominates over lines from the other molecules with over 100 lines detected. Table 4.2 lists all the individual lines detected in our spectra. A selection of spectra including all observed molecules are shown in Figures 4.1 and 4.2, along with fits described in Chapter 4.3. For most molecules the line strengths were taken from the GEISA03 database (<http://ara.lmd.polytechnique.fr>). CH₃ and HNC₂ band strengths were calculated by van Hemert (priv. comm.). The CS band strength was taken from Botschwina & Sebald (1985).

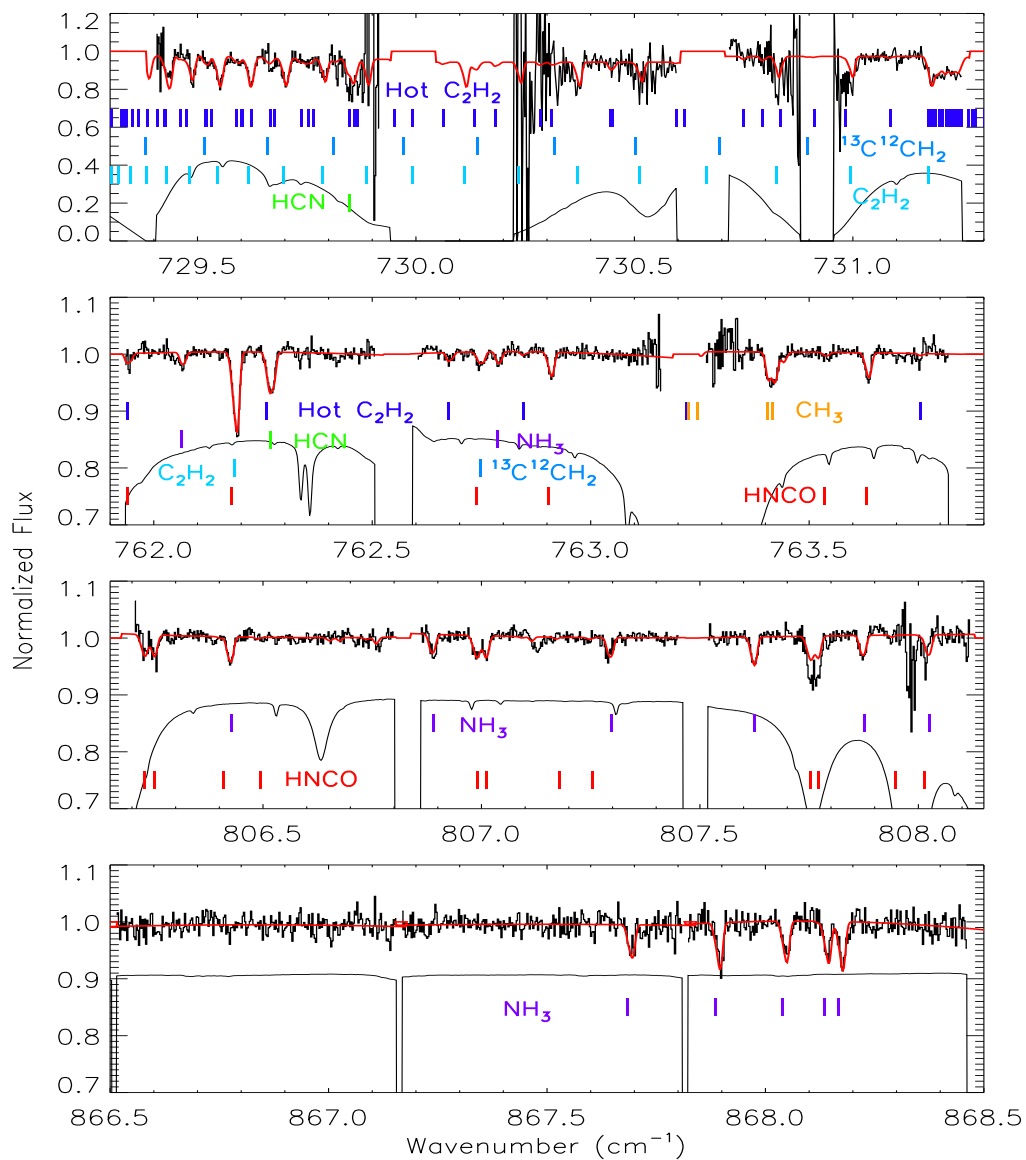


Figure 4.1 Selected orders (thick black) between 729 and 870 cm^{-1} are shown with the best fit (red). Position of lines considered in the fit are given: C_2H_2 (light blue), $^{13}\text{C}^{12}\text{CH}_2$ (blue), hot bands of C_2H_2 (dark blue), HCN (green), CH_3 (orange), HNCO (red), and NH_3 (purple). The thin black line indicates the atmospheric transmission. The top panel has a larger scale for the normalized flux (y-axis) to show the lower atmospheric transmission. Note that there are gaps between orders.

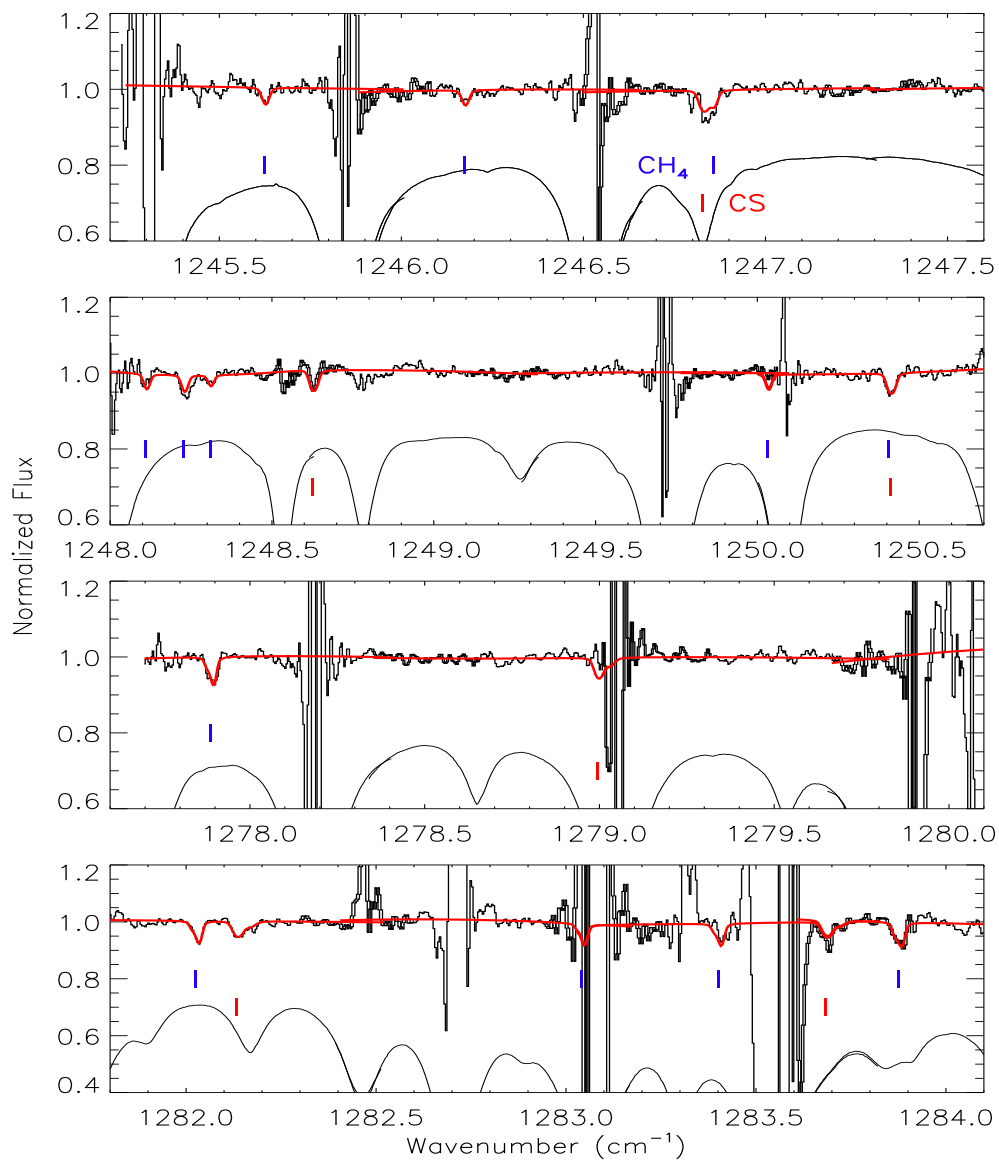


Figure 4.2 Selected orders (thick black) between 1245 and 1285 cm^{-1} are shown with the best fit (red). Position of lines considered in the fit are given: CH_4 (blue) and CS (red). The thin black line indicates the atmospheric transmission. In this region there are no gaps between orders. Instead the orders overlap where the black line is darker.

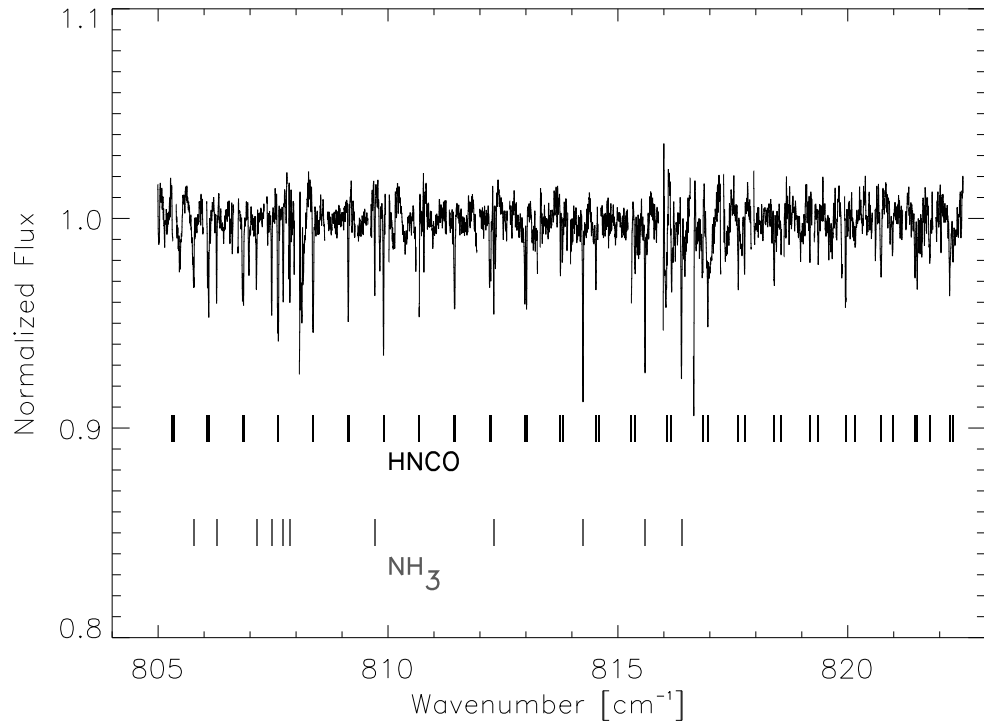


Figure 4.3 This figure shows a portion of spectrum containing some NH_3 lines as well as wealth of HNCO lines. These spectral settings led to the identification of HNCO. Figure 4.4 shows a small portion of this spectrum.

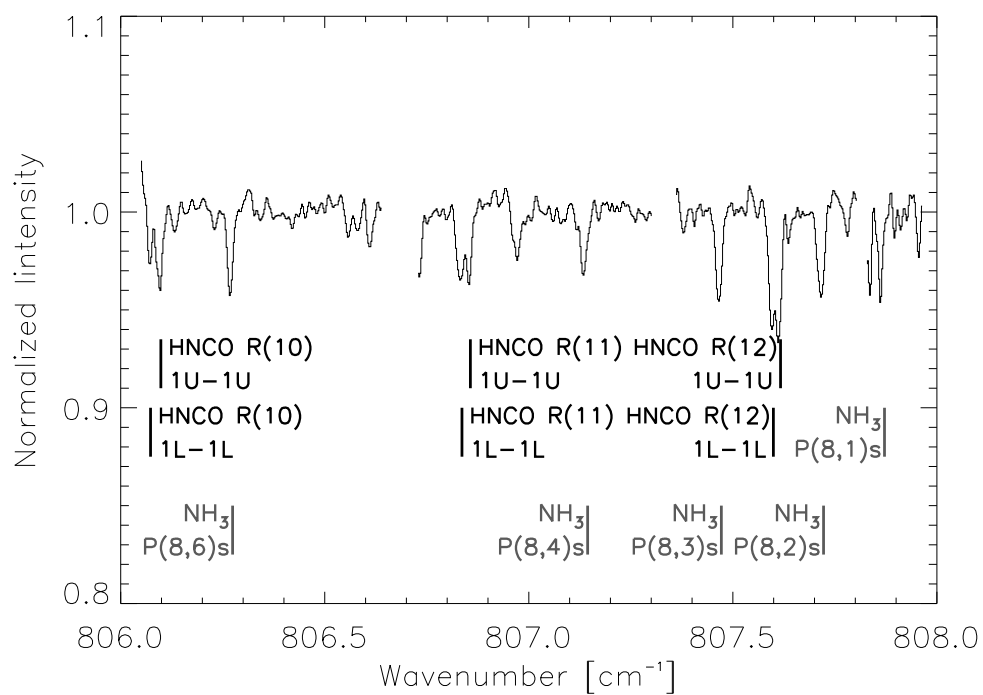


Figure 4.4 This figure shows the profiles of several HNC0 and NH₃ lines in the spectral region shown in Figure 4.3. The two HNC0 sub-bands shown are R-branch transitions where the $K = 1$ state is split into upper (U) and lower (L) levels. Because of the close separation the sub-bands, the lines can overlap for a range of J . See Appendix A for more details on transition rules for HNC0.

Table 4.1. Summary of Observed Lines

Molecule	Total Number of Detected Lines	Band
C ₂ H ₂	25	ν_5
C ₂ H ₂ ^a	2	$\nu_4 + \nu_5$
C ₂ H ₂ ^b	20	$\nu_4 + \nu_5 - \nu_4$
¹³ CCH ₂ ^c	7	ν_5
HCN	10	ν_2
NH ₃	64	ν_2
HNCO	125	ν_4
CH ₃	11	ν_2
CH ₄	12	ν_2/ν_4 dyad
CS	6	ν_2

Note. — *a.* These lines were observed at 8 μm .

b. Lines in Q-branch at 731 cm^{-1} . See top panel of Figure 4.1.

c. Only unblended lines are reported here.

Table 4.2. Observed Lines

Molecule	Line	Wavenumber cm^{-1}	E_J (K)	Band
C ₂ H ₂	Q(5)	729.289	35.30	ν_5
C ₂ H ₂	Q(6)	729.343	49.42	ν_5
C ₂ H ₂	Q(7)	729.406	65.89	ν_5
C ₂ H ₂	Q(8)	729.477	84.71	ν_5
C ₂ H ₂	Q(9)	729.558	105.89	ν_5
C ₂ H ₂	Q(10)	729.648	129.41	ν_5
C ₂ H ₂	Q(11)	729.747	155.29	ν_5
C ₂ H ₂	Q(14)	730.096	247.02	ν_5
C ₂ H ₂	Q(15)	730.230	282.30	ν_5
C ₂ H ₂	Q(16)	730.373	319.93	ν_5
C ₂ H ₂	Q(18)	730.686	402.22	ν_5
C ₂ H ₂	Q(19)	730.855	446.89	ν_5
C ₂ H ₂	Q(20)	731.034	493.90	ν_5
C ₂ H ₂	Q(26)	732.287	825.20	ν_5
C ₂ H ₂	Q(27)	732.526	888.62	ν_5
C ₂ H ₂	R(1)	733.859	2.35	ν_5

Table 4.2 (cont'd)

Molecule	Line	Wavenumber cm ⁻¹	E_J (K)	Band
C ₂ H ₂	R(5)	743.264	35.30	ν_5
C ₂ H ₂	R(6)	745.613	49.42	ν_5
C ₂ H ₂	R(8)	750.311	84.71	ν_5
C ₂ H ₂	R(12)	759.695	183.52	ν_5
C ₂ H ₂	R(13)	762.039	214.10	ν_5
C ₂ H ₂	R(15)	766.724	282.30	ν_5
C ₂ H ₂	R(16)	769.065	319.93	ν_5
C ₂ H ₂	R(20)	778.417	493.90	ν_5
C ₂ H ₂	R(21)	780.752	543.26	ν_5
C ₂ H ₂	P(9)	1307.165	105.89	$\nu_4 + \nu_5$
C ₂ H ₂	P(8)	1309.459	84.71	$\nu_4 + \nu_5$
¹³ CCH ₂	Q(10)	728.694	126.31	ν_5
¹³ CCH ₂	Q(11)	728.787	151.57	ν_5
¹³ CCH ₂	Q(12)	728.888	179.12	ν_5
¹³ CCH ₂	Q(13)	728.998	208.97	ν_5
¹³ CCH ₂	Q(14)	729.117	241.11	ν_5

Table 4.2 (cont'd)

Molecule	Line	Wavenumber cm ⁻¹	E_J (K)	Band
¹³ CCH ₂	Q(16)	729.378	312.27	ν_5
¹³ CCH ₂	Q(17)	729.522	351.28	ν_5
¹³ CCH ₂	Q(18)	729.673	392.59	ν_5
¹³ CCH ₂	Q(21)	730.178	530.26	ν_5
¹³ CCH ₂	Q(22)	730.363	580.72	ν_5
¹³ CCH ₂	Q(24)	730.758	688.52	ν_5
¹³ CCH ₂	Q(25)	730.967	745.84	ν_5
¹³ CCH ₂	R(2)	735.116	6.89	ν_5
¹³ CCH ₂	R(6)	744.291	48.23	ν_5
¹³ CCH ₂	R(8)	748.874	82.68	ν_5
¹³ CCH ₂	R(13)	760.317	208.97	ν_5
¹³ CCH ₂	R(14)	762.602	241.11	ν_5
¹³ CCH ₂	R(16)	767.171	312.27	ν_5
¹³ CCH ₂	R(17)	769.453	351.28	ν_5
C ₂ H ₂	Q(14)	731.034	859.54	$\nu_4 + \nu_5 - \nu_4$
C ₂ H ₂	Q(13)	731.035	826.50	$\nu_4 + \nu_5 - \nu_4$

Table 4.2 (cont'd)

Molecule	Line	Wavenumber cm ⁻¹	E_J (K)	Band
C ₂ H ₂	Q(15)	731.036	894.93	$\nu_4 + \nu_5 - \nu_4$
C ₂ H ₂	Q(12)	731.039	795.82	$\nu_4 + \nu_5 - \nu_4$
C ₂ H ₂	Q(21)	731.040	1154.34	$\nu_4 + \nu_5 - \nu_4$
C ₂ H ₂	Q(16)	731.041	932.68	$\nu_4 + \nu_5 - \nu_4$
C ₂ H ₂	Q(11)	731.044	767.50	$\nu_4 + \nu_5 - \nu_4$
C ₂ H ₂	Q(17)	731.050	972.79	$\nu_4 + \nu_5 - \nu_4$
C ₂ H ₂	Q(10)	731.050	741.53	$\nu_4 + \nu_5 - \nu_4$
C ₂ H ₂	Q(9)	731.058	717.93	$\nu_4 + \nu_5 - \nu_4$
C ₂ H ₂	Q(18)	731.064	1015.25	$\nu_4 + \nu_5 - \nu_4$
C ₂ H ₂	Q(8)	731.066	696.68	$\nu_4 + \nu_5 - \nu_4$
C ₂ H ₂	Q(7)	731.074	677.80	$\nu_4 + \nu_5 - \nu_4$
C ₂ H ₂	Q(6)	731.081	661.27	$\nu_4 + \nu_5 - \nu_4$
C ₂ H ₂	Q(19)	731.084	1060.06	$\nu_4 + \nu_5 - \nu_4$
C ₂ H ₂	Q(5)	731.089	647.11	$\nu_4 + \nu_5 - \nu_4$
C ₂ H ₂	Q(4)	731.095	635.30	$\nu_4 + \nu_5 - \nu_4$
C ₂ H ₂	Q(3)	731.100	625.86	$\nu_4 + \nu_5 - \nu_4$

Table 4.2 (cont'd)

Molecule	Line	Wavenumber cm ⁻¹	E_J (K)	Band
C ₂ H ₂	Q(2)	731.104	618.78	$\nu_4 + \nu_5 - \nu_4$
C ₂ H ₂	Q(20)	731.109	1107.23	$\nu_4 + \nu_5 - \nu_4$
HCN	R(5)	729.706	44.34	ν_2
HCN	R(6)	732.658	62.08	ν_2
HCN	R(7)	735.609	82.77	ν_2
HCN	R(10)	744.458	162.57	ν_2
HCN	R(11)	747.405	195.07	ν_2
HCN	R(15)	759.180	354.61	ν_2
HCN	R(16)	762.121	401.86	ν_2
HCN	R(18)	767.996	505.21	ν_2
HCN	R(22)	779.725	747.24	ν_2
HCN	R(23)	782.652	815.09	ν_2
NH ₃	P(12,3) _s	728.813	1500.40	ν_2
NH ₃	P(12,1) _s	729.411	1528.43	ν_2
NH ₃	P(11,10) _s	743.073	937.96	ν_2
NH ₃	P(10,0) _a	745.420	1084.58	ν_2

Table 4.2 (cont'd)

Molecule	Line	Wavenumber cm ⁻¹	E_J (K)	Band
NH ₃	P(11,7)s	745.706	1124.04	ν_2
NH ₃	P(11,2)s	748.570	1284.61	ν_2
NH ₃	P(11,1)s	748.767	1295.20	ν_2
NH ₃	P(11,0)s	748.834	1298.72	ν_2
NH ₃	P(9,7)a	749.863	711.55	ν_2
NH ₃	P(9,3)a	760.694	856.66	ν_2
NH ₃	P(9,2)a	761.918	874.62	ν_2
NH ₃	P(9,1)a	762.641	885.37	ν_2
NH ₃	P(10,6)s	766.253	955.11	ν_2
NH ₃	P(10,5)s	766.871	994.77	ν_2
NH ₃	P(8,7)a	767.037	533.67	ν_2
NH ₃	P(10,4)s	767.396	1027.08	ν_2
NH ₃	P(10,3)s	767.809	1052.11	ν_2
NH ₃	P(10,2)s	768.128	1069.95	ν_2
NH ₃	P(8,0)a	780.568	712.35	ν_2
NH ₃	P(8,7)s	805.779	532.89	ν_2

Table 4.2 (cont'd)

Molecule	Line	Wavenumber cm ⁻¹	E_J (K)	Band
NH ₃	P(8,6)s	806.274	580.78	ν_2
NH ₃	P(8,5)s	806.738	621.07	ν_2
NH ₃	P(8,4)s	807.144	653.87	ν_2
NH ₃	P(8,3)s	807.472	679.29	ν_2
NH ₃	P(8,2)s	807.722	697.40	ν_2
NH ₃	P(8,1)s	807.872	708.24	ν_2
NH ₃	P(6,5)a	809.715	325.13	ν_2
NH ₃	P(6,4)a	812.301	358.28	ν_2
NH ₃	P(6,3)a	814.241	383.98	ν_2
NH ₃	P(6,2)a	815.591	402.28	ν_2
NH ₃	P(6,1)a	816.386	413.24	ν_2
NH ₃	P(6,0)a	816.651	416.89	ν_2
NH ₃	P(5,4)s	867.520	238.65	ν_2
NH ₃	P(5,3)s	867.720	264.52	ν_2
NH ₃	P(5,2)s	867.873	282.94	ν_2
NH ₃	P(5,1)s	867.969	293.97	ν_2

Table 4.2 (cont'd)

Molecule	Line	Wavenumber cm ⁻¹	E_J (K)	Band
NH ₃	P(5,0)s	868.002	297.64	ν_2
NH ₃	P(2,1)s	928.232	55.94	ν_2
NH ₃	Q(10,8)a	928.558	853.91	ν_2
NH ₃	Q(5,5)a	928.754	206.09	ν_2
NH ₃	Q(7,6)a	929.162	423.22	ν_2
NH ₃	Q(12,9)a	929.642	1244.37	ν_2
NH ₃	Q(4,4)a	929.898	140.16	ν_2
NH ₃	Q(9,7)a	929.970	711.55	ν_2
NH ₃	Q(6,5)a	930.307	325.13	ν_2
NH ₃	Q(3,3)a	930.757	86.66	ν_2
NH ₃	Q(11,8)a	931.062	1070.38	ν_2
NH ₃	Q(8,6)a	931.122	581.47	ν_2
NH ₃	Q(5,4)a	931.177	239.41	ν_2
NH ₃	Q(2,2)a	931.333	45.59	ν_2
NH ₃	Q(1,1)a	931.628	16.96	ν_2
NH ₃	Q(4,3)a	931.774	166.09	ν_2

Table 4.2 (cont'd)

Molecule	Line	Wavenumber cm ⁻¹	E_J (K)	Band
NH ₃	Q(7,5)a	932.011	463.71	ν_2
NH ₃	Q(3,2)a	932.094	105.18	ν_2
NH ₃	Q(2,1)a	932.136	56.71	ν_2
NH ₃	Q(10,7)a	932.235	908.58	ν_2
NH ₃	Q(6,4)a	932.636	358.28	ν_2
NH ₃	Q(3,1)a	932.881	116.28	ν_2
NH ₃	Q(5,3)a	932.992	265.23	ν_2
NH ₃	Q(4,2)a	933.076	184.55	ν_2
NH ₃	Q(9,6)a	933.157	759.00	ν_2
NH ₃	Q(12,8)a	933.508	1305.65	ν_2
HNCO	P(19)0-1L	732.525	380	ν_4
HNCO	P(17)0-1L	733.871	306	ν_4
HNCO	P(15)0-1L	735.229	240	ν_4
HNCO	P(5)0-1L	742.922	30	ν_4
HNCO	P(3)0-1L	744.360	12	ν_4
HNCO	P(1)0-1L	745.800	2	ν_4

Table 4.2 (cont'd)

Molecule	Line	Wavenumber cm ⁻¹	E_J (K)	Band
HNCO	R(2)0-1L	748.744	6	ν_4
HNCO	R(3)0-1L	749.492	12	ν_4
HNCO	R(4)0-1L	750.242	20	ν_4
HNCO	P(36)0-0	750.495	1332	ν_4
HNCO	R(5)0-1L	750.992	30	ν_4
HNCO	R(16)0-1L	759.433	272	ν_4
HNCO	P(23)0-0	759.860	552	ν_4
HNCO	R(17)0-1L	760.219	306	ν_4
HNCO	P(22)0-0	760.584	506	ν_4
HNCO	R(18)0-1L	761.007	342	ν_4
HNCO	P(21)0-0	761.309	462	ν_4
HNCO	P(20)0-0	762.033	420	ν_4
HNCO	P(19)0-0	762.759	380	ν_4
HNCO	R(20)0-1L	762.593	420	ν_4
HNCO	P(18)0-0	763.485	342	ν_4
HNCO	R(21)0-1L	763.390	462	ν_4

Table 4.2 (cont'd)

Molecule	Line	Wavenumber cm ⁻¹	E_J (K)	Band
HNCO	R(24)0-1L	765.800	600	ν_4
HNCO	P(14)0-0	766.393	210	ν_4
HNCO	P(13)0-0	767.121	182	ν_4
HNCO	P(12)0-0	767.849	156	ν_4
HNCO	P(11)0-0	768.578	132	ν_4
HNCO	P(10)0-0	769.307	110	ν_4
HNCO	P(9)0-0	770.037	90	ν_4
HNCO	R(1)0-0	778.090	2	ν_4
HNCO	P(28)1U-1U	777.947	812	ν_4
HNCO	P(29)1L-1L	777.746	870	ν_4
HNCO	R(2)0-0	778.824	6	ν_4
HNCO	P(27)1U-1U	778.640	756	ν_4
HNCO	P(28)1L-1L	778.401	812	ν_4
HNCO	P(26)1U-1U	779.333	702	ν_4
HNCO	P(27)1L-1L	779.060	756	ν_4
HNCO	P(25)1U-1U	780.028	650	ν_4

Table 4.2 (cont'd)

Molecule	Line	Wavenumber cm ⁻¹	E_J (K)	Band
HNCO	P(26)1L-1L	779.721	702	ν_4
HNCO	P(24)1U-1U	780.724	600	ν_4
HNCO	R(5)0-0	781.029	30	ν_4
HNCO	P(23)1U-1U	781.420	552	ν_4
HNCO	P(24)1L-1L	781.053	600	ν_4
HNCO	R(6)0-0	781.765	42	ν_4
HNCO	P(22)1U-1U	782.118	506	ν_4
HNCO	P(23)1L-1L	781.723	552	ν_4
HNCO	R(7)0-0	782.501	56	ν_4
HNCO	P(21)1U-1U	782.818	462	ν_4
HNCO	P(22)1L-1L	782.396	506	ν_4
HNCO	R(9)1L-1L	805.318	90	ν_4
HNCO	R(10)1U-1U	806.098	110	ν_4
HNCO	R(10)1L-1L	806.076	110	ν_4
HNCO	R(11)1U-1U	806.857	132	ν_4
HNCO	R(11)1L-1L	806.836	132	ν_4

Table 4.2 (cont'd)

Molecule	Line	Wavenumber cm ⁻¹	E_J (K)	Band
HNCO	R(12)1U-1U	807.617	156	ν_4
HNCO	R(12)1L-1L	807.599	156	ν_4
HNCO	R(13)1U-1U	808.379	182	ν_4
HNCO	R(13)1L-1L	808.365	182	ν_4
HNCO	R(14)1U-1U	809.142	210	ν_4
HNCO	R(14)1L-1L	809.133	210	ν_4
HNCO	P(25)1L-0	809.585	650	ν_4
HNCO	R(15)1U-1U	809.907	240	ν_4
HNCO	R(15)1L-1L	809.904	240	ν_4
HNCO	P(24)1L-0	810.319	600	ν_4
HNCO	P(23)1L-0	811.053	552	ν_4
HNCO	R(16)1U-1U	810.672	272	ν_4
HNCO	R(16)1L-1L	810.677	272	ν_4
HNCO	P(22)1L-0	811.788	506	ν_4
HNCO	R(17)1U-1U	811.440	306	ν_4
HNCO	R(17)1L-1L	811.453	306	ν_4

Table 4.2 (cont'd)

Molecule	Line	Wavenumber cm ⁻¹	E_J (K)	Band
HNCO	P(21)1L-0	812.523	462	ν_4
HNCO	R(18)1U-1U	812.209	342	ν_4
HNCO	R(18)1L-1L	812.232	342	ν_4
HNCO	P(20)1L-0	813.258	420	ν_4
HNCO	R(19)1U-1U	812.979	380	ν_4
HNCO	R(19)1L-1L	813.013	380	ν_4
HNCO	R(20)1U-1U	813.750	420	ν_4
HNCO	R(20)1L-1L	813.797	420	ν_4
HNCO	P(19)1L-0	813.993	380	ν_4
HNCO	R(21)1U-1U	814.522	462	ν_4
HNCO	P(18)1L-0	814.728	342	ν_4
HNCO	P(17)1L-0	815.464	306	ν_4
HNCO	R(22)1U-1U	815.295	506	ν_4
HNCO	R(22)1L-1L	815.373	506	ν_4
HNCO	P(16)1L-0	816.199	272	ν_4
HNCO	R(23)1U-1U	816.070	552	ν_4

Table 4.2 (cont'd)

Molecule	Line	Wavenumber cm ⁻¹	E_J (K)	Band
HNCO	R(23)1L-1L	816.165	552	ν_4
HNCO	P(33)2U-2U	816.181	1122	ν_4
HNCO	P(33)2L-2L	816.196	1122	ν_4
HNCO	P(15)1L-0	816.935	240	ν_4
HNCO	R(24)1U-1U	816.845	600	ν_4
HNCO	R(24)1L-1L	816.960	600	ν_4
HNCO	P(32)2U-2U	816.938	1056	ν_4
HNCO	P(32)2L-2L	816.951	1056	ν_4
HNCO	P(14)1L-0	817.670	210	ν_4
HNCO	R(25)1U-1U	817.621	650	ν_4
HNCO	R(25)1L-1L	817.758	650	ν_4
HNCO	P(31)2U-2U	817.695	992	ν_4
HNCO	P(31)2L-2L	817.706	992	ν_4
HNCO	P(13)1L-0	818.406	182	ν_4
HNCO	R(26)1U-1U	818.398	702	ν_4
HNCO	R(26)1L-1L	818.558	702	ν_4

Table 4.2 (cont'd)

Molecule	Line	Wavenumber cm ⁻¹	E_J (K)	Band
HNCO	P(30)2U-2U	818.450	930	ν_4
HNCO	P(30)2L-2L	818.460	930	ν_4
HNCO	P(12)1L-0	819.141	156	ν_4
HNCO	R(27)1U-1U	819.175	756	ν_4
HNCO	P(29)2U-2U	819.206	870	ν_4
HNCO	P(29)2L-2L	819.214	870	ν_4
HNCO	P(11)1L-0	819.876	132	ν_4
HNCO	R(27)1L-1L	819.361	756	ν_4
HNCO	R(28)1U-1U	819.954	812	ν_4
HNCO	R(28)1L-1L	820.167	812	ν_4
HNCO	P(28)2U-2U	819.960	812	ν_4
HNCO	P(28)2L-2L	819.967	812	ν_4
HNCO	P(10)1L-0	820.612	110	ν_4
HNCO	R(29)1L-1L	820.976	870	ν_4
HNCO	P(27)2U-2U	820.713	756	ν_4
HNCO	P(27)2L-2L	820.720	756	ν_4

Table 4.2 (cont'd)

Molecule	Line	Wavenumber cm ⁻¹	E_J (K)	Band
HNCO	P(9)1L-0	821.347	90	ν_4
HNCO	R(30)1L-1L	821.788	930	ν_4
HNCO	P(26)2U-2U	821.466	702	ν_4
HNCO	P(26)2L-2L	821.472	702	ν_4
HNCO	P(8)1L-0	822.081	72	ν_4
HNCO	P(25)2U-2U	822.218	650	ν_4
HNCO	P(25)2L-2L	822.223	650	ν_4
CH ₃	R(7,5)	745.829	414.56	ν_2
CH ₃	R(8,1)	750.220	680.76	ν_2
CH ₃	R(7,6)	750.108	361.79	ν_2
CH ₃	R(8,0)	749.858	685.50	ν_2
CH ₃	R(8,6)	763.274	514.24	ν_2
CH ₃	R(9,3)	765.937	813.14	ν_2
CH ₃	R(9,4)	768.462	780.08	ν_2
CH ₃	R(8,7)	768.342	451.97	ν_2
CH ₃	R(10,3)	778.189	1001.70	ν_2

Table 4.2 (cont'd)

Molecule	Line	Wavenumber cm ⁻¹	E_J (K)	Band
CH ₃	R(9,7)	780.796	623.34	ν_2
CH ₃	R(10,4)	780.654	968.86	ν_2
CH ₄	P(9)	1245.220	470.87	ν_2/ν_4 dyad
CH ₄	P(9)	1245.769	470.87	ν_2/ν_4 dyad
CH ₄	P(9)	1246.453	470.86	ν_2/ν_4 dyad
CH ₄	P(10)	1247.705	575.06	ν_2/ν_4 dyad
CH ₄	P(9)	1247.823	470.83	ν_2/ν_4 dyad
CH ₄	P(10)	1247.843	575.05	ν_2/ν_4 dyad
CH ₄	P(9)	1249.627	470.81	ν_2/ν_4 dyad
CH ₄	P(9)	1250.001	470.80	ν_2/ν_4 dyad
CH ₄	P(5)	1277.473	157.12	ν_2/ν_4 dyad
CH ₄	P(4)	1281.611	104.78	ν_2/ν_4 dyad
CH ₄	P(4)	1282.984	104.78	ν_2/ν_4 dyad
CH ₄	P(4)	1283.459	104.77	ν_2/ν_4 dyad
CH ₄	R(0)	1311.43	0.00	ν_2/ν_4 dyad
CS	P(15)	1246.424	240	ν_2

Table 4.2 (cont'd)

Molecule	Line	Wavenumber cm ⁻¹	E_J (K)	Band
CS	P(14)	1248.221	210	ν_2
CS	P(13)	1250.006	182	ν_2
CS	R(4)	1280.154	20	ν_2
CS	R(5)	1281.717	30	ν_2
CS	R(6)	1283.268	42	ν_2

Note. — Only lines that were individually detected at the $3\text{-}\sigma$ level are included in this list.

4.3 Spectrum Fitting

4.3.1 Method

To derive physical parameters of the absorbing gas, model spectra were fitted to the observations. For this purpose, the data were divided into two groups. All data at wavenumbers between 700 and 1000 cm⁻¹ (10.7 – 13.7 μm) were fitted simultaneously, and data at 1240–1280 cm⁻¹ (8 μm) were fitted separately. The Marquardt fitting procedure (Bevington & Robinson 2003) was used, which minimizes χ^2 , the summed squared deviation normalized by the squared noise, between the data and the model.

Fitting was first attempted with a single component for each molecule, but the residuals suggested that a better fit could be obtained with multiple velocity components. The model that we used assumed that each molecule is found in one or two absorbing ‘components’. Each component is described

by its Doppler shift, V_{LSR} , its Gaussian line width ($1/e$ half width), b , the molecule's column density, N , the rotational temperature of the gas, T , and the covering factor, C , (the fraction of the background continuum source covered by the component). The fitted column density is the average over the partially covered source, so the column density in the covered portion would be N/C . A covering factor of, e.g., 10% means that lines saturate at 90% of the continuum flux. This could result from a partially covered source, from veiling (continuum emission from foreground or surrounding material), or from re-emission in the lines by the absorbing molecules. Each component was assumed to only overlap by the product of the covering factors (see Fig. 4.5). The following equation was used to calculate the observed transmission:

$$I_{\text{obs}} = I_0(1 - C_1(1 - e^{-\tau_1(\nu)}))(1 - C_2(1 - e^{-\tau_2(\nu)})). \quad (4.1)$$

where C_1 and C_2 are the covering factors for the two components. This results in a greater absorption in saturated lines than would result if the optical depths were added first and then the transmission spectrum was calculated from the optical depth spectrum. This approach was chosen because it gave a better fit to the data than adding the optical depths first and assuming the same covering factor, but it assumes that different components absorb along different lines of sight to a partially covered continuum source, which may not be the case.

A frequency correction was allowed for each spectral setting observed, to correct for errors in wavelength calibration. With only one exception, the

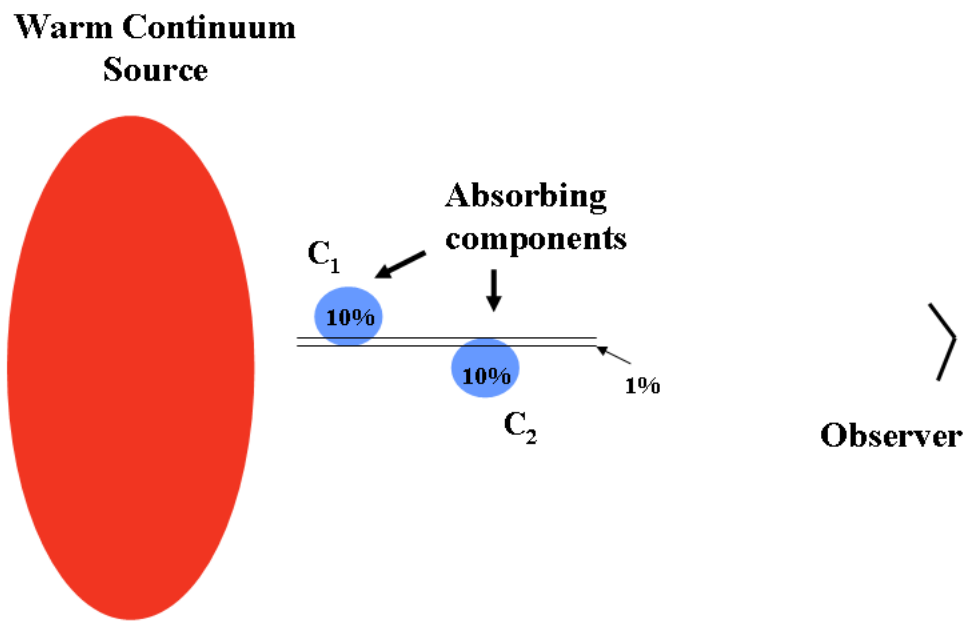


Figure 4.5 This figure shows two absorbing components between the continuum source and the observer. Each component covers 10% of the continuum source. The overlap of the two absorbing regions is given by the product of their covering factor. In this case, only 1% of the continuum source is covered by both components.

correction was less than a 1 km s^{-1} Doppler shift. In addition, a broadening of the instrumental resolution was permitted in the fitting to allow for imperfect internal instrument focusing, or possibly a ‘macroturbulent’ broadening in the absorbing gas. The fitting program chose a resolution a factor of 1.2 greater than that derived from gas cell data. A constant frequency resolution (as opposed to a constant Doppler resolution) was used in each of the two fitted regions. This represents well the improving resolving power toward shorter wavelengths in the $10.7\text{-}13.7 \mu\text{m}$ region. In addition to these parameters, the continuum, slope, and curvature of each echelon order were varied, to allow correction of the baseline fitting done during data reduction. The continuum fitting and frequency correction required about 300 free, but rather easily determined, parameters. Fewer parameters are needed to determine the physical conditions such as temperature, column density, line width and covering factor: 70 parameters for the $10.7\text{-}13.7 \mu\text{m}$ spectra and 21 for the $8 \mu\text{m}$ region. For the $10\text{-}13 \mu\text{m}$ region, we have over 3000 points to constrain the 70 parameters of interest if we characterize the constraining points by the number of lines times the number of pixels for each line.

For C_2H_2 and HNCO , lines of several bands were observed. For C_2H_2 , in addition to lines of the Q and R branches of the ν_5 fundamental, lines of several $\nu_4 + \nu_5 - \nu_5$ and $2\nu_5 - \nu_5$ bands (involving absorption from the excited ν_4 and ν_5 vibration states) were observed. The vibrational temperatures of the ν_4 and ν_5 states were included as free parameters in the fit. R-branch lines of the ν_5 band of $^{13}\text{CCH}_2$ were also observed, and the $^{13}\text{CCH}_2/\text{C}_2\text{H}_2$ abundance

ratio was allowed to vary, although it was kept the same in all the C_2H_2 components. We take into account that there are two locations for the carbon isotope in the C_2H_2 molecule. Two C_2H_2 lines of the $\nu_4 + \nu_5$ band at $7.6 \mu\text{m}$ were observed as well. For HNC, lines from the ν_4 band were observed. HNC is an only slightly non-linear molecule, and its spectrum consists of a series of sub-bands resembling those of a linear molecule, like C_2H_2 . Its dipole moment oscillates diagonally, giving it a-type sub-bands, with no change in the angular momentum about its long axis and only P and R branches, and b-type sub-bands, in which the angular momentum about its long axis changes, and P, Q, and R branches are seen. Since we did not have laboratory data regarding the relative strengths of the different sub-bands, we considered them to be caused by different species and summed their strengths to obtain the HNC abundance. The HCN lines observed were from the ν_2 bending mode. We included H^{13}CN lines in the fit, with an assumed $^{12}\text{C}/^{13}\text{C}$ ratio of 57, as derived from $^{13}\text{CCH}_2$. Although no H^{13}CN lines were obvious in the spectra, their inclusion lowered χ^2 significantly ($\Delta\chi^2 = 13$) and changed the best-fitting N_{HCN} noticeably (although not outside of its very large uncertainty). A better fit was obtained with $\text{HCN}/\text{H}^{13}\text{CN} = 200$, but we did not think it was justified to use a different $^{13}\text{C}/^{12}\text{C}$ ratio for C_2H_2 and HCN.

Although it might not be apparent from the spectra, given the shallowness of the lines, many of the detected lines are at least moderately saturated, and some are very saturated. The lines only appear weak because of the small covering factors (or emission filling in the absorption lines) and to a lesser ex-

tent the small line widths. This conclusion is very robust; the relative depths of lines of different opacity requires substantial saturation. This is most apparent in the near equality of the depths of the ortho and para lines in the C₂H₂ Q branch, near 730 cm⁻¹ (see top panel of Figure 4.1). HCN in the -60 km s⁻¹ component and NH₃ in the -56.5 km s⁻¹ component are so saturated that only lower limits could be placed on their abundances until their isotopomers were included in the fit to provide upper limit constraints. By including isotopomers and intrinsically weak lines, a wide enough range of line optical depths was observed to allow meaningful constraints to be placed on the molecular abundances in spite of the saturation. The fact that the ¹²C/¹³C ratio, 57, derived from the C₂H₂ lines, is toward the low end of the ratio typically observed for other molecules suggests that the column density of C₂H₂ may be underestimated, but only by a factor <2.

The observed lines of CH₃ were in the R branch of the ν_2 ‘sting-ray’ mode of this planar molecule. Each of these lines is doubled by the interaction between the electron spin and the molecular rotation (see Appendix). The CH₃ ν_2 band center is at 16.5 μm , whereas all observed lines were shortward of 13.5 μm , with $J \geq 7$, making us rather insensitive to cold CH₃. Lines of the P and Q branches of the NH₃ ν_2 band were observed. There was no evidence of ¹⁵NH₃ lines, but they were included in the fit to constrain the NH₃ abundance, as was done with H¹³CN. In the 8 μm region, which was fitted separately, lines of the ν_2/ν_4 dyad of CH₄ were observed. Because of the strong absorption by low- J lines of CH₄ in the Earth’s atmosphere, most of

the observed lines originate at $J > 4$. We were able to observe the R(0) line due to the favorable Doppler shift of the source ($\sim -57 \text{ km s}^{-1}$). The R(0) line helps constrain the temperature derived from the high J lines. We also detected and fitted absorption by CS.

The derived component parameters are given in Table 4.3. Uncertainties for the parameters, given in parentheses, are three times the square roots of the diagonal elements of the error matrix, which are uncertainties allowing all other parameters to vary. The noise in the fitted spectra is assumed to be purely photon statistical noise. With this noise estimate, the reduced $\chi^2 \approx 1.6$, indicating that non-statistical noise sources contribute moderately, or perhaps that a different model for the line profiles is justified. Including non-statistical noise, the uncertainties given might reasonably be taken to be 95% confidence intervals. The larger fractional errors are asymmetric, and would be more symmetric in the log of the parameters; parameters with errors greater than the quantity are not consistent with zero. The column densities of HNCO and CH₃ have smaller fractional uncertainties than those of C₂H₂ and HCN, whereas the covering factors have smaller uncertainties for C₂H₂ and HCN. This is because equivalent widths of lines of the molecules with more saturated lines depend more on covering factors than on column densities. All of the fitted molecules are detected with very high confidence.

Table 4.3. Results from the model fit to the spectra

Molecule	V_{LSR} km s ⁻¹	b (km s ⁻¹)	T_{ex} (K)	$N(X)$ 10 ¹⁶ (cm ⁻²)	C %
C ₂ H ₂	-55.9(0.2)	0.8(0.1)	256(20)	1.6(0.4)	6(0.7)
C ₂ H ₂	-59.6(0.1)	0.8(0.1)	205(11)	1.8(0.3)	18(1.4)
HCN	-56.0(0.3)	1.1(0.2)	202(22)	17(8.5)	7.1(0.7)
HCN	-59.9(0.1)	0.6(0.2)	350(94)	5.0(3.3)	9(2)
NH ₃	-56.5(0.3)	1.0(0.3)	194(25)	16(11)	4.4(0.5)
NH ₃	-59.8(0.2)	0.8(0.3)	281(13)	2.1(0.4)	14(5)
HNCO	-56.2(0.2)	1.4(0.2)	377(47)	0.29	2.4(0.3)
HNCO	-59.5(0.1)	1.6(0.1)	190(10)	0.24	8(1)
CH ₃	-54.3(0.2)	2.2(0.3)	253(11)	1.8(0.1)	97(6)
CH ₃	-62.6(0.3)	1.5(0.4)	931(140)	0.55(0.08)	97(6)
CH ₄	-55.9(0.4)	0.6(0.2)	248(80)	66(0.1)	6(1.6)
CH ₄	-59.4(0.2)	1.6(0.4)	218(40)	22(28)	11(2.2)
CS*	-55.7(1.8)	1.1(0.8)	248*	0.2(0.3)	100(8)

Note. — The column densities listed are $N_{\text{tot}} \times C$.

*The temperature for CS is fixed to be the same as for CH₄ because there are not enough lines to constrain it.

4.3.2 Results

For most molecules, we found two ‘components’ with Doppler shifts of $V_{\text{LSR}} = -56.4 \pm 0.3 \text{ km s}^{-1}$ and $-59.7 \pm 0.3 \text{ km s}^{-1}$, with widths of $b = 1 - 2 \text{ km s}^{-1}$ (see Table 4.3). Most of the component temperatures were in the range 200-400 K and covering factors were typically 0.04-0.08, with C_2H_2 requiring somewhat larger values of 0.06 and 0.18. HNC0 has somewhat broader component line widths but other parameters are similar. CH_3 has the broadest component line widths, with a greater velocity spacing between the two components and the hottest component. Both CS and CH_3 are fitted with much larger covering factors (consistent with 100%) than were the other molecules. The model spectra resulting from the best fit parameters can be seen in Figures 4.1 and 4.2.

In addition to agreeing among the different molecules (except CH_3), the Doppler shifts agree with the two most commonly observed values for molecules seen at radio wavelengths. This gives us some confidence that the two velocity components, at -56.5 and -60 km s^{-1} , are real, although whether they are two separate components, or just a way of describing a non-Gaussian velocity distribution is difficult to determine from the data. Generally, the temperatures of the two components for a given molecule are not very different, although a fit constraining them to be equal was significantly worse than the fit allowing all temperatures to vary. Line widths, column densities, and covering factors vary more. The fit was very poor when they were constrained to be equal for all molecules.

Note that our quoted column densities are averages over the lines of sight to the continuum emitting material, or column densities in the absorbing gas multiplied by the covering factors. Since our fitted covering factors may instead be a way of representing the effect of emission in the lines filling in the absorption, the actual column densities of our molecules could be as much as an order of magnitude larger than our quoted numbers. Alternatively, if only a small fraction of the infrared continuum source is covered by high column density material, the dust grains in this component may be nearly opaque in the silicate feature. In this case the high column density gas might not contribute to the measured silicate feature, and the column density measured by Willner (1976) would be an underestimate of the column density through which we observe. However, the column density measured by Willner may be representative since the opaque, high column density gas would not contribute to the observed molecular absorption.

4.3.3 C₂H₂ and HCN

Since our initial search for molecules began with C₂H₂ and HCN, the first models only included those two molecules. In these models, we derived similar temperatures and column densities as derived from *ISO* observations (Lahuis & van Dishoeck 2000; Boonman et al. 2003). Once we include absorption from other molecules, HNC in particular, the temperatures for HCN and especially for C₂H₂ are lowered significantly. Some HNC lines overlap with high J lines of C₂H₂, which means that more hot C₂H₂ is necessary to produce

the observed absorption when HNCO is not included in the model. In our final model including all of the observed molecules, our derived column densities of C_2H_2 , $N = 3.4 \times 10^{16} \text{ cm}^{-2}$, and HCN, $N = 2.2 \times 10^{17} \text{ cm}^{-2}$, (see Table 4.3) are larger than those derived in Lahuis & van Dishoeck, $N_{\text{C}_2\text{H}_2} = 8 \times 10^{15} \text{ cm}^{-2}$ and $N_{\text{HCN}} = 1.0 \times 10^{16} \text{ cm}^{-2}$. Part of the difference is due to the different Doppler parameter used: $b = 5 \text{ km s}^{-1}$ is used in Lahuis & van Dishoeck, whereas, we derive $b \sim 1 \text{ km s}^{-1}$. We derive lower temperatures, $T_{\text{C}_2\text{H}_2} = 200 - 250 \text{ K}$ and $T_{\text{HCN}} = 200 - 350 \text{ K}$ than derived by Lahuis & van Dishoeck, $T_{\text{C}_2\text{H}_2} = 800 \text{ K}$ and $T_{\text{HCN}} = 600 \text{ K}$, and Boonman et al. (2003), $T_{\text{C}_2\text{H}_2} = 500 \text{ K}$. We also find that we need a covering factor to account for the saturated yet shallow lines. The level of saturation is difficult to determine from the *ISO* data. In order to verify that our fit to the TEXES data is also consistent with the *ISO* observations, we take our model at the *ISO*-SWS resolution and compare to the data (Figure 4.6). The model matches the fundamental Q-branches for the two molecules as well as a hot band Q-branch of C_2H_2 .

C_2H_2 is expected to be in rotational local thermal equilibrium (LTE) since it has no permanent dipole moment. The fact that the two excited vibrational states of C_2H_2 from which absorption was observed, ν_4 and ν_5 , are found to be near LTE at the C_2H_2 rotational temperature, or even slightly higher, provides information about the physical conditions of the gas. For both bands, the hot bands indicate they are slightly out of LTE since the vibrational temperatures (T_v) are higher than the rotational temperatures (T_r). For the $\nu_4 + \nu_5 - \nu_4$ bands, the T_v temperatures for the two components were

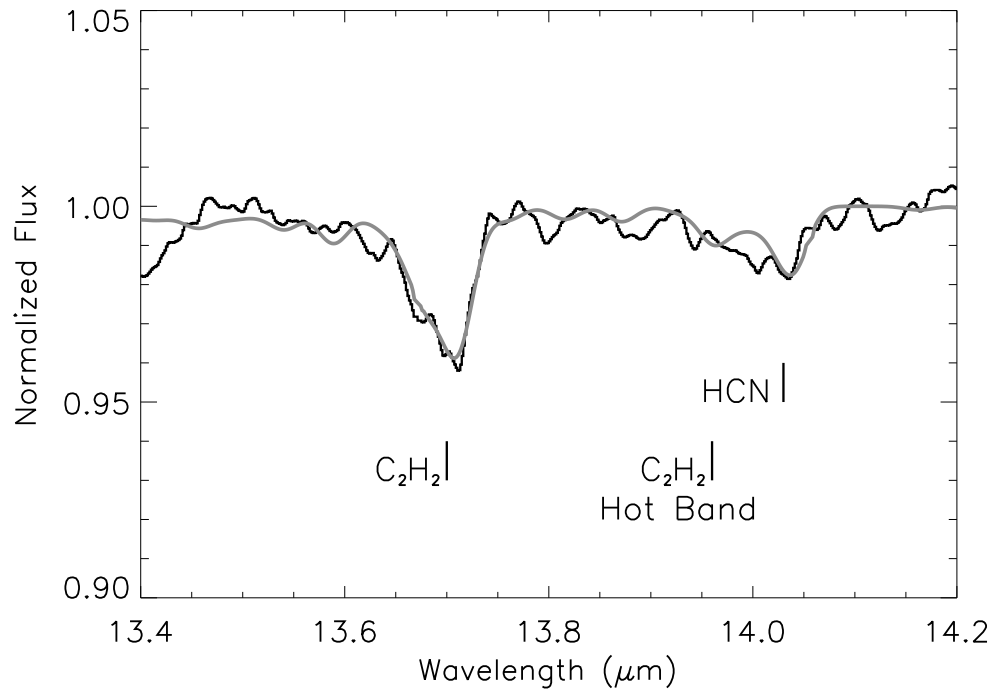


Figure 4.6 The spectrum of NGC 7538 IRS 1 as seen by *ISO* is shown in black. A fit to the C₂H₂ and HCN fundamental Q-branches as well as a hot band Q-branch of C₂H₂ is shown in grey. The parameters are set from the TEXES high-resolution observations. The models gives a good fit to the *ISO* spectrum.

370 K and 270 K while for the $2\nu_5-\nu_5$ bands, they were 320 K and 245 K. The temperatures for the ν_5 fundamental are 256 K and 205 K for the two components. In LTE, the vibrational temperatures for the hot bands would equal the rotational temperature measured by the fundamental branch lines.

The ν_4 level has no allowed radiative transitions to the ground vibrational level, and none of the rotational levels of the ground vibrational level are coupled radiatively, in both cases due to the symmetry of the C_2H_2 molecule. This suggests that the populations of the ground and ν_4 states should be set by collisions, and so should be in LTE at the same temperature. However, the ν_4 level can be radiatively pumped by absorption in the $7.6 \mu\text{m}$ $\nu_4 + \nu_5$ band followed by emission of photons in the $\nu_4 + \nu_5 - \nu_4$ band. The ν_5 state must be populated predominantly radiatively for any plausible density, since the critical density is $> 10^{10} \text{ cm}^{-3}$. From these considerations, we conclude that the brightness temperature of the radiation field seen by the observed gas must be close to the kinetic temperature of the gas. In addition, the fact that the measured rotational temperature for HCN is similar to that of C_2H_2 indicates that the rotational levels of HCN are kept populated either by collisions, which would require a gas density $> 10^7 \text{ cm}^{-3}$, or by infrared pumping through the ν_2 transitions. Lahuis & van Dishoeck (2000) conclude that either excitation mode is possible. The presence of C_2H_2 $\nu_5 = 1-2$ absorption requires infrared pumping, although $\nu_4 + \nu_5 - \nu_4$ absorption does not.

We can attempt to estimate the extent to which emission in our lines fills in the absorption, at least for C_2H_2 , by using the $2\nu_5 - \nu_5$ lines as probes of

the ν_5 population. Our spectra require a ν_5 vibrational temperature ~ 300 K. We need to compare this number to the blackbody brightness temperature of the background continuum radiation. From the shape of the 8–13 μm silicate feature, Willner derived a dust temperature of 330 K assuming the emitting dust is optically thick, or 370 K assuming optically thin silicate emission. He preferred the latter model, which gives a brightness temperature only when combined with an assumption about the solid angle subtended by the source.

The physical conditions and molecular abundances we derive can be compared to those derived by Mitchell et al. (1990) for CO. They obtain a column density of $1.5 \pm 0.3 \times 10^{17} \text{ cm}^{-2}$ for ^{13}CO in cold gas at 25 K and $1.4 \pm 0.1 \times 10^{17} \text{ cm}^{-2}$ in warm gas at 176 K. We would not be sensitive to their cold gas. Presumably their warm gas includes both of our components, although our temperatures are generally higher than theirs. If we assume $^{12}\text{CO}/^{13}\text{CO} = 45$, using the $^{12}\text{C}/^{13}\text{C}$ ratio we derived from our C_2H_2 observations, we derive the abundances of our molecules relative to CO and are listed Table 4.4. (Note that Mitchell et al. use $^{12}\text{C}/^{13}\text{C} = 89$.) However, we should note that we have measured one spectral setting including CO lines, while searching for OCS absorption near 5 μm . The noise is rather high, but it is apparent that the ^{13}CO lines are not well described by moderately saturated Gaussians, as assumed by Mitchell et al.. The ^{13}CO lines are deeper and broader than the lines of any of our other molecules, and have prominent blue-shifted shoulders probably tracing an outflow. We suspect that the lines are more saturated, and the CO column density larger than Mitchell et al.

Table 4.4. Abundances with respect to CO and H₂

Molecule	N(X)/N(CO)* 10 ⁻³	N(X)/N(H ₂)* 10 ⁻⁷
HCN	35	29
NH ₃	29	24
C ₂ H ₂	5.4	4.5
CH ₃	3.7	3.1
CH ₄	140	117
CS	0.3	0.2
HNCO	0.8	0.7

Note. — *N(CO) = 6.3×10^{18} cm⁻² and N(H₂) = 7.5×10^{22} cm⁻². We use N listed in Table 4.3.

concluded. The different shapes and greater depths of the CO lines than our C₂H₂ lines also indicates that CO probes different gas. Likely, C₂H₂ and the other molecules we observe in the mid-infrared are found only in unusual regions, whereas CO is distributed along the entire line of sight.

Alternatively, we can compare our column densities to the H₂ column density derived from the silicate absorption feature by Willner (1976), $6 - 9 \times 10^{22}$ cm⁻². This H₂ column density is consistent with the CO column density measured by Mitchell et al. and an H₂/CO ratio of $0.9 - 1.4 \times 10^4$, which is within the range normally assumed. Assuming $N_{\text{H}_2} = 7.5 \times 10^{22}$ cm⁻², we derive the abundances relative to H₂ given in Table 4.4. For C₂H₂ and HCN,

we find abundances of 4.5×10^{-7} and 2.9×10^{-6} with respect to H_2 . These abundances are enhanced in relation to cold cloud abundances. The chemistry leading to the enhanced abundances will be discussed below (Chapter 4.4.2).

Given the many assumptions and uncertainties in this calculation, it is difficult to make a strong statement, but the level at which our C_2H_2 lines saturate, $\sim 85\%$ of the continuum, which we model with a small covering factor, could instead be due partly or entirely to emission by the absorbing gas. Presumably the same statement applies to the other observed molecules. The required column densities are the ratios of the column densities and the covering factors given in Table 4.3.

4.3.4 NH_3

From our infrared observations, we find that NH_3 has two components: one at -56.5 km s^{-1} and the other at -59.8 km s^{-1} . Most of the NH_3 is found in the first component, for which the temperature is $\sim 200 \text{ K}$ and the column density is $1.6 \times 10^{17} \text{ cm}^{-2}$. The second component has a higher temperature ($\sim 280 \text{ K}$) and the column density is 8 times less than for the first component (see Table 4.3). NH_3 absorption toward IRS 1 has also been studied in the radio by Wilson et al. (1983) and Henkel, Wilson, & Johnston (1984). They found $N_{\text{NH}_3} = 2 \times 10^{18} \text{ cm}^{-2}$ in gas with $T = 170\text{--}220 \text{ K}$ and $V_{\text{LSR}} = -60 \text{ km s}^{-1}$. Although their temperature and Doppler shift is in reasonable agreement with our bluer absorption components, their column density is nearly 10 times ours. Without constraining the $^{15}\text{N}/^{14}\text{N}$ isotopic ratio, our NH_3 column is within

a factor of two of the column derived from radio observations. Although no $^{15}\text{NH}_3$ lines are observed, using their absence to constrain the column of $^{14}\text{NH}_3$ is important. However, if the difference is real, then it is possible that we sample only a fraction of the column observed at cm wavelengths as a result of larger dust opacity at mid-infrared wavelengths. It may be notable that Wilson et al. found, as did we, that although relative depths of lines (in their case hyperfine components) require large optical depths, line shapes do not appear flat-bottomed as would be expected if they are optically thick. They suggest that the absorbing gas may be in small spectrally and spatially unresolved clumps, each of which is optically thick, and which combine to make a line that does not have the shape of a thick line. Our use of two components in our fit may be a way of approximating this situation. The abundance of NH_3 with respect to H_2 (2.4×10^{-6}) is also enhanced compared to the cold envelope. The cold material around IRS 1 probed by Zheng et al. (2001) had a smaller abundance of NH_3 . It is possible that NH_3 ice is evaporating from icy mantles close to the protostar. Thus, the abundance we observe is enhanced in the inner warm gas.

4.3.5 HNC O

Since the HNC O temperature and velocities derived from our observations agree with the values for the other molecules, we can assume that HNC O is probing the same gas. It appears the region probed by HNC O is very small in angular size. Zinchenko et al. (2000) detect HNC O emission in the radio

and derive a column density of $1.1 \times 10^{14} \text{ cm}^{-2}$. This value is an order of magnitude lower than our observed column density. However, beam dilution in the radio observations can explain the difference in the column densities. Like other molecules mentioned above, gas-phase HNC₂O is possibly coming from evaporation of grain mantles. The $4.62 \mu\text{m}$ feature observed toward some protostars has been attributed to OCN⁻ (e.g., Lacy et al. 1984; Pendleton et al. 1999; van Broekhuizen et al. 2004). Recent *ISO* results of solid state features toward protostars show an upper limit of 10^{16} cm^{-2} toward IRS 1 (Gibb et al. 2004). The total column derived in this work is $5.4 \times 10^{15} \text{ cm}^{-2}$, a factor of 2 lower than the solid OCN⁻ limit. In general, IRS 1 does not show many ice features compared to the colder nearby source IRS 9 (see Gibb et al. 2004), which has a column density $N(\text{OCN}^-) = 1.2 \times 10^{17} \text{ cm}^{-2}$. If solid OCN⁻ sublimates and recombines to form HNC₂O, the expected column density for HNC₂O would be comparable to the observed OCN⁻ ice toward cold lines of sight (like IRS 9). However, the gas-phase column observed is at least an order of magnitude smaller than that of the solid state ion. This indicates that when OCN⁻ sublimates, a fraction of the ices goes into forming HNC₂O, while most of HNC₂O is destroyed in the warm gas-phase chemistry on short time scales. Further studies of how OCN⁻ reacts in the gas-phase are needed in order to understand the difference between ice and gas phase column densities.

4.3.6 CH₃

CH₃ is detected for the first time toward warm, dense gas. The parameters derived for this molecule do not agree as well with the other molecules. The separation between the centroid velocities for the two components is nearly twice the separation found for the other molecules, $V_{\text{LSR}} = -54.3$ and -62.6 km s⁻¹. Also, the covering for both of the components is 100%, whereas as it is closer to 10% for the other molecules. In addition, the temperature of the second component is much hotter (>900 K) than the temperatures derived for the other molecules. These pieces of evidence indicate that the material traced by CH₃ has a larger extent and is closer to the protostar (and hence warmer). It is possible that the hotter component probes a region where CH₄ is being destroyed efficiently to form CH₃. The abundance of CH₃ is higher than expected and is comparable to C₂H₂. The chemical implications of a high CH₃ abundance are described in Chapter 4.4.2.

4.3.7 CH₄ and CS

CH₄ gas-phase absorption had been observed toward the neighboring protostar IRS 9 (Lacy et al. 1991; Boogert et al. 2004a) but had never been seen toward IRS 1. We find that the centroid velocities, temperatures, and covering factors for the two components are very similar to those of C₂H₂ and other molecules (see Table 4.3). From all of the observed molecules, CH₄ has the highest abundance with respect to H₂ (1.2×10^{-5}). Such a high abundance seems to indicate that CH₄ is evaporating from the grain mantles and thus

the gas-phase abundance is highly enhanced compared with the cold molecular envelope. Studies of the solid CH_4 content toward IRS 1 show that the column density is 100 times less than our observed gas-phase column (Gibb et al. 2004), suggesting that the solid CH_4 on grains has sublimated. Also, CH_3 can be formed from the destruction of CH_4 . Since we observe a high abundance of CH_3 , CH_4 must have had an even higher abundance in order to produce CH_3 at the observed levels. Chapter 4.4.2 describes model predictions for the relative abundances of CH_3 and CH_4 .

We detect only 6 lines of CS, all of which are from similar rotational levels ($J = 4-6, 13-15$; see Table 4.2). This prevents us from constraining the temperature. Since most molecules agree on temperatures between 200–250 K, we assume the temperature to be the same as CH_4 . The centroid velocities agree with the values for other molecules which indicates that the assumed temperature is appropriate. However, the covering factor is 100%, but it is unclear whether we have enough constraints to fit all of the parameters for CS. From radio studies of the envelope around IRS 1, a CS abundance of $\sim 10^{-10}$ is found (Plume et al. 1997; Mueller et al. 2002; Shirley et al. 2003). However, also using radio observations, van der Tak et al. (2000) derive a CS abundance closer to our observed abundance of 10^{-8} . It is possible that the infrared CS absorption traces material in the envelope, but, since warm temperature fits the observations, it is also possible that it traces the warm inner region.

4.4 Models

4.4.1 Physical Models

We now attempt to construct a physical and geometrical model of NGC 7538 IRS 1. Within the possible scenarios presented from various radio and infrared observations (e.g., Minier et al. 2001; Lugo et al. 2004; De Buizer & Minier 2005; Kraus et al. 2006), we propose a scenario in which the molecular absorption presented here comes from a circumstellar disk. We will examine other possibilities first. Figure 4.7 depicts the possible scenarios allowed by the available observations.

We can quickly rule out a simple model in which the absorbing molecular gas is in the foreground molecular cloud and not closely associated with IRS 1. Our observations require the gas to be much hotter ($T \sim 300$ K) and denser ($n_{\text{H}_2} \sim 10^7 \text{ cm}^{-3}$ to maintain rotational LTE of HCN out to $J = 21$) than is found away from luminous sources in molecular clouds. In addition, the infrared radiation field must have a brightness temperature ~ 300 K to maintain vibrational LTE of the $\text{C}_2\text{H}_2 \nu_5$ level. Undoubtedly, the absorbing molecular gas is in close proximity to the infrared continuum source IRS 1.

It is not quite so easy to rule out a model in which the absorbing molecules are in the warm inner envelope around the IRS 1 hypercompact H II region. This gas could be compressed by the ionized wind, and if it is as close as $0.1''$, or 280 AU, from a $10^5 L_\odot$ source it would have a temperature near 300 K. The temperature structure determined by van der Tak et al. (2000) indicates that indeed temperatures range from 200 – 400 K at radii of

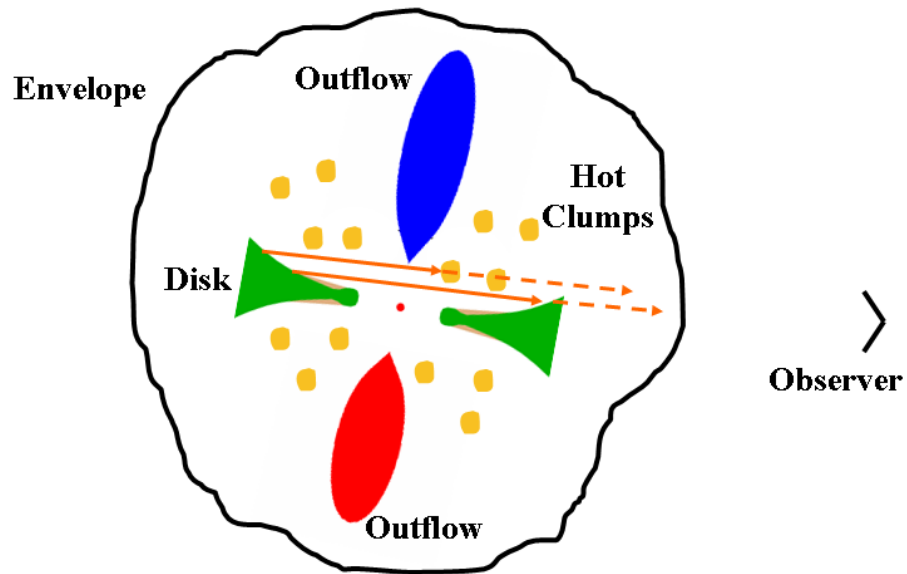


Figure 4.7 This is cartoon representation of the IRS 1 region. The absorbing material containing the molecules observed can either be located in the disk or in the hot clumps, while the continuum is coming from the photo-evaporating layers of the disk. The continuum can also be from other parts of the disk for which lines of sight do not cross the material with our molecules. There is also more extended dust emission from the envelope that contributes to the continuum but does not contain our molecules in high abundances.

220–380 AU. However, interaction with the ionized wind, which has a velocity $\sim 100 \text{ km s}^{-1}$, would be expected to accelerate the gas, causing broad, blue-shifted absorption. In contrast, the observed lines have widths of $< 8 \text{ km s}^{-1}$ and have centroids within a few km s^{-1} of those seen in surrounding molecular gas. Another argument against the presence of the observed gas in an envelope around IRS 1 is the fact that net absorption is seen. Since the vibrational temperature is comparable to the brightness temperature of the continuum radiation, emission lines would be seen if the molecular gas had a larger extent than the continuum source. If the lines arose in molecular shell surrounding the hypercompact H II region, this probably would be the case.

On the other hand, Campbell (1984b) proposes that the centimeter continuum from IRS 1 results from partially ionized material in an outflow. The centimeter continuum emission has been spatially resolved into clumps by Gaume et al. (1995), who suggest that the emission comes from photo-evaporation of knots of neutral molecular material (see 4.7). The CH_3OH masers seen by Minier et al. (2001) also seem to trace the clumpy structure probed by the cm continuum emission. If we compare the velocities we derive for the two components of our molecules to those observed for the CH_3OH masers, we find that they match the two velocities found for the A cluster of masers. This indicates that the infrared observations may be tracing the same gas as the CH_3OH masers.

We propose that the absorbing material is in a circumstellar disk. There is evidence for a disk close to edge-on from other observations and models

(e.g., Pestalozzi et al. 2004; Lugo et al. 2004; De Buizer & Minier 2005). Hot dust in the surface layers or the inner rim of a flared disk provides the continuum source. Material deeper into the disk can then absorb some of the infrared continuum going into the disk. Because the disk is inclined, the absorbing material does not cover the entire continuum source which results in the veiling effect seen in the absorption lines. This scenario is similar to the one described by Lahuis et al. (2006) to describe C₂H₂ and HCN absorption toward the low-mass protostar IRS 46. Detailed modeling of the disk structure of IRS 46 showed that it was possible to have the absorbing material in the disk illuminated by the continuum from the surface. Figure 4.7 illustrates a cartoon of our proposed picture, where the orange rays represent the continuum. Some of the continuum radiation passes through the absorbing outer disk.

4.4.2 Chemical Models

We now consider the implications of the observations for the chemistry of the observed material. Hot core models can be used to represent the two likely scenarios postulated above: 1) material in a circumstellar disk and 2) photo-evaporating clumps of neutral molecular material. Hot cores are small ($r < 0.1$ pc), dense ($n_{\text{H}_2} > 10^7$ cm⁻³) and hot ($T > 100$ K) regions associated with high-mass protostars (Kurtz et al. 2000). Chemically, hot cores are identified by an enhanced abundance of fully hydrogenated molecules such as H₂O and NH₃, which are usually observed through rotational transitions at sub-millimeter and millimeter wavelengths. These abundances are enhanced

with respect to the cold molecular envelope. A hot core is thought to form as a result of the protostar heating the envelope, which triggers ice sublimation from the grain mantles (Charnley et al. 1992). HNCO is another hot core molecule which has been found in the Orion hot core with an abundance $\sim 10^{-8}$ (Zinchenko et al. 2000). HCN and C₂H₂ could be sublimating from icy grain mantles or formed by the warm gas-phase chemistry. In addition, molecules such as CH₃ are the daughter molecules of the sublimated ices. CH₃ is formed through the destruction of CH₄ through photo-dissociation although this process is thought to favor the production of CH₂.

From the parameters listed in Table 4.3, two major divisions between the gas being traced are apparent. As mentioned in Chapter 4.3, the covering factors for C₂H₂, HCN, NH₃, HNCO, and CH₄ are between 3-18%, whereas for CH₃ and CS, it is 100%. Since the material being traced by CH₃ and CS is more extended, it is possible that these molecules are found in the inner envelope surrounding the protostar as well as in the material closer to the protostar or in the surface layers of the disk. The other molecules might trace a clumpier region that does not cover the continuum source or the gas in a disk with the dust in the surface and envelope filling in the absorption (so as to get shallow, saturated lines, see Chapter 4.3). The temperatures derived for the various molecules (see Table 4.3) indicate that the material is between 220–400 AU away from the central source (van der Tak et al. 2000). At a distance of 350 AU, the difference in velocity between the blue- and red-shifted sides of the disk is $\sim 3.1 \text{ km s}^{-1}$, which is similar to the splitting between the two

components of C₂H₂, HCN, NH₃ and HNCO.

From our observations we see a high abundance of the parent molecules NH₃ and CH₄. High abundances of the other molecules are also observed. Nomura & Millar (2004) present a time dependent chemical evolution of molecules in a hot core. The models begin at the time when the protostar turns on ($t = 0$ yrs). Table 4.5 shows the abundances with respect to CO at an age of 10⁴ years. The hot core model seems to underpredict abundances with respect to CO of all our observed molecules. As mentioned in Chapter 4.3.3, the CO column density found by Mitchell et al. (1990) may not be the appropriate number with which to compare our observations. If the CO column is larger than the column measured by Mitchell et al., then perhaps the abundances from the model will more closely resemble the observations. We can also compare the relative abundances between our observed molecules. The observed and predicted values for $N(\text{CH}_3)/N(\text{CH}_4)$ are similar, ~ 0.01 . For the other molecules the ratios from the models at an age of 10⁴ years are very different from the observed values. However, if we compare the observations to predictions for 10⁵ years, the agreement in the relative abundances of, for example, HCN and NH₃ improves substantially.

If we consider the disk scenario, we can also compare our observations to a chemical model of a photo-evaporating disk. Nguyen et al. (2002) present a chemical model for a disk around a 10 M_⊙ star. The model consists of a flared disk with a photo-evaporating layer on the surface. Table 4.5 compares our derived abundances with respect to CO for the various molecules to the

Table 4.5. $N(X)/N(\text{CO})$ from chemical models

Molecule	Observed (10^{-3})	Hot Core Model ^a (10^{-3})	Disk Models ^b (10^{-3})
HCN	35	0.02	16 – 24
NH ₃	29	0.76	1 – 6
C ₂ H ₂	5.4	0.88	0.06 – 0.1
CH ₃	3.7	0.016	0.02 – 1.6
CH ₄	117	1.6	7 – 35
CS*	0.2	0.0031	0.03 – 0.07

Note. — The model values were taken at 10^4 years.

References. — ^a Nomura & Millar 2004 and H. Nomura, private communication 2004, ^b Nguyen et al. 2002

predicted values from disk models. The summarized results of models taking the midplane temperature for the temperature of the layers below the photo-dissociation region (PDR) are discussed here. The difference among the three models is the variation in the X-ray ionization rate, ζ ($1\zeta = 1.3 \times 10^{-17} \text{s}^{-1}$), from 1 to $10^5 \zeta$. Table 4.5 shows that the abundance for C_2H_2 is underpredicted. In the chemical model, C_2H_2 is produced only by gas phase reactions. One possible explanation is that C_2H_2 is formed as ice on grain mantles. The abundance of NH_3 is also underpredicted. The model with the highest X-ray ionization rate produces CH_3 abundances close to the observed value. For that model, $N(\text{CH}_3)/N(\text{CH}_4)$ is 4 times larger than the observed ratio. HCN is the only molecule whose predicted abundance is close to the observed value. These models do not fit our observations very well but can serve as a guide to the expected abundances in such a scenario. The model by Nguyen et al. has not been modified to try to fit data. So, adapting the model for this object may give predictions closer to the observations. The star in NGC 7538 IRS 1 is believed to be a $30 M_\odot$ star. The different radiation field may affect the resulting chemistry.

Doty et al. (2002) present a model of chemical evolution of the envelopes of massive protostars using AFGL 2591 as an example. From that model, they conclude that enhancements of C_2H_2 , HCN and CH_4 are possible at late times in the evolution ($> 10^5$ years) and at high temperature ($T \sim 800$ K). Our derived temperatures indicate cooler material, yet the molecules seem to be enhanced in the line of sight. Alternatively, these species could be produced

at high temperature in the inner disk, and subsequently brought outward by the disk wind. Including UV and X-ray radiation in the model affects the chemistry especially relating to HCN. Stäuber et al. (2004, 2005) find that increasing the UV and X-ray flux can lead to enhanced HCN starting by the ionization of N_2 . The column densities for HCN and CS from the Stäuber et al. model of protostar AFGL 2591 agree with our observed abundances while their column densities for C_2H_2 , CH_4 , and NH_3 are lower than our observed values.

Hot core and disk chemistry models predict the enhancement of molecules such as C_2H_2 , CH_4 , and NH_3 . However, the observed abundance of C_2H_2 is higher than what models predict from warm gas-phase chemistry (see Table 4.5). This indicates that C_2H_2 is probably frozen on dust grains and sublimates along with molecules like CH_4 . Boudin et al. (1998) studied the solid features of C_2H_2 , especially when mixed with H_2O or CO . They found that the C_2H_2 features broaden substantially when mixed with H_2O and to a lesser extent when mixed with CO . They compare the laboratory data to *ISO* data for the colder neighbor, IRS 9, which resulted in an upper limit of $8 \times 10^{17} \text{ cm}^{-2}$ for the column density of solid C_2H_2 . This upper limit is consistent with the observed gas-phase column density seen toward IRS 1. So, it is possible that solid C_2H_2 is sublimating from grain mantles as protostars heat the environment. The observed CH_3/CH_4 ratio agrees with the branching ratio for the destruction of CH_4 . Based on these results CH_2 should also be very abundant. The chemical models for hot cores tend to indicate an age of $\sim 10^5$ years (Doty et al. 2002; Nomura & Millar 2004).

4.5 Conclusions

Here we present a summary of our conclusions:

1. NGC 7538 IRS 1 has a rich spectrum in the mid-infrared. At high spectral resolution, lines of previously observed molecules such as C_2H_2 and HCN are seen as well as weak lines of molecules such as HNC, CH_3 , NH_3 , CH_4 , and CS. We have presented the first infrared detection of interstellar HNC. This is also the first detection of CH_3 toward dense gas.

2. The data show shallow yet saturated lines indicating that either the absorbing gas does not fully cover the continuum source or there is emission filling in the absorption. The observed ortho:para ratio for C_2H_2 is ~ 1.5 instead of the expected value of 3.

3. The rotational temperatures for the various molecules range between 200 and 400 K with the exception of CH_3 , which has one hot component ($T \sim 900$ K). From the derived temperatures, we find that the gas is within ~ 400 AU of the central star (van der Tak et al. 2000).

4. We suggest that the material traces a close to edge-on circumstellar disk as determined from other observations (e.g., De Buizer & Minier 2005). However, it can also be tracing hot, clumpy material close in to the star (see Figure 4.7).

5. Because it is possible to use hot core chemistry to describe chemistry in a disk, the different chemical models do not help identify the physical location of the absorbing gas. However, the models do seem to indicate that

NGC 7538 IRS 1 is an evolved protostar with an age $\sim 10^5$ years.

6. Our observations help constrain the chemistry in massive protostars. The abundances for all the molecules are enhanced, except for possibly CS (see discussion in Chapter 4.3.7). Species known to be present in icy mantles such as CH_4 and NH_3 have high column densities suggesting that they have recently sublimated from grain mantles. The high abundance of the daughter molecules such CH_3 gives constraints on the gas-phase chemistry happening after sublimation of ices. HNC also provides some constraints about the presence of OCN^- on dust grains. It is unclear whether C_2H_2 is a parent molecule or a product of warm gas-phase chemistry. For molecules like HCN, UV/X-ray radiation is important in producing the observed abundances.

With the spectral resolution of TEXES, we can begin to study chemistry of circumstellar disks. In this case, the disk is around a massive protostar. Studies of lower mass stars will require higher sensitivity, which can be achieved with TEXES on the Gemini North Telescope. Infrared absorption studies will be extended to other protostars in order to determine the chemistry at different stages of stellar evolution.

Chapter 5

Summary

This thesis has presented research studying the composition of ices in cold molecular clouds and the chemistry toward two massive protostars, AFGL 2591 and NGC 7538 IRS 1. With the results presented within, we begin to lay the ground work for studies of solar-type protostars.

Ices such as H₂O, CO, and CO₂ had been known to be present toward quiescent cloud regions (e.g., Whittet et al. 1985, 1988, 1998; Eiroa & Hodapp 1989; Smith et al. 1993; Chiar et al. 1994, 1995; Nummelin et al. 2001). Evidence for thermal processing toward some protostars but not others was seen through the line shape of the CO₂ feature (e.g., Boogert et al. 2004b). Recent observations with *Spitzer* IRS presented in Chapter 2 (Knez et al. 2005) show no evidence for thermal processing of the CO₂ ice toward quiescent lines of sight (see also Bergin et al. 2005). Since heating from the protostar appears to change the shape of the solid CO₂ feature at 15 μ m, it may be possible to use it as an age determinant for chemical evolution of protostars.

From the ice studies presented in this thesis, we find that the shape and depth of the 6.0 μ m H₂O feature changes with mixtures. In other words, if H₂O and CO₂ are mixed in close to a one to one ratio, then the H₂O feature

will be deeper and narrower than the feature seen in pure H₂O (see Figure 2.4). Thus, it is important to learn how it changes with ice composition. Laboratory experiments are already underway to explore such effects (Öberg et al. submitted).

Chapter 2 also shows that complex ices such as formic acid (HCOOH) begin to appear on grain mantles even before star formation begins. Additional evidence arises from the 6.8 μm features seen toward two of the three lines of sight studied here (see also Knez et al. 2005), which has been attributed to the ammonium ion, NH₄⁺ (Keane et al. 2001; Schutte & Khanna 2003). Preliminary studies of ice composition toward other background stars also show that other molecules such as methanol (CH₃OH) are also present in “pristine” molecular clouds (Knez et al. in prep.). While statistics cannot be made from 3 lines of sight, the results from Chapter 2 show that some ice features may depend on the visual extinction, A_V (the amount of material in that line of sight), whereas others seem to be affected by other cloud properties such as density or stellar activity. We are beginning to understand the initial chemical conditions of molecular clouds before star formation. Future work by the Cores to Disks Legacy team will aim to determine which cloud properties affect ice composition and, thus, further constrain the initial conditions.

Massive protostars provide bright laboratories in which to study the effects of sublimation of icy grain mantles (see Chapters 3 and 4). Close in to the star (within 100-400 AU) temperatures reach 200–300 K (van der Tak et al. 1999) and complex molecules found on grain mantles are released to

the gas-phase. Observations of AFGL 2591 probe the inner, warm regions of the material surrounding the protostar. With high spectral resolution ($R \sim 75000$) observations using TEXES, two separate components are spectrally resolved. The absorption is potentially associated with clumpy material being pushed out by the outflow. Abundance enhancement of organic molecules such as acetylene, C_2H_2 , and hydrogen cyanide, HCN, show that temperatures as high as 1000 K are not necessary for abundant organic molecules as had been previously thought (Mitchell et al. 1989; Boonman et al. 2001).

High-resolution, infrared spectra of NGC 7538 IRS 1 show that the source is very chemically rich with detections of more molecules than AFGL 2591. Absorption of the following molecules is observed between 11–13 μm : C_2H_2 , HCN, HNC, NH_3 , and CH_3 . At 8 μm , absorption from CH_4 , C_2H_2 , and CS is also observed. Our detection of CH_3 is the first detection of this molecule toward dense gas. Previously, it had only been seen in diffuse gas toward Sgr A* (Feuchtgruber et al. 2000). The column density observed toward NGC 7538 IRS 1 is two orders of magnitude larger than that observed toward the Galactic center. Because CH_3 is likely to form from the destruction of CH_4 , it is important to determine whether the ratio of the two molecules matches those predicted by chemical models. Comparison to models of disk chemistry (Nguyen et al. 2002) show that the observed $CH_3:CH_4$ ratio matches the value predicted, despite the underprediction of the absolute abundances of the two molecules.

The chemical enrichment due to ice sublimation is apparent from the

high abundances of the saturated molecules. Molecules such as CH_4 and NH_3 are known to be present on grain mantles toward protostars (e.g., Gibb et al. 2004). Toward NGC 7538 IRS 1, the abundances of these molecules are enhanced by several orders of magnitude, in agreement with the idea that these species sublime once protostars heat up their environments. We present the first infrared detection of HNCO in the interstellar medium. The high abundance of HNCO may also indicate that it is enhanced by the sublimation of ices. While solid HNCO has not been detected, solid OCN^- has been identified toward many sources (e.g., Lacy et al. 1984; van Broekhuizen et al. 2004; Gibb et al. 2004). Once OCN^- sublimates, a fraction of ice goes into forming HNCO, which leads to the enhanced abundance with relation to the observed HNCO in the envelope material (Zinchenko et al. 2000). Solid C_2H_2 is difficult to detect because of the broadening of the solid state features when C_2H_2 is mixed with H_2O or with CO (Boudin et al. 1998). Boudin et al. derived an upper-limit of $8 \times 10^{17} \text{ cm}^{-2}$ toward NGC 7538 IRS 9, which is consistent with the observed column in the gas-phase seen toward IRS 1. So, despite the lack of evidence of solid C_2H_2 , it is possible that C_2H_2 is also sublimating from dust grains.

Based on the geometrical descriptions of the region (see Minier et al. 2000; De Buizer & Minier 2005), we conclude that the absorbing material around NGC 7538 IRS 1 is potentially tracing material in a photo-evaporating disk. While planets are unlikely to form in disks around massive protostars, this finding lays the ground work for the type of chemistry expected around

solar-type protostars. The high sensitivity of the *Spitzer* IRS has made possible observations of ice (Pontoppidan et al. 2005) and gas (Lahuis et al. 2006) in disks around low mass protostars at low spectral resolution. The high-resolution spectrograph TEXES is currently a visiting instrument at Gemini North. The larger aperture of the telescope increases the sensitivity and allows for the observations of lower-mass protostars known to have circumstellar disks.

While AFGL 2591 and NGC 7538 IRS 1 both show absorption of C_2H_2 and HCN, AFGL 2591 lacks the chemical richness seen toward IRS 1. These differences could be due to different initial conditions for the ices. From the studies of background stars, we find that there can be a lot of variation in the ice composition which is not necessarily correlated to the amount of material present (see Chapter 2 and Knez et al. in prep). Perhaps the region around AFGL 2591 was not rich in complex ices. AFGL 2591 is in relative isolation and, therefore, the parent cloud may not have been enriched by nearby star formation.

Another possible explanation is that they are at different stages of evolution. van der Tak & Menten (2005) found very compact radio emission toward AFGL 2591 which could be due to a hypercompact HII region with a Strömgren radius of 7.3 AU. In contrast NGC 7538 IRS 1 has a compact HII region with a Strömgren radius of 1000 AU (Akabane & Kuno 2005). Also, IRS 1 has ionized material which has been detected in our observations. The [NeII] line at $12.88 \mu\text{m}$ is detected toward NGC 7538 IRS 1 but not

toward AFGL 2591. This seems to indicate that AFGL 2591 is a less evolved source while the C₂H₂ and HCN observations indicate that the two sources have a similar age of $\sim 10^5$ yrs. It is possible that the difference in physical evolution is due to a difference in the radiation field originating from the central star. AFGL 2591 has a luminosity close to an order of magnitude lower than NGC 7538 IRS 1.

Since some molecules are enhanced from ice sublimation and others are formed in the warm gas-phase chemistry, it is possible that both the difference in radiation field as well as the difference in initial ice content play a role in the variation seen toward the two protostars. By studying more lines of sight toward quiescent molecular clouds, we can determine the extent of variations in ice content among the lines of sight. We can then apply that knowledge to differences observed between protostars both high mass and low mass.

Appendix

Appendix 1

Spectroscopy of CH₃ and HNCO

CH₃ is a nearly planar molecule and thus do not expect to see inversion transitions as observed in NH₃. We observe the out-of-plane vibrational mode (similar to the umbrella mode in NH₃). We observe splitting due to spin-rotation interactions. For symmetric-top molecules, the splitting of a rotational level is given by

$$\Delta\nu = (N + 1/2)\{\epsilon_{bb}^{(\nu)} - (\epsilon_{bb}^{(\nu)} - \epsilon_{cc}^{(\nu)})K^2/[N(N + 1)]\}, \quad (1.1)$$

where $\epsilon_{bb}^{(\nu)}$ and $\epsilon_{cc}^{(\nu)}$ are the spin-rotation coupling constants for the B and C axes, respectively, at a given vibrational state, ν . We use Equation (1.1) in deriving the splitting for the lines we observed. The values for $\epsilon_{bb}^{(\nu)}$ and $\epsilon_{cc}^{(\nu)}$ were taken from Yamada et al. (1981).

HNCO is a quasilinear, nearly symmetric-top molecule. The moment of inertia about the figure axis is small and the moments of inertia about the other two axes are much larger (~ 100 times larger) and about equal to each other. Because it is a slightly asymmetric molecule, the levels with $K \neq 0$ are split into two components. Steiner et al. (1979) refer to these levels as upper (U) and lower (L). The following selection rules apply for HNCO:

$$\begin{array}{ll}
\Delta K = 0, & \Delta K = \pm 1 \\
\Delta J = 0 \quad \Delta J = \pm 1, & \Delta J = 0 \quad \Delta J = \pm 1 \\
U \leftrightarrow L \quad U \leftrightarrow U, & U \leftrightarrow U \quad U \leftrightarrow L \\
L \leftrightarrow L, & L \leftrightarrow L
\end{array} \tag{1.2}$$

In Figure 4.4, the HNCO lines labeled R(J)1U correspond to lines where $\Delta K = 0$ and $\Delta J = 1$ and $K = 1$ upper. Likewise, the lines labeled R(J)1L are lines where $\Delta K = 0$ and $\Delta J = 1$ and $K = 1$ lower. Because the splitting between the two levels is small the lines overlap in the spectral region shown in Figures 4.3 and 4.4. Some lines from the upper and lower K states are blended together and give the appearance of double peaked lines.

Bibliography

- Akabane, K., & Kuno, N. 2005, *A&A*, 431, 183
- Allamandola, L. J., Sandford, S. A., Tielens, A. G. G. M., & Herbst, T. M. 1992, *ApJ*, 399, 134
- Bergin, E. A., Melnick, G. J., Gerakines, P. A., Neufeld, D. A., & Whittet, D. C. B. 2005, *ApJ*, 627, L33
- Bevington, P. R., & Robinson, D. K. 2003, *Data reduction and error analysis for the physical sciences* (3rd ed.; Boston: McGraw-Hill)
- Boogert, A. C. A., Blake, G. A., & Öberg, K. 2004a, *ApJ*, 615, 344
- Boogert, A. C. A., Pontoppidan, K. M., Lahuis, F., Jørgensen, J. K., Augereau, J.-C., Blake, G. A., Brooke, T. Y., Brown, J., Dullemond, C. P., Evans, II, N. J., Geers, V., Hogerheijde, M. R., Kessler-Silacci, J., Knez, C., Morris, P., Noriega-Crespo, A., Schöier, F. L., van Dishoeck, E. F., Allen, L. E., Harvey, P. M., Koerner, D. W., Mundy, L. G., Myers, P. C., Padgett, D. L., Sargent, A. I., & Stapelfeldt, K. R. 2004b, *ApJS*, 154, 359
- Boonman, A. M. S., Stark, R., van der Tak, F. F. S., van Dishoeck, E. F., van der Wal, P. B., Schäfer, F., de Lange, G., & Laauwen, W. M. 2001, *ApJ*, 553, L63
- Boonman, A. M. S., & van Dishoeck, E. F. 2003, *A&A*, 403, 1003
- Boonman, A. M. S., van Dishoeck, E. F., Lahuis, F., & Doty, S. D. 2003, *A&A*, 399, 1063
- Botschwina, P., & Sebald, P. 1985, *Journal of Molecular Spectroscopy*, 110, 1
- Botta, O., & Bada, J. L. 2002, *Surveys in Geophysics*, 23, 411
- Boudin, N., Schutte, W. A., & Greenberg, J. M. 1998, *A&A*, 331, 749

- Campbell, B. 1984a, ApJ, 287, 334
- . 1984b, ApJ, 282, L27
- Campbell, B., & Thompson, R. I. 1984, ApJ, 279, 650
- Carr, J. S., Evans, N. J., Lacy, J. H., & Zhou, S. 1995, ApJ, 450, 667
- Charnley, S. B., Tielens, A. G. G. M., & Millar, T. J. 1992, ApJ, 399, L71
- Chiar, J. E., Adamson, A. J., Kerr, T. H., & Whittet, D. C. B. 1994, ApJ, 426, 240
- . 1995, ApJ, 455, 234
- Churchwell, E., & Koornneef, J. 1986, ApJ, 300, 729
- Crovisier, J. 2004, The Molecular Complexity of Comets (ASSL Vol. 305: Astrobiology: Future Perspectives), 179
- De Buizer, J. M., & Minier, V. 2005, ApJ, 628, L151
- Dickel, H. R., Rots, A. H., Goss, W. M., & Forster, J. R. 1982, MNRAS, 198, 265
- Doty, S. D., van Dishoeck, E. F., van der Tak, F. F. S., & Boonman, A. M. S. 2002, A&A, 389, 446
- Draine, B. T. 2003, ARA&A, 41, 241
- Ehrenfreund, P., Boogert, A. C. A., Gerakines, P. A., Tielens, A. G. G. M., & van Dishoeck, E. F. 1997, A&A, 328, 649
- Ehrenfreund, P., & Charnley, S. B. 2000, ARA&A, 38, 427
- Eiroa, C., & Hodapp, K.-W. 1989, A&A, 210, 345
- Elmegreen, B. G., & Lada, C. J. 1977, ApJ, 214, 725
- Evans, N. J., Lacy, J. H., & Carr, J. S. 1991, ApJ, 383, 674

- Evans, II, N. J., Allen, L. E., Blake, G. A., Boogert, A. C. A., Bourke, T., Harvey, P. M., Kessler, J. E., Koerner, D. W., Lee, C. W., Mundy, L. G., Myers, P. C., Padgett, D. L., Pontoppidan, K., Sargent, A. I., Stapelfeldt, K. R., van Dishoeck, E. F., Young, C. H., & Young, K. E. 2003, *PASP*, 115, 965
- Feuchtgruber, H., Helmich, F. P., van Dishoeck, E. F., & Wright, C. M. 2000, *ApJ*, 535, L111
- Forrest, W. J., & Shure, M. A. 1986, *ApJ*, 311, L81
- Gaume, R. A., Goss, W. M., Dickel, H. R., Wilson, T. L., & Johnston, K. J. 1995, *ApJ*, 438, 776
- Gerakines, P. A., Schutte, W. A., & Ehrenfreund, P. 1996, *A&A*, 312, 289
- Gerakines, P. A., Whittet, D. C. B., Ehrenfreund, P., Boogert, A. C. A., Tielens, A. G. G. M., Schutte, W. A., Chiar, J. E., van Dishoeck, E. F., Prusti, T., Helmich, F. P., & de Graauw, T. 1999, *ApJ*, 522, 357
- Gibb, E. L., Whittet, D. C. B., Boogert, A. C. A., & Tielens, A. G. G. M. 2004, *ApJS*, 151, 35
- Goldsmith, P. F. 2001, *ApJ*, 557, 736
- Helmich, F. P., van Dishoeck, E. F., Black, J. H., de Graauw, T., Beintema, D. A., Heras, A. M., Lahuis, F., Morris, P. W., & Valentijn, E. A. 1996, *A&A*, 315, L173
- Henkel, C., Wilson, T. L., & Johnston, K. J. 1984, *ApJ*, 282, L93
- Hoffman, I. M., Goss, W. M., Palmer, P., & Richards, A. M. S. 2003, *ApJ*, 598, 1061
- Houck, J. R., Roellig, T. L., van Cleve, J., Forrest, W. J., Herter, T., Lawrence, C. R., Matthews, K., Reitsema, H. J., Soifer, B. T., Watson, D. M., Weedman, D., Huisjen, M., Troeltzsch, J., Barry, D. J., Bernard-Salas, J., Blacken, C. E., Brandl, B. R., Charmandaris, V., Devost, D., Gull, G. E., Hall, P., Henderson, C. P., Higdon, S. J. U., Pirger, B. E., Schoenwald, J.,

- Sloan, G. C., Uchida, K. I., Appleton, P. N., Armus, L., Burgdorf, M. J., Fajardo-Acosta, S. B., Grillmair, C. J., Ingalls, J. G., Morris, P. W., & Teplitz, H. I. 2004, *ApJS*, 154, 18
- Hudgins, D. M., Sandford, S. A., Allamandola, L. J., & Tielens, A. G. G. M. 1993, *ApJS*, 86, 713
- Indebetouw, R., Mathis, J. S., Babler, B. L., Meade, M. R., Watson, C., Whitney, B. A., Wolff, M. J., Wolfire, M. G., Cohen, M., Bania, T. M., Benjamin, R. A., Clemens, D. P., Dickey, J. M., Jackson, J. M., Kobulnicky, H. A., Marston, A. P., Mercer, E. P., Stauffer, J. R., Stolovy, S. R., & Churchwell, E. 2005, *ApJ*, 619, 931
- Irvine, W. M. 1998, *Origins of Life and Evolution of the Biosphere*, 28, 365
- Kaas, A. A., Olofsson, G., Bontemps, S., André, P., Nordh, L., Hultgren, M., Prusti, T., Persi, P., Delgado, A. J., Motte, F., Abergel, A., Boulanger, F., Burgdorf, M., Casali, M. M., Cesarsky, C. J., Davies, J., Falgarone, E., Montmerle, T., Perault, M., Puget, J. L., & Sibille, F. 2004, *A&A*, 421, 623
- Kameya, O., Morita, K.-I., Kawabe, R., & Ishiguro, M. 1990, *ApJ*, 355, 562
- Keane, J. V., Tielens, A. G. G. M., Boogert, A. C. A., Schutte, W. A., & Whittet, D. C. B. 2001, *A&A*, 376, 254
- Kessler, M. F., Steinz, J. A., Anderegg, M. E., Clavel, J., Drechsel, G., Estaria, P., Faelker, J., Riedinger, J. R., Robson, A., Taylor, B. G., & Ximenez de Ferran, S. 1996, *A&A*, 315, L27
- Knez, C., Boogert, A. C. A., Pontoppidan, K. M., Kessler-Silacci, J., van Dishoeck, E. F., Evans, II, N. J., Augereau, J.-C., Blake, G. A., & Lahuis, F. 2005, *ApJ*, 635, L145
- Kraus, S., Balega, Y., Elitzur, M., Hofmann, K.-H., Meyer, M., Preibisch, T., Rosen, A., Schertl, D., Weigelt, G., & Young, E. T. 2006, *A&A*, 1000, 446
- Kurtz, S., Cesaroni, R., Churchwell, E., Hofner, P., & Walmsley, C. M. 2000, *Protostars and Planets IV*, 299

- Lacy, J. H., Achtermann, J. M., Bruce, D. E., Lester, D. F., Arens, J. F., Peck, M. C., & Gaalema, S. D. 1989a, *PASP*, 101, 1166
- Lacy, J. H., Baas, F., Allamandola, L. J., van de Bult, C. E. P., Persson, S. E., McGregor, P. J., Lonsdale, C. J., & Geballe, T. R. 1984, *ApJ*, 276, 533
- Lacy, J. H., Carr, J. S., Evans, N. J., Baas, F., Achtermann, J. M., & Arens, J. F. 1991, *ApJ*, 376, 556
- Lacy, J. H., Evans, N. J., Achtermann, J. M., Bruce, D. E., Arens, J. F., & Carr, J. S. 1989b, *ApJ*, 342, L43
- Lacy, J. H., Richter, M. J., Greathouse, T. K., Jaffe, D. T., & Zhu, Q. 2002, *PASP*, 114, 153
- Lada, C. J. 1987, in *IAU Symp. 115: Star Forming Regions*, ed. M. Peimbert & J. Jugaku, 1–17
- Lada, C. J., Thronson, H. A., Smith, H. A., Schwartz, P. R., & Glaccum, W. 1984, *ApJ*, 286, 302
- Lahuis, F., & Boogert, A. 2003, in *SFChem 2002: Chemistry as a Diagnostic of Star Formation*, proceedings of a conference held August 21-23, 2002 at University of Waterloo, Waterloo, Ontario, Canada N2L 3G1. Edited by Charles L. Curry and Michel Fich. NRC Press, Ottawa, Canada, 2003, p. 335., ed. C. L. Curry & M. Fich, 335
- Lahuis, F., & van Dishoeck, E. F. 2000, *A&A*, 355, 699
- Lahuis, F., van Dishoeck, E. F., Boogert, A. C. A., Pontoppidan, K. M., Blake, G. A., Dullemond, C. P., Evans, N. J., Hogerheijde, M. R., Jørgensen, J. K., Kessler-Silacci, J. E., & Knez, C. 2006, *ApJ*, 636, L145
- Lee, J.-E., Bergin, E. A., & Evans, II, N. J. 2004, *ApJ*, 617, 360
- Lugo, J., Lizano, S., & Garay, G. 2004, *ApJ*, 614, 807
- Madden, S. C., Irvine, W. M., Matthews, H. E., Brown, R. D., & Godfrey, P. D. 1986, *ApJ*, 300, L79

- Marengo, M., Jayawardhana, R., Fazio, G. G., Hoffmann, W. F., Hora, J. L., Dayal, A., & Deutsch, L. K. 2000, *ApJ*, 541, L63
- Martin, A. H. M. 1973, *MNRAS*, 163, 141
- Menten, K. M., Walmsley, C. M., Henkel, C., Wilson, T. L., Snyder, L. E., Hollis, J. M., & Lovas, F. J. 1986, *A&A*, 169, 271
- Merrill, K. M., & Soifer, B. T. 1974, *ApJ*, 189, L27
- Minier, V., Booth, R. S., & Conway, J. E. 1998, *A&A*, 336, L5
- . 2000, *A&A*, 362, 1093
- Minier, V., Conway, J. E., & Booth, R. S. 2001, *A&A*, 369, 278
- Mitchell, G. F., Curry, C., Maillard, J.-P., & Allen, M. 1989, *ApJ*, 341, 1020
- Mitchell, G. F., Maillard, J.-P., Allen, M., Beer, R., & Belcourt, K. 1990, *ApJ*, 363, 554
- Mozurkewich, D., Schwartz, P. R., & Smith, H. A. 1986, *ApJ*, 311, 371
- Mueller, K. E., Shirley, Y. L., Evans, N. J., & Jacobson, H. R. 2002, *ApJS*, 143, 469
- Murakawa, K., Tamura, M., & Nagata, T. 2000, *ApJS*, 128, 603
- Nguyen, T. K., Viti, S., & Williams, D. A. 2002, *A&A*, 387, 1083
- Nomura, H., & Millar, T. J. 2004, *A&A*, 414, 409
- Nummelin, A., Whittet, D. C. B., Gibb, E. L., Gerakines, P. A., & Chiar, J. E. 2001, *ApJ*, 558, 185
- Pendleton, Y. J., Tielens, A. G. G. M., Tokunaga, A. T., & Bernstein, M. P. 1999, *ApJ*, 513, 294
- Pestalozzi, M. R., Elitzur, M., Conway, J. E., & Booth, R. S. 2004, *ApJ*, 603, L113

- Plume, R., Jaffe, D. T., Evans, N. J., Martin-Pintado, J., & Gomez-Gonzalez, J. 1997, *ApJ*, 476, 730
- Pontoppidan, K. M., Dullemond, C. P., van Dishoeck, E. F., Blake, G. A., Boogert, A. C. A., Evans, II, N. J., Kessler-Silacci, J. E., & Lahuis, F. 2005, *ApJ*, 622, 463
- Pontoppidan, K. M., Fraser, H. J., Dartois, E., Thi, W.-F., van Dishoeck, E. F., Boogert, A. C. A., d'Hendecourt, L., Tielens, A. G. G. M., & Bisschop, S. E. 2003, *A&A*, 408, 981
- Pratap, P., Batrla, W., & Snyder, L. E. 1989, *ApJ*, 341, 832
- Preibisch, T., Balega, Y. Y., Schertl, D., & Weigelt, G. 2003, *A&A*, 412, 735
- Rieke, G. H., & Lebofsky, M. J. 1985, *ApJ*, 288, 618
- Rodgers, S. D., & Charnley, S. B. 2001, *ApJ*, 546, 324
- Schutte, W. A., Boogert, A. C. A., Tielens, A. G. G. M., Whittet, D. C. B., Gerakines, P. A., Chiar, J. E., Ehrenfreund, P., Greenberg, J. M., van Dishoeck, E. F., & de Graauw, T. 1999, *A&A*, 343, 966
- Schutte, W. A., & Khanna, R. K. 2003, *A&A*, 398, 1049
- Scoville, N. Z., Sargent, A. I., Sanders, D. B., Claussen, M. J., Masson, C. R., Lo, K. Y., & Phillips, T. G. 1986, *ApJ*, 303, 416
- Shirley, Y. L., Evans, N. J., Young, K. E., Knez, C., & Jaffe, D. T. 2003, *ApJS*, 149, 375
- Sloan, G. C., Kraemer, K. E., Price, S. D., & Shipman, R. F. 2003, *ApJS*, 147, 379
- Smith, R. G., Sellgren, K., & Brooke, T. Y. 1993, *MNRAS*, 263, 749
- Stahler, S. W., Palla, F., & Ho, P. T. P. 2000, *Protostars and Planets IV*, 327
- Stäuber, P., Doty, S. D., van Dishoeck, E. F., & Benz, A. O. 2005, *A&A*, 440, 949

- Stäuber, P., Doty, S. D., van Dishoeck, E. F., Jørgensen, J. K., & Benz, A. O. 2004, *A&A*, 425, 577
- Steiner, D. A., Wishah, K. A., Polo, S. R., & McCubbin, T. K. 1979, *J. of Mol. Spec.*, 76, 341
- Tielens, A. G. G. M., Allamandola, L. J., Bregman, J., Goebel, J., Witteborn, F. C., & Dhendecourt, L. B. 1984, *ApJ*, 287, 697
- Torrelles, J. M., Ho, P. T. P., Rodriguez, L. F., & Canto, J. 1989, *ApJ*, 343, 222
- Torrelles, J. M., Rodriguez, L. F., Canto, J., Marcaide, J., & Gyulbudaghian, A. L. 1983, *Revista Mexicana de Astronomia y Astrofisica*, 8, 147
- Ungerechts, H., Umbanhowar, P., & Thaddeus, P. 2000, *ApJ*, 537, 221
- van Broekhuizen, F. A., Keane, J. V., & Schutte, W. A. 2004, *A&A*, 415, 425
- van Broekhuizen, F. A., Pontoppidan, K. M., Fraser, H. J., & van Dishoeck, E. F. 2005, *A&A*, 441, 249
- van der Tak, F. F. S., & Menten, K. M. 2005, *A&A*, 437, 947
- van der Tak, F. F. S., van Dishoeck, E. F., Evans, N. J., Bakker, E. J., & Blake, G. A. 1999, *ApJ*, 522, 991
- van der Tak, F. F. S., van Dishoeck, E. F., Evans, N. J., & Blake, G. A. 2000, *ApJ*, 537, 283
- van Dishoeck, E. F., & Blake, G. A. 1998, *ARA&A*, 36, 317
- van Dishoeck, E. F., & van der Tak, F. F. S. 2000, in *Astrochemistry: From Molecular Clouds to Planetary*, 97
- Weingartner, J. C., & Draine, B. T. 2001, *ApJ*, 548, 296
- Werner, M. W., Becklin, E. E., Gatley, I., Matthews, K., Neugebauer, G., & Wynn-Williams, C. G. 1979, *MNRAS*, 188, 463

- Werner, M. W., Roellig, T. L., Low, F. J., Rieke, G. H., Rieke, M., Hoffmann, W. F., Young, E., Houck, J. R., Brandl, B., Fazio, G. G., Hora, J. L., Gehrz, R. D., Helou, G., Soifer, B. T., Stauffer, J., Keene, J., Eisenhardt, P., Gallagher, D., Gautier, T. N., Irace, W., Lawrence, C. R., Simmons, L., Van Cleve, J. E., Jura, M., Wright, E. L., & Cruikshank, D. P. 2004, *ApJS*, 154, 1
- Whittet, D. C. B., Bode, M. F., Longmore, A. J., Adamson, A. J., McFadzean, A. D., Aitken, D. K., & Roche, P. F. 1988, *MNRAS*, 233, 321
- Whittet, D. C. B., Gerakines, P. A., Tielens, A. G. G. M., Adamson, A. J., Boogert, A. C. A., Chiar, J. E., de Graauw, T., Ehrenfreund, P., Prusti, T., Schutte, W. A., Vandenbussche, B., & van Dishoek, E. F. 1998, *ApJ*, 498, L159
- Whittet, D. C. B., McFadzean, A. D., & Longmore, A. J. 1985, *MNRAS*, 216, 45P
- Whittet, D. C. B., Pendleton, Y. J., Gibb, E. L., Boogert, A. C. A., Chiar, J. E., & Nummelin, A. 2001, *ApJ*, 550, 793
- Whittet, D. C. B., Schutte, W. A., Tielens, A. G. G. M., Boogert, A. C. A., de Graauw, T., Ehrenfreund, P., Gerakines, P. A., Helmich, F. P., Prusti, T., & van Dishoek, E. F. 1996, *A&A*, 315, L357
- Willner, S. P. 1976, *ApJ*, 206, 728
- Willner, S. P., Gillett, F. C., Herter, T. L., Jones, B., Krassner, J., Merrill, K. M., Pipher, J. L., Puetter, R. C., Rudy, R. J., Russell, R. W., & Soifer, B. T. 1982, *ApJ*, 253, 174
- Wilson, T. L., Walmsley, C. M., Batrla, W., & Mauersberger, R. 1983, *A&A*, 127, L19
- Wynn-Williams, C. G., Becklin, E. E., & Neugebauer, G. 1974, *ApJ*, 187, 473
- Yamada, C., Hirota, E., & Kawaguchi, K. 1981, *J. Chem. Phys.*, 75, 5256
- Zheng, X.-W., Zhang, Q., Ho, P. T. P., & Pratap, P. 2001, *ApJ*, 550, 301
- Zinchenko, I., Henkel, C., & Mao, R. Q. 2000, *A&A*, 361, 1079

Vita

Claudia Knez was born in Guadalajara, Mexico on 17 May 1978, the daughter of Ana Celina Knez and Michael A. Knez. In August 1990, she moved to Urbanna, Virginia. In 1996, she graduated summa cum laude from Middlesex High School. She received the Bachelor of Arts degree in Astrophysics from the University of Virginia in May 2000. In September 2000, she enrolled in the astronomy program at the University of Texas at Austin.

Permanent address: 102 E. 52nd St. Apt. B
Austin, Texas 78751

This dissertation was typeset with \LaTeX^\dagger by the author.

[†] \LaTeX is a document preparation system developed by Leslie Lamport as a special version of Donald Knuth's \TeX Program.